

Use of Multiple Imaging Views for Improving Image Quality  
in Small Animal MR Imaging Studies

Dissertation

Presented in Partial Fulfillment of the Requirements for the Degree  
Doctor of Philosophy in the Graduate School of The Ohio State  
University

By

Niranchana Manivannan, M.S.

Graduate Program in Electrical and Computer Engineering

The Ohio State University

2015

Dissertation Committee:

Bradley D. Clymer, PhD, Co-Advisor

Kimerly A. Powell, PhD, Co-Advisor

Can E. Koksal, PhD

© Copyright by  
Niranchana Manivannan  
2015

## Abstract

*In vivo* imaging provides a venue for studying and understanding the biological mechanism of a living system noninvasively. High resolution scanning for MR imaging is practically limited by the length of the scan for *in vivo* applications. *In vivo* small animal MRI suffers from subject motion which can degrade image quality with blurring and artifacts. In many small animal imaging studies, multiple imaging views are already obtained as part of the normal workflow but the information taken from one view is not generally combined with that from another view. The main objective of this dissertation is to study the use of multiple imaging views for improving image quality in small animal MR imaging studies. The goal of the study is to evaluate post-processing techniques that could make use of multiple low resolution image acquisitions for increasing resolution in through-plane 3D images and to reduce motion artifacts in in-plane 2D images. Both qualitative and quantitative comparisons are carried out to evaluate the performance of the algorithms and they are demonstrated in *in vivo* settings.

To my teachers

## Acknowledgments

I would like to express my sincere gratitude towards my advisors Dr. Bradley Clymer and Dr. Kimerly Powell for giving me a chance to work under their able guidance. This work is a testimony to the staunch support and genuine care shown by Dr. Powell. Thanks for having confidence in me. I am really grateful to Dr. Clymer for his guidance throughout my research project. It is a privilege to have worked with him. Sometimes their words of encouragement were my only motivation. I would like to thank my committee member Dr. Koksal for the help and support he provided throughout this work. I would like to extend my thanks to Department of Biomedical Informatics for funding this project.

I would like to thank Dr. Anna Bratasz for her guidance in my experiments and lab work. She is a magician who can make anything and everything work when it comes to experiments. I would like to thank James Gentry, Patricia Toothman and Stephanie Muldrow for helping me navigate through administrative paperwork. I would like to thank my mentors back in India. I would not have been able to complete this journey without my friends. Thanks to Mathi, Nazreen, Nallasivan, Lakshminarasimhan, Anusha, Balaji, Eppie, Yazhini, Angel, Gayathri, Makam, Shardha, Radha and Jayashri for their support throughout this journey. I am grateful to all my friends in Columbus who made Columbus a home away from home.

Finally, I deeply appreciate the love and trust shown towards me by my mom, dad, brother and rest of my family. No part of this journey would have been possible without Amit Gera, who gave me strength and courage to continue.

## Vita

2004-2008 .....	B.E. Electronics and Communication Engineering, College of Engineering, Guindy
2008-2010 .....	M.S. Electrical and Computer Engineering, The Ohio State University, Columbus
2008-2014 .....	Graduate Research Associate, Small Animal Imaging Center, The Ohio State University, Columbus

## Publications

### Research Publications

N. Manivannan, B. Clymer, A. Bratasz, K. Powell “Comparison of Super Resolution Reconstruction Acquisition Geometries for use in Mouse Phenotyping”. *IJBI*, 2013.

N. Manivannan, B. Clymer, A. Bratasz, K. Powell “Orthogonal Super Resolution Reconstruction for 3D Isotropic Imaging in 9.4 MRI”. *ISMRM*, 2011.

N. Manivannan, B. Clymer, A. Bratasz, K. Powell “Streaking Artifact Reduction in Orthogonal Super Resolution Reconstruction of MRI data sets”. *ISMRM*, 2013.

N. Manivannan, K. Banks, A. Bratasz, D. Wheeler, M. Joseph, R. Huttinger, R. Hershberger, K. Powell “*In vivo* Cardiac MRI Development for Studying Zebrafish Models of Myocardial Disease”. *ISMRM*, 2014.

D. Stredney, B. Hittle, C. M. Chen, T. Kerwin, A. Bratasz, N. Manivannan, K. Powell “Virtual simulation of mouse anatomy and procedural techniques”. *Studies in Health Technology and Informatics*, 173:500-5, 2012.

## **Fields of Study**

Major Field: Electrical and Computer Engineering

# Table of Contents

	<b>Page</b>
Abstract . . . . .	ii
Dedication . . . . .	iii
Acknowledgments . . . . .	iv
Vita . . . . .	vi
List of Tables . . . . .	xii
List of Figures . . . . .	xiv
1. Introduction . . . . .	1
1.1 Background . . . . .	1
1.2 Statement of Problem Studied in this Dissertation . . . . .	8
1.3 Overview of the Dissertation . . . . .	9
2. In Depth Comparison of SR Acquisition Geometries and Trade-offs In- volved . . . . .	12
2.1 Introduction . . . . .	12
2.2 Material and Methods . . . . .	16
2.2.1 Super Resolution Reconstruction Method . . . . .	16
2.2.2 Resolution Phantom . . . . .	17
2.2.2.1 Quantitative measures . . . . .	18
2.2.3 Biological Phantom . . . . .	20
2.2.3.1 Quantitative measures . . . . .	21
2.2.4 <i>In vivo</i> Experiment . . . . .	22
2.3 Results . . . . .	23
2.3.1 Resolution Phantom . . . . .	23

2.3.2	Biological Phantom . . . . .	24
2.3.3	<i>In vivo</i> Experiment . . . . .	27
2.4	Discussion . . . . .	27
3.	Addressing Streaking Artifacts in Orthogonal SRR . . . . .	41
3.1	Introduction . . . . .	41
3.2	Method 1: Adding Additional Oblique Views . . . . .	42
3.2.1	Theory . . . . .	42
3.2.2	Experiments . . . . .	44
3.2.2.1	Simulated Shepp-Logan phantom . . . . .	44
3.2.2.2	Simulated biological phantom . . . . .	45
3.2.2.3	<i>In vivo</i> experiment . . . . .	46
3.2.3	Quantitative Measures . . . . .	46
3.3	Method 2: Gradient Guided Sigmoid Based Interpolation Model . . . . .	47
3.3.1	Theory . . . . .	47
3.3.2	Algorithm . . . . .	50
3.3.3	Experiments . . . . .	52
3.3.3.1	3D wedge phantom . . . . .	53
3.3.3.2	Concentric sphere phantom . . . . .	53
3.3.3.3	Simulated SLP experiment . . . . .	54
3.3.3.4	Simulated biological phantom . . . . .	54
3.3.3.5	<i>In vivo</i> experiment . . . . .	55
3.3.4	Quantitative Measures . . . . .	55
3.4	Results for Method 1: Adding Additional Oblique Views . . . . .	56
3.4.1	Simulated Shepp-Logan Phantom . . . . .	56
3.4.1.1	Qualitative evaluation . . . . .	56
3.4.1.2	Quantitative evaluation . . . . .	57
3.4.2	Simulated Biological Phantom . . . . .	57
3.4.2.1	Qualitative evaluation . . . . .	57
3.4.2.2	Quantitative evaluation . . . . .	58
3.4.3	<i>In vivo</i> Experiment . . . . .	58
3.4.3.1	Qualitative evaluation . . . . .	58
3.4.3.2	Quantitative evaluation . . . . .	59
3.5	Results for Method 2: Gradient Guided Sigmoid Based Interpolation Model . . . . .	59
3.5.1	3D Wedge Phantom . . . . .	59
3.5.1.1	Qualitative evaluation . . . . .	59
3.5.1.2	Quantitative evaluation . . . . .	60
3.5.2	Concentric Sphere . . . . .	60
3.5.2.1	Qualitative evaluation . . . . .	60
3.5.2.2	Quantitative evaluation . . . . .	60

3.5.3	Simulated SLP Experiment . . . . .	61
3.5.3.1	Qualitative evaluation . . . . .	61
3.5.3.2	Quantitative evaluation . . . . .	61
3.5.4	Biological Phantom . . . . .	62
3.5.4.1	Qualitative evaluation . . . . .	62
3.5.4.2	Quantitative evaluation . . . . .	62
3.5.5	<i>In vivo</i> Experiment . . . . .	62
3.5.5.1	Qualitative evaluation . . . . .	62
3.5.5.2	Quantitative evaluation . . . . .	63
3.6	Discussion . . . . .	63
4.	Motion Correction Using Orthogonal Images . . . . .	84
4.1	Introduction . . . . .	84
4.2	Materials and Methods . . . . .	86
4.2.1	Algorithm . . . . .	86
4.2.2	Motion Experiments . . . . .	87
4.2.2.1	Simulated motion in Shepp-Logan phantom . . . . .	88
4.2.2.2	Simulated motion in biological phantom . . . . .	90
4.2.3	Real Motion in <i>In vivo</i> Experiment . . . . .	90
4.2.3.1	<i>In vivo</i> gated experiment . . . . .	90
4.2.3.2	<i>In vivo</i> non-gated experiment . . . . .	91
4.2.4	Quantitative Measures . . . . .	91
4.2.5	Motion Artifact Metric . . . . .	91
4.2.5.1	Contrast metric . . . . .	91
4.2.5.2	Mean square error (MSE) and root mean square deviation (RMS) . . . . .	91
4.2.6	Tests Using Automated Image Segmentation Algorithms . . . . .	92
4.2.6.1	Otsu's segmentation of brain in biological phantom . . . . .	93
4.2.6.2	Active contour body segmentation in <i>in vivo</i> mouse model . . . . .	94
4.2.6.3	Active contour kidney segmentation in <i>in vivo</i> mouse model . . . . .	94
4.2.7	Statistical Metrics Used for Evaluation of Tests Using Automated Image Segmentation Algorithms . . . . .	95
4.2.7.1	Type I and Type II error . . . . .	95
4.2.7.2	Positive and negative predictive values . . . . .	95
4.2.7.3	Rand index and rand error . . . . .	96
4.2.7.4	Fractional volume error . . . . .	97
4.3	Results . . . . .	97
4.3.1	Simulated Motion in Shepp-Logan Phantom . . . . .	97
4.3.1.1	Qualitative evaluation . . . . .	97

4.3.1.2	Quantitative evaluation . . . . .	99
4.3.2	Simulated Motion in Biological Phantom . . . . .	100
4.3.2.1	Qualitative evaluation . . . . .	100
4.3.2.2	Quantitative evaluation . . . . .	101
4.3.2.3	Otsu's segmentation of brain in biological phantom . . . . .	102
4.3.3	Gated <i>In vivo</i> Experiment . . . . .	103
4.3.3.1	Qualitative evaluation . . . . .	103
4.3.3.2	Quantitative evaluation . . . . .	104
4.3.3.3	Active contour body segmentation in <i>in vivo</i> mouse model . . . . .	105
4.3.3.4	Active contour kidney segmentation in <i>in vivo</i> mouse model . . . . .	105
4.3.4	Non-gated <i>In vivo</i> Experiment . . . . .	106
4.3.4.1	Qualitative evaluation . . . . .	106
4.3.4.2	Quantitative evaluation . . . . .	106
4.4	Discussion . . . . .	106
5.	Conclusions and Future Work . . . . .	124
5.1	Thesis Summary and Conclusions . . . . .	124
5.2	Suggested Future Work . . . . .	126
	Bibliography . . . . .	128

## List of Tables

Table	Page
1.1 List of abbreviations used in the thesis . . . . .	11
2.1 Quantitative measures of image quality calculated from line phantom	25
2.2 Quantitative measures of image quality calculated from images of biological phantom . . . . .	39
3.1 Quantitative parameters for the SLP with added oblique views at 45° increment . . . . .	67
3.2 Quantitative parameters for the SLP with added oblique views at 30° increment . . . . .	79
3.3 Quantitative parameters for biological phantom when oblique LR views are added . . . . .	80
3.4 Quantitative parameters for <i>in vivo</i> experiment when oblique LR views are added . . . . .	81
3.5 Mean edge width of wedge phantom for gradient guided sigmoid based interpolation . . . . .	81
3.6 Mean edge width of concentric sphere phantom for gradient guided sigmoid interpolation . . . . .	82
3.7 Quantitative parameters for gradient guided sigmoid interpolation in SLP . . . . .	82
3.8 Quantitative parameters for gradient guided sigmoid interpolation in biological phantom . . . . .	82

3.9	Quantitative parameters for gradient guided sigmoid interpolation in <i>in vivo</i> experiment . . . . .	83
4.1	Quantitative parameters for SLP random motion simulation . . . . .	101
4.2	Quantitative parameters for SLP periodic motion simulation . . . . .	102
4.3	Quantitative parameters for SLP bulk motion simulation . . . . .	103
4.4	Quantitative parameters for SLP simulation with Gaussian noise . . . . .	104
4.5	Quantitative parameters for SLP simulation experiment with different ARs . . . . .	105
4.6	Quantitative parameters for <i>ex vivo</i> (biological) phantom simulation experiment . . . . .	106
4.7	Statistical metrics when multi-level Otsu is used for segmentation of brain in biological phantom images with simulated motion . . . . .	107
4.8	Quantitative parameters for <i>in vivo</i> gated study . . . . .	108
4.9	Statistical metrics when active contour body segmentation is used in <i>in vivo</i> mouse model . . . . .	108
4.10	Statistical metrics when active contour kidney segmentation is used in <i>in vivo</i> mouse model . . . . .	109
4.11	Quantitative parameters for <i>in vivo</i> non-gated rib tumor study . . . . .	109

## List of Figures

Figure	Page
2.1 Block diagram of Irani and Peleg's IBP algorithm . . . . .	31
2.2 Schematic illustrating the orientation of the resolution phantom where the long axis of tubes were positioned orthogonal to the slice-select direction of the a) shifted, b) rotational, c) orthogonal acquisition geometries, and d) orientation of tubes in the resolution phantom for the oblique setup and the acquisition geometries shown in Figure 2.2a, 2.2b, 2.2c were repeated for this oblique orientation. (Axes in this image represent physical coordinates and the main magnetic field is in Z direction) . . . . .	32
2.3 Axial view of the line pair resolution phantom illustrating sample edge profiles chosen to calculate the edge width . . . . .	33
2.4 Schematic illustrating the orientation of the <i>ex vivo</i> embryo with respect to the slice-select direction of the acquisition geometries . . . . .	34
2.5 2D slice image of the <i>ex vivo</i> embryo illustrating the location of 9*9*9 voxel ROI chosen for SNR and CNR calculations and sample edge profiles chosen to calculate the edge width . . . . .	35
2.6 2D slice images (Image plane represented is orthogonal to the long axis of the tube which is placed along Y-axis in Figure 2.2a) of resolution phantom where the long axis of the tubes is orthogonal to the acquisition plane and LR image stacks were collected with a voxel AR of 1:1:5: a) interpolated, b) shifted, c) rotational, d) orthogonal, e) in-plane, f) line plot, and where the long axis of the tubes is oblique to the acquisition plane: g) interpolated, h) shifted, i) rotational, j) orthogonal, k) in-plane, l) line plot . . . . .	36

2.7	2D slice images (Image plane represented is orthogonal to the long axis of the tube which is placed along Y-axis in Figure 2.2a) of resolution phantom where the long axis of the tubes is orthogonal to the acquisition plane and LR image stacks were collected with a voxel AR of 1:1:10: a) interpolated, b) shifted, c) rotational, d) orthogonal, e) in-plane, f) line plot, and where the long axis of the tubes is oblique to the acquisition plane: g) interpolated, h) shifted, i) rotational, j) orthogonal, k) in-plane, l) line plot . . . . .	37
2.8	2D sagittal view of SRR images of the <i>ex vivo</i> embryo based on different acquisition geometries: a) interpolated, b) shifted, c) rotational, d) orthogonal, e) isotropic. White arrow indicates structures in the nasal cavity not clearly observed in the corresponding SRR images . . . . .	38
2.9	2D sagittal view of the <i>ex vivo</i> embryo for a) 3D isotropic acquisition, and SRR images based on LR image stacks with AR equal to b) 1:1:4, c) 1:1:6, d) 1:1:8, and e) 1:1:10. White arrow highlights rib structures that are present in the SRR image but not present in the isotropic 3D image . . . . .	38
2.10	Cutaway section from 3D volume rendering of the <i>in vivo</i> mouse abdomen based on orthogonal SRR (left) with AR equal to 1:1:10 and single interpolated view (right). The solid arrow points to the wall of the stomach, dashed arrow to the kidney, and dotted arrow to the liver vasculature. Biological structures can be observed clearly in any oblique cutting plane of the SRR image as opposed to single 2D multi-slice image with linear interpolation . . . . .	40
3.1	Image of SLP showing line profiles along which edge width is measured and CNR, SNR measurement windows . . . . .	47
3.2	Gradient from the HR sagittal view (red mask) overlaid on the error resulting from the orthogonal SRR algorithm. Brighter the intensity, higher the error, it is evident that the homogeneous regions have lesser error when compared to the areas with higher gradients (structural boundaries or edges) . . . . .	49

3.3	a) Isotropic 3D image of liver, b) HR volume reconstructed from LR image stacks with AR 1:1:8 by orthogonal SRR, c) average image used as initial guess for orthogonal SRR, d) average of two images orthogonal to image with partial volume mixing, e) gradients from average upsampled image . . . . .	50
3.4	Flowchart for gradient based sigmoid interpolation in orthogonal SRR	68
3.5	1D line profile is highlighted in HR image (left), the plot of pixel intensities for HR image, linear interpolated image and gradient guided interpolation image along the line profile (right) . . . . .	69
3.6	Three dimensional wedge phantom . . . . .	69
3.7	SRR orthogonal images with oblique views added at 45° increments; AR of LR image stack is 1:1:8 a) 3D, b) interpolated, c) 3-view ortho SRR, d) 4-view ortho SRR, e) 5-view ortho SRR. Arrow highlights the three ellipsoids which are resolved in ortho SRR but not in linear interpolated image stack . . . . .	70
3.8	SRR orthogonal images with oblique views added at 30° increments; AR of LR image stack is 1:1:8 a) 3D, b) interpolated, c) 3-view ortho SRR, d) 4-view ortho SRR, e) 5-view ortho SRR, f) 6-view ortho SRR, g) 7-view ortho SRR . . . . .	71
3.9	a) Isotropic 3D image and the area enlarged for the comparison is highlighted, b) HR volume simulated from LR image stacks with AR 1:1:10 by 3-view orthogonal SRR (enlarged ROI to show the area of interest), c) HR volume simulated from LR image stacks with AR 1:1:10 by 4-view orthogonal SRR, d) ground truth (isotropic 3D image). Lung-liver boundary is highlighted with white arrow and stomach wall is highlighted with yellow arrow. . . . .	72
3.10	a) Interpolated image, b) HR volume reconstructed using 3-view orthogonal SRR, c) HR volume reconstructed using 4-view orthogonal SRR, d) HR volume reconstructed using 5-view orthogonal SRR, e) HR volume acquired in-plane. The spinal cord and the intestinal tract are highlighted by yellow arrow and white arrow respectively. Red arrow highlights the streaking artifact . . . . .	73

3.11	a) HR image from which LR images are simulated, LR images interpolated in through-plane direction using: b) nearest neighbor, c) linear, d) cubic, e) gradient based sigmoid interpolation, f) difference between the linear and gradient based sigmoid interpolation . . . . .	74
3.12	a) HR image from which LR images are simulated, orthogonal SRR images reconstructed direction using: b) linear, c) cubic, d) gradient based sigmoid interpolation, e) line profile for plotting and edge width calculation, f) line plot across the boundary of the sphere and the inflection point in the HR image and sigmoid SRR is denoted by dotted line and asterisk respectively . . . . .	75
3.13	a) HR image from which LR images are simulated and the line profile (highlighted by blue line) to study the effect of SRR in small structures, and the line profiles (highlighted by yellow line) used for edge width calculations, orthogonal SRR images reconstructed using: b) linear, c) cubic, d) gradient based sigmoid interpolation, e) line profile across the boundary of the small ellipsoids, showing the location of the structures in sigmoid SRR is comparable with HR image. Red arrow highlights the three small ellipsoids . . . . .	76
3.14	Enlarged thoracic area of <i>ex vivo</i> embryo showing developing heart, lungs and liver in: a) 3D isotropic image, b) linear SRR, c) cubic SRR, d) sigmoidal SRR (pleural cavity which is filled with contrast and fixative is highlighted with arrow) . . . . .	77
3.15	Flank area of <i>in vivo</i> mouse showing tumor in: a) interpolated, b) linear SRR, c) cubic SRR, d) sigmoidal SRR, e) HR in-plane (white and yellow arrows highlight the fat filled cavity in tumor and tail muscle). AR of LR image stacks used is 1:1:10 . . . . .	78
4.1	Coronal and axial acquisition geometry along with encoding directions	113
4.2	Coronal (left) and axial (right) images of thoracic cavity of <i>in vivo</i> mouse obtained for rib tumor study . . . . .	114
4.3	Flowchart of the motion correction algorithm . . . . .	115

4.4	Shepp-Logan phantom a) coronal image stack corrupted with random motion, b) axial image stack with no motion rotated and viewed in coronal plane, c) motion corrected image, d) average image. The motion artifacts are highlighted by arrows . . . . .	116
4.5	Shepp-Logan phantom a) coronal image stack corrupted with more periodic motion than axial image stack, b) axial image stack corrupted with motion, c) motion corrected image . . . . .	117
4.6	Shepp-Logan phantom with bulk motion a) motion corrupted coronal image stack, b) axial image stack with bulk misalignment rotation of $4^\circ$ , c) motion corrected image when bulk misalignment rotation is $4^\circ$ , d) motion corrupted coronal image stack, e) axial image stack with bulk misalignment rotation of $8^\circ$ , f) motion corrected image when bulk misalignment rotation is $8^\circ$ . . . . .	118
4.7	Shepp-Logan phantom with added gaussian noise a) coronal image stack with gaussian noise $\sigma = 0.001$ , b) axial image stack with gaussian noise $\sigma = 0.001$ , c) motion corrected image in case of gaussian noise with $\sigma = 0.001$ , d) coronal image stack with gaussian noise $\sigma = 0.005$ , e) axial image stack with gaussian noise $\sigma = 0.005$ , f) motion corrected image in case of gaussian noise with $\sigma = 0.005$ . . . . .	119
4.8	Shepp-Logan phantom with different ARs a) motion corrupted coronal stack, b) axial stack with AR 1:1:5, c) motion corrected image when AR is 1:1:5, d) motion corrupted coronal stack, e) axial stack with AR 1:1:10, f) motion corrected image when AR is 1:1:10 . . . . .	120
4.9	Simulated motion in biological phantom experiment a) coronal view corrupted with motion, b) axial view upsampled and rotated with motion, c) motion corrected image, d) <i>ex vivo</i> image without motion . .	121
4.10	<i>In vivo</i> gated experiment for obesity study, a) coronal with motion, b) axial with motion, c) axial upsampled and rotated, d) motion corrected image. The ghosting artifact in coronal view is highlighted by red arrow. Anatomical details recovered by the correction algorithm are highlighted by white arrows . . . . .	122
4.11	<i>In vivo</i> non-gated experiment for rib tumor study a) axial image stack with less pronounced motion, b) coronal image stack with motion, c) motion corrected image . . . . .	123

# Chapter 1: Introduction

## 1.1 Background

Small animal imaging plays an important role in the improvement of preclinical and translational biomedical research. Small animals are increasingly used for biomedical research, because they are inexpensive with short life span and gestation period [2]. Small animals like mice and rats share many human phenotypes and pathologies. Mice and humans share about 97.5% of their working DNA [48]. The ease of modification of the small animal genotype helps in creating transgenic animal models with induced pathological states that are suitable for studying various human diseases [2].

MRI is based on the principle of detecting the absorption and emission of radio waves by protons (hydrogen nuclei) in the presence of strong magnetic field [38]. Some of the advantages of the MRI are it is noninvasive, provides excellent soft tissue contrast and no ionizing radiation exposure is involved [2]. MRI produces images with high spatial and temporal resolution and the repeatability and reproducibility of the experiments are well established. Noninvasive *in vivo* imaging enables the animal subjects to serve as their own control in longitudinal studies if imaging is performed prior to initiation of the disease. One of the major advantages of medical

imaging techniques like MRI is the ability to perform longitudinal noninvasive studies, thereby reducing the number of animals required for a particular study. For example, instead of having to sacrifice animals at each time point in a longitudinal study, a group of animals can be monitored at multiple time points by imaging internal tissues noninvasively during the study.

Some of the challenges faced by small animal MRI are the presence of physiological motion, small size of the animal and limited time available for the scanning due to the use of general anesthesia. Small animal MR imaging is similar to clinical MR imaging in that they both use the same data acquisition setups and pulse imaging sequences. However, the respiratory and cardiac rates of small animals are faster than human subjects and animals cannot be instructed to hold their breath during imaging. Hence, *in vivo* small animal MRI suffers from subject motion which can degrade image quality with blurring and artifacts [73].

The structures of interest in small animal imaging are of the order of millimeter or smaller, thus making it important to acquire high resolution images [2]. Because of the finer feature sizes of organs and tissues, small animal MRI is usually done in ultrahigh field MRI machines in order to obtain higher spatial resolution and signal-to-noise ratio (SNR). High field and ultrahigh field MRI yield high resolution images with more SNR because of the higher energy emitted per photon but the problems posed by gradient inhomogeneities are more pronounced than that in lower field clinical magnets [22]. However, high resolution imaging requires low slice thickness which results in fewer protons contributing to the MRI signal. To achieve a suitable SNR, the number of averaged scans has to be increased, which in turn leads to increase in scanning time. There is a limit to how long the acquisition time can be increased as it

is not desirable to keep the animal under anesthesia for extended period of time [23]. Therefore in MRI images, through-plane resolution<sup>1</sup> is usually lower than the in-plane resolution.

To sum up, even at ultrahigh field strength, high resolution imaging requires longer acquisition time to accommodate weaker signal from smaller voxels<sup>2</sup> because multiple acquisition are required to average out the noise effects [1]. Therefore, key trade-offs for acquiring high resolution images in MRI are acquisition time, resolution and SNR. Long acquisition time could help getting high resolution images with high SNR, however, it is not desirable. When the long acquisition time is taken in to account along with the animal preparation time and recovery time, the total time taken for an imaging session is long.

Many acquisition techniques have been proposed to reduce the scanning time in MRI aimed at acquiring high resolution images in less time. These techniques include parallel imaging [26], partial Fourier imaging [41] and partial echo [30]. Parallel imaging is a technique which combines the signals from several coils within a phased array to reconstruct an image and thus results in lower acquisition time. The major drawback of parallel acquisition technique is the requirement of specialized hardware (phased array coil) and low SNR. Partial Fourier imaging techniques are based on partial filling of  $k$ -space. Low acquisition time comes at the expense of reduced SNR. Truncation artifacts also pose a major problem for partial  $k$ -space filling [42]. These techniques rely on specialized hardware and software for implementation and are not always available.

<sup>1</sup>in-plane resolution is the resolution in X-Y plane and through-plane resolution is the resolution in Z direction of MRI images.

<sup>2</sup>pixel and voxel refers to smallest image forming unit in 2D and 3D MRI images respectively.

Super resolution reconstruction (SRR) is a post processing technique to improve through-plane resolution that does not rely on any specialized equipment or acquisition software [17], although it can be used in conjunction with other techniques like parallel imaging and partial Fourier acquisition which are aimed at reducing acquisition time. Several SRR methods have been proposed differing in acquisition geometry and in the number of the low resolution (LR) image stacks and the optimization algorithms used for iterative reconstruction. Plenge et al. [52] evaluated different optimization techniques used for SRR of MRI data. However, no definitive quantitative comparison has been published to compare the effect of acquisition geometry on SRR.

The shifted and rotated acquisition geometries are the most commonly used SRR acquisition geometry [17], [60]. The orthogonal acquisition geometry is a relatively new SRR geometry, introduced in 2008 [62]. The main advantage of using orthogonal acquisition for SRR is that it requires a lower number of views and thus less acquisition time when compared to shifted or rotated view acquisitions. In most research studies, at least two orthogonal image stacks are acquired for the anatomical studies and using them in SRR geometry without having to collect new additional stacks exclusively for this purpose is advantageous. The results of the comparison study of these three SRR acquisition geometries (discussed in detail in chapter 2) indicate that super resolution reconstructed images based on orthogonally acquired low resolution images resulted in reconstructed images with higher SNR and contrast-to-noise (CNR) in less acquisition time than those based on rotational or shifted acquisition geometries. Although SRR based on the shifted and rotated geometries could more closely approximate the

structures observed in the 3D isotropic acquisition by acquiring a greater number of views, this would defeat the overall goal of reducing acquisition time.

The SRR images based on three orthogonal views can exhibit significant streaking artifacts and mislocalization when the low resolution data sets are acquired with a slice thickness 6 times greater than the in-plane voxel size (discussed in detail in chapter 2). In most *in vivo* studies the aspect ratio (AR)<sup>3</sup> is high, so exploration of a way to reduce the reconstruction artifacts observed in orthogonal SRR would make the technique more useful for *in vivo* studies. A significant source of these reconstruction artifacts in SRR image is the interpolation scheme used to upsample the MRI images. Linear interpolation has been widely used in medical images [39] and as it is more relevant when there is absence of additional information and the interpolation factor is high. An extended review of interpolation methods used can be found in [18], [39]. But most of these interpolation schemes require either prior knowledge [31], [63] or a large training set to incorporate the domain knowledge into the design of the interpolators [8]. A sigmoid based interpolation model modulated by the local gradient profile of orthogonal datasets is studied in this dissertation. The sigmoid interpolation model provides a level of smoothing along the boundaries while maintaining sharp intensity contrast [47]. As typically two orthogonal views are obtained in the studies, it is advantageous to use the gradient information from orthogonal view to improve the interpolation of another image stack and it is a post processing technique which aims at overcoming the above mentioned disadvantages like requirement of prior knowledge or training sets.

<sup>3</sup>Voxel's AR refer to the proportional relationship of its size in each dimension (i.e., width:height:depth) and are directly related to SNR and acquisition time.

The ghosting artifacts caused by various types of motion pose a big challenge in small animal MRI. Although the animal is under anesthesia, motion cannot be eliminated completely [23]. Many techniques have been developed to eliminate or reduce effects of motion. Active restraints have been used to fasten the subject to the bed to reduce motion, but this cannot eliminate motion completely [2]. Furthermore, scans having long acquisition times (as in the case of high resolution imaging) are more susceptible to ghosting artifacts due to motion. Several model based correction algorithms have been implemented for reducing the effect of ghosting artifacts in MRI images [44], [75], [74], [24]. But it is difficult to model all of the various causes of modulation of  $k$ -space data in a correction algorithm. Some of the established correction methods based on specific artifact models may not account for all the causes of  $k$ -space modulation [75], [24]. Additionally, the correction models that are well established in human studies cannot be extended to small animals without significant modifications because the pattern of motion in animals is different than that in humans [56], [67], [61]. Establishing a motion correction model which would work across a wide spectrum of small animal models poses great difficulty as the pattern of motion varies widely. Modulation of  $k$ -space data is caused by following types of motion:

- Periodic motion like cardiac, blood flow and respiratory motion
- Random motion as caused by gastrointestinal peristalsis, eye motion and subject movement
- Bulk motion which is caused by large scale motion of the subject such as the motion of the head

Periodic motion like cardiac and respiratory motion can be reduced by prospective or retrospective gating [20]. Prospective cardiac and respiratory gating [5] rely on cardiac and respiratory signals as control signals to trigger the MRI acquisition, so that the data are acquired at the same point in the cycle. However, even with prospective gating, motion poses significant problems in small animal imaging applications [20]. For example, when the animal has an unstable ECG or respiratory cycle due to its physical condition, the acquisition trigger point may not be accurately detected leading to ghosting artifacts and poor quality images. Retrospective gating technique relies on retro-gating software and it requires specialized pulse sequence design. Blood flow effects can be reduced using techniques such as gradient moment nulling [51] and spatial presaturation [12]. Adaptive motion correction techniques using a navigator echo can be used for retrospective referencing of tissue position to correct for random or bulk motion caused by subject movement [10]. Techniques such as adaptive motion correction [34], gradient moment nulling [51], and spatial presaturation [12] require modification to the pulse sequence design and are not applicable for post-processing.

The modulation in  $k$ -space data which causes the motion artifacts in MRI occurs only in one direction (i.e., the phase encode direction). By acquiring multiple datasets with different phase encode directions image information is correlated between the data sets but the modulation caused by motion is uncorrelated. Previous works have exploited this property to reduce ghosting artifacts [35], [70]. These methods use two or more scans obtained over the same field of view (FOV) but with the phase encode direction and readout directions interchanged. The advantages of these methods are that no a priori knowledge about the type of motion is required for

their implementation. They are post processing techniques and no changes in pulse sequence or hardware are needed for their implementation. However, these studies used the same slice-select directions [35], [70]. In most small animal imaging studies both long axis (coronal or sagittal) and short axis (axial) images of the region of interest (ROI) are obtained. The concept of using two MRI images acquired over the same region of interest using different slice-select directions (i.e., orthogonal views) is explored in this dissertation.

## **1.2 Statement of Problem Studied in this Dissertation**

The overall goal of this dissertation was to study the use of multiple imaging views for improving image quality in small animal MR imaging studies. In many small animal imaging studies, multiple imaging views are already obtained as part of the normal workflow but the information taken from one view is not generally combined with that from another view. Therefore, our goal was to evaluate imaging post-processing techniques that could make use of multiple low resolution image acquisitions for

1. increasing resolution in through-plane 3D images and
2. to reduce motion artifacts in in-plane 2D images.

More specifically, the aim is to find a technique that can use all the pre collected data to reduce image reconstruction errors in orthogonal SRR or to reduce motion artifacts.

### 1.3 Overview of the Dissertation

Chapter 2 of this dissertation deals in detail with the evaluation of different SRR acquisition geometry. Chapter 2 discusses whether SRR with a minimal number of LR views would be useful for morphological evaluations of *in vivo* animal models. The effects of various LR acquisition geometry (shifted, rotation, and orthogonal) and the number of LR image stacks with different voxel ARs have on SRR are explored. For this study, quantitative and qualitative evaluations of SRR images were performed using a resolution (line pair) and a biological (*ex vivo* embryo) phantom. Image quality was assessed by comparing the SRR images to a HR 3D isotropically acquired image. SRR was also implemented for an *in vivo* animal imaging application.

Chapter 3 of this thesis describes the development of a post processing method that aims to use multiple LR image stacks available in SRR algorithm, and make use of gradient information from orthogonal scans to improve the interpolation of another image stack and to reduce streaking artifacts in SR reconstructed image. Chapter 3 explores two ways of solving the reconstruction artifacts in orthogonal SRR, adding additional oblique LR views to the 3-view orthogonal super resolution and a sigmoid based interpolation model which is modulated by the local gradient profile of orthogonal datasets. Experiments are carried out using phantom and *in vivo* mouse. Both qualitative (visual inspection) and quantitative measures are used for comparison of the images.

Chapter 4 of this thesis outlines the development of a post processing method that aims to use two orthogonal views obtained with different slice-select directions to correct for motion artifacts in-plane 2D images. In particular, the focus is on deriving a motion correction method with no external hardware requirements but

without an increase in acquisition time over conventional scans. Simulated phantom experiment, *ex vivo* and *in vivo* experiments are carried out and improvement in image quality is evaluated.

Acronyms	Definitions
AR	Aspect ratio
CNR	Contrast-to-noise ratio
DW	Diffusion weighted
EPI	Echo-planar imaging
FA	Flip angle
FDR	False discovery rate
FOR	False omission rate
FOV	Field of view
FVE	Fractional volume error
FWHM	Full width at half maximum
GD	Gadopentetate dimeglumine
HR	High resolution
LR	Low resolution
MRI	Magnetic resonance imaging
MSE	Mean square error
NPV	Negative predictive values
PBS	Phosphate buffered saline
PPV	Positive predictive values
RE	Rand error
RI	Rand index
RMS	Root mean square deviation
ROI	Region of interest
SNR	Signal-to-noise ratio
SRR	Super resolution reconstruction
TE	Echo time
TR	Repetition time

Table 1.1: List of abbreviations used in the thesis

## Chapter 2: In Depth Comparison of SR Acquisition Geometries and Trade-offs Involved

### 2.1 Introduction

MRI is more frequently being used for evaluating morphological phenotypes in genetically engineered mouse models of disease [7]. Three-dimensional imaging at the highest spatial resolution is the preferred approach for comparing morphological phenotypes, however it is not always possible in small animal *in vivo* imaging settings. This is due to the long acquisition times required to achieve high spatial resolution in all directions. Several factors limit obtaining high resolution 3D isotropic images in the *in vivo* settings such as the length of time a mouse can be kept under anesthesia, motion artifacts that are likely to occur during long acquisition protocols that degrade image quality, and increased repetition times required at the high magnetic field strengths used for small animal imaging. Even though the high magnetic field strength increases the SNR, it is not enough to resolve small anatomical details in all directions in small animal studies. Keeping animals under anesthesia for long periods of time (>2 hrs) is not desirable. MRI acquisition protocols with very long repetition times (TR>1500 ms) such as T2-weighted, diffusion-weighted (DW), and inversion recovery imaging are particularly affected by the long scan times required for 3D isotropic

imaging. Thus, *in vivo* MR images in small animal studies are usually acquired using 2D multi-slice acquisitions with in-plane pixel dimensions (50-100  $\mu\text{m}$ ) which are 5-10 times greater than the through-plane dimension (slice thickness) in the slice-select direction (500-1000  $\mu\text{m}$ ).

Multi-slice 2D images suffer from the effects of partial volume averaging due to their increased slice thickness and when reformatted and viewed from a perspective other than the in-plane acquisition direction, the features often appear blurry due to decreased resolution in the slice-select direction. Increasing the resolution in the slice-select direction comes at the expense of decreased SNR due to the smaller voxel size (fewer spins in the voxel to generate the signal). SNR is directly proportional to voxel size, and the square root of number of signal averages. Therefore, in order to compensate for a decrease in SNR due to a decrease in voxel size, the number of signal averages must be increased by a factor and thus an increase in acquisition time. Decreasing the slice thickness also requires increasing the number of slices in order to cover the same FOV which also results in increased acquisition time. This trade-off between spatial resolution, acceptable SNR, and image acquisition time is always a consideration when imaging live subjects. MRI acquisition techniques, such as parallel imaging [15] and partial Fourier imaging [41] have been proposed for speeding up acquisition times so that higher resolution images can be acquired. These techniques require specialized hardware and software such as array coils and specialized acquisition sequence for implementation and are not always available for small animal MRI applications. Super resolution reconstruction is an image post-processing approach that has been proposed to improve the resolution in the slice-select direction in 2D multi-slice MRI data sets [17]. It is based on reconstructing a

high resolution (HR) image volume from a set of low resolution (LR) image stacks that were obtained from different viewpoints of the same FOV. Its application is not limited by the availability of acquisition hardware or specialized acquisition sequences and can be used in many multi-slice acquisition setting including those that utilize high-speed acquisition protocols, such as parallel or partial Fourier imaging.

The SRR approaches proposed thus far for MRI have differed primarily in the orientation of the acquisition geometry of the set of LR image stacks and the iterative optimization technique used for SRR. Greenspan et al. [17] proposed collecting a set of LR image stacks by subpixel shifting the 2D multi-slice stack acquisitions in the slice-select direction. Irani and Peleg's iterative backprojection method (IBP) [28] was then used to reconstruct the HR image from the shifted LR stacks. For this method, the number of LR image stacks required to reconstruct an isotropic 3D HR image is directly related to the ratio of the slice thickness to the in-plane resolution of the LR images. Thus the more anisotropic the LR data acquisitions are the greater the number of LR image stacks that are required. Shilling et al. [60] proposed acquiring a set of LR image stacks by rotating the slice-select direction in equal angle sampling intervals about a central axis. Six LR image stacks, obtained at  $30^\circ$  rotational increments, were used for SRR. Additive and multiplicative iterative algebraic reconstructions were used to produce the HR image volume from the LR image stacks. Additive correction was found to be better than the multiplicative method for high noise levels. Resolution enhancement was observed in phantom studies, *ex vivo* studies, and *in vivo* human brain scans.

Souza and Senn [62] based their SR reconstructions on the acquisition of three orthogonal (i.e., coronal, sagittal, and axial) LR image stacks. IBP was also used for

reconstructing HR images from the LR image stacks in this approach. Qualitative and quantitative evaluations indicated that SRR using LR image stacks acquired orthogonally might be useful for improving spatial resolution and CNR similar to that observed using shifted and rotational geometries. Recently, Plenge et al. [52] evaluated the different optimization techniques used for SRR of MRI data. Plenge's evaluation was performed using only the rotational acquisition geometry proposed by Shilling et al. [60]. No evaluation of the affect of LR acquisition geometry on SRR has been performed. Their results indicated that reconstruction methods based on IBP and least squares optimization techniques performed better than those based on algebraic reconstruction.

Our overall goal in this chapter was to determine whether SRR with a minimal number of LR views would be useful for morphological evaluations of *in vivo* animal models. In order for SRR to be applicable in small animal phenotyping applications, the LR image stacks must be acquired in significantly less time than a comparable HR 3D isotropic acquisition and the SRR image should have comparable image quality to that observed in images obtained from a HR acquisition. To achieve this goal we investigated the effects that LR acquisition geometry (shifted, rotation, and orthogonal) and the number of LR image stacks with different voxel ARs have on SRR. For this study, quantitative and qualitative evaluations of SRR images were performed using a resolution (line pair) and a biological (*ex vivo* embryo) phantom. Image quality was assessed by comparing the SRR images to a HR 3D isotropically acquired image. SRR was also implemented for an *in vivo* animal imaging application.

## 2.2 Material and Methods

### 2.2.1 Super Resolution Reconstruction Method

All SRR images were reconstructed using the IBP approach proposed by Irani and Peleg [28]. IBP was chosen because it has been widely used for super resolution reconstruction in the past and its ease of implementation. A flowchart illustrating the IBP approach is provided in Figure 2.1. Initially an HR image volume  $\hat{G}^{(0)}$  is approximated from the average of LR image stacks,  $\{f_k\}_{k=1}^N$  that have been upsampled and geometrically transformed,  $T_k^{-1}$ , to the same orientation prior to averaging as shown in equation 2.1.

$$\hat{G}^{(0)} = \frac{1}{N} \sum_{k=1}^N T_k^{-1} [\textit{upsample} \{f_k\}] \quad (2.1)$$

$$\{\hat{f}_k^{(i)}\}_{k=1}^N = [\textit{downsample} \{T_k(G^{(i)}) * h\}] \quad (2.2)$$

Here  $f_k$  denotes the LR image stacks and  $N$  denotes the number of LR image stacks used. A temporary set of LR images,  $\{\hat{f}_k^{(0)}\}_{k=1}^N$ , is obtained from the predicted HR image,  $\hat{G}^{(0)}$ , by simulating the imaging process that includes blurring,  $h$ , and down sampling as shown in equation 2.2. For our case, a 1D Gaussian kernel with full width at half maximum (FWHM) equal to the LR slice thickness was used along the slice-select direction in the HR image for blurring because it closely matched the excitation profile used in the original image acquisition sequence. If the predicted HR image  $\hat{G}^{(0)}$  is the same as the true HR image  $G$ , then the simulated LR images  $\{\hat{f}_k^{(0)}\}_{k=1}^N$  should be equal to the observed LR images  $\{f_k\}_{k=1}^N$ . Therefore, the difference (error) between the observed and simulated LR images  $\{f_k - \hat{f}_k^{(0)}\}_{k=1}^N$  is upsampled and

backprojected on to  $\hat{G}^{(0)}$  using linear interpolation. This results in an updated HR image that can again be downsampled and the predicted LR images compared to the observed LR images (equation 2.3). These steps are iteratively repeated till the maximum error at the  $i$ th iteration is less than a preset threshold (equation 2.4). All SRR software was developed using Matlab v.2009a (MathWorks Inc., Mass USA).

$$\hat{G}^{(1)} = \hat{G}^{(0)} + \frac{1}{k} \sum_{k=1}^N \left( \text{upsample} \left\{ f_k - \hat{f}_k^{(0)} \right\} \right) \quad (2.3)$$

$$e^{(i)} = \text{Max} \left\{ \left\| f_k - \hat{f}_k^{(i)} \right\|_2 \right\}_{k=1,2,\dots,N} \quad (2.4)$$

## 2.2.2 Resolution Phantom

A resolution phantom was constructed using five cylindrical quartz capillary tubes (0.5 mm ID, 0.7 mm OD). The tubes were cut into 2.5 cm lengths and were placed side-by-side with a known separation of 0.7 mm (see illustration in Figure 2.2a). The tubes were sealed with air trapped inside the tubes, resulting in a signal void within the tubes. They were then immersed in the center of a 15 ml test tube (14 mm ID) filled with 1:30 (v:v) homogeneous mixture of gadopentetate dimeglumine (GD) Magnevist<sup>TM</sup> (Bayer Pharmaceutical, Wayne NJ) and water.

LR image stacks of the phantom were acquired using a Bruker Biospin Avance<sup>TM</sup> 500 MHz 11.7T magnet (Bruker Biospin, Karlsruhe, Germany) and a 25 mm diameter volume coil and a T1-weighted FLASH imaging sequence (TR = 348.2 ms, TE = 6 ms, FA=90, FOV = 2.6\*2.6 cm, 1 mm slice thickness, navgs = 4, number of contiguous slices = 26, acquisition time = 4 min 56 sec). The phantom was imaged at two orientations relative to the slice-select direction of the three acquisition geometries.

The first orientation was where the long axes of the tubes were positioned parallel to the Y-axis as illustrated in Figures 2.2a-c. The second orientation was where the long axes of the tubes were positioned obliquely to the slice-select direction of the acquisition geometries as illustrated in Figure 2.2d. For this orientation the tubes were rotated  $40^\circ$  in the XY-plane and  $55^\circ$  in the YZ-plane in the oblique orientation. The oblique orientation represents the most extreme case where edge reconstruction is affected due to partial volume averaging in the slice-select direction. LR image stacks were collected using an in-plane matrix size of  $128 \times 128$  and  $256 \times 256$  for voxel AR of 1:1:5 and 1:1:10, respectively. For both the orientations mentioned above the stacks were obtained using the following three acquisition geometries for sets of data acquired using two different AR: 1) Five sets of LR image stacks were acquired using 0.20 mm subpixel shifts in the slice-select direction for voxel AR of 1:1:5 and ten sets were acquired using 0.10 mm subpixel shifts in the slice-select direction for voxel AR of 1:1:10 (shifted) (Figure 2.2a), 2) six sets were acquired with  $30^\circ$  angular rotations along the slice-select direction for both ARs of 1:1:5 and 1:1:10 (rotated) (Figure 2.2b), and 3) three sets were acquired orthogonally to one another in axial, coronal and sagittal planes for both ARs of 1:1:5 and 1:1:10 (orthogonal) (Figure 2.2c). SRR images were calculated for each acquisition geometry using the SRR method described above.

### **2.2.2.1 Quantitative measures**

The quality of the SRR was evaluated by visual inspection of the resolution phantom in the short axis view (i.e. short axis of the tubes), where blurring in the slice-select direction is expected to be the greatest due to the low resolution sampling in that direction. Intensity line plots were obtained to better evaluate the effects of SRR

on signal intensity and edge transitions. SRR images were qualitatively compared to a high resolution image of the phantom acquired in the axial plane.

SNR, CNR and edge pixel width were commonly used for quantitative evaluation of the SRR images. In case of line phantom, SNR and CNR obtained would be fairly high as there is not much gray scale information. SNR and CNR might not be useful measures as there was no live tissue which contributes to the gray scale information in the images. So contrast of the images along the line plot with respect to the ideal contrast is used as comparison. Contrast is defined as difference between the mean maximum ( $S_{max}$  from air filled in test tube) and mean minimum ( $S_{min}$  inside quartz tube) signal intensities along the line profile chosen for intensity plots.

$$C = \overline{S_{max}} - \overline{S_{min}} \quad (2.5)$$

Edge profiles were measured by nonlinear least-square fitting a sigmoid function of the form [17], [60], [52].

$$f = a_1 + \frac{a_2}{1 + \exp(-a_3(x - a_4))} \quad (2.6)$$

The edge width in high resolution pixels is computed by

$$Edge\ Width\ [Pixels] = \frac{4.4}{a_3} \quad (2.7)$$

After fitting using the equation 2.6, a measure of rise length is calculated using equation 2.7. It is defined as the width (in high resolution pixels) from 10% to 90% of edge height. An estimate of resolution can be obtained from these edge widths. The mean edge width was calculated from 5 edge profiles obtained across the

boundary between the quart tubes and the air trapped inside the test tube as showed in Figure 2.3.

### 2.2.3 Biological Phantom

An *ex vivo* E17.5 wild type embryo was used as a biological phantom for evaluating the effects of SRR on live subject MRIs. It possesses anatomic structures similar to that observed in live animals but does not suffer from motion artifacts observed in *in vivo* imaging. It is also possible to obtain an isotropic high resolution volume image of the *ex vivo* embryo for comparison to the SRR images. The E17.5 embryo was fixed and stained for 2 hours using a 20:1 volume ratio of 4% paraformaldehyde and Phosphate-buffered saline PBS:GD solution. It was then stabilized and stored in 15 ml of 200:1 PBS:GD solution prior to imaging. For MR imaging the embryo was suspended in a 15 ml tube of Fluorinert<sup>TM</sup> FC-70(3M Company, St. Paul MN).

The LR image stacks of the *ex vivo* embryo were obtained using a Bruker Biospin Avance<sup>TM</sup> 500 MHz 11.7T magnet (Bruker Biospin, Karlsruhe, Germany) and a 25 mm diameter volume coil and T1-weighted FLASH imaging sequence (TR = 519.5 ms, TE = 4 ms, FA = 30.0, FOV = 2.2\*2.2 cm, matrix = 512\*512, navgs = 1, acquisition time = 3 min) and two different slice thicknesses, 0.19 mm (voxel AR = 1:1:4, number of contiguous slices = 64) and 0.26 mm (voxel AR = 1:1:6, number of contiguous slices = 46). Two additional slice thicknesses were evaluated for the orthogonal acquisition geometry, 0.38 mm (voxel AR = 1:1:8, number of contiguous slices = 32) and 0.46 mm (voxel AR = 1:1:10, number of contiguous slices = 26). LR image stacks were obtained using the acquisition geometries outlined above: 1) Four sets of LR image stacks were acquired using 0.0475 mm subpixel shifts in the

slice-select direction for a voxel AR 1:1:4 and six sets were acquired using 0.0433 mm subpixel shifts in the slice-select direction for a voxel AR 1:1:6 (shifted), 2) six sets were acquired with 30° angular rotations along the slice-select direction for both ARs of 1:1:4 and 1:1:6 (rotated), and 3) three sets were acquired orthogonal to one another in axial, coronal and sagittal planes for ARs of 1:1:4, 1:1:6, 1:1:8, and 1:1:10 (orthogonal). The embryo was positioned such that the sub-pixel shifts were done along the X-axis for the shifted geometry and around the Z-axis for the rotational geometry (Figure 2.4). SRR images were calculated for each LR acquisition geometry using the SRR method described above.

3D isotropic volume images of the same embryo were acquired for comparison to the SRR images. A T1-weighted 3D FLASH sequence (TR = 11.3 ms, TE = 4.0 ms, FA = 20.0 , FOV = 2.2\*2.2\*1.2 cm, matrix = 512\*512\*256, navgs = 1, acquisition time = 18.5 min) was used for the 3D imaging. The 3D image obtained from this acquisition protocol results in a high quality image that is routinely used for biological phenotyping of *ex vivo* embryos in our laboratory.

### 2.2.3.1 Quantitative measures

SRR images were qualitatively compared to the isotropically acquired 3D image of the biological phantom. SNR, CNR and edge pixel width were used for quantitative evaluation of the SRR images. SNR and contrast-to-noise ratio ( $CNR_{H-L}$ ) were calculated using 9\*9\*9 voxel regions within homogenous regions of tissue illustrated in Figure 2.5. SNR was calculated using the following equation:

$$SNR = \frac{S}{\sigma_n} \quad (2.8)$$

where  $S$  is the mean signal intensity (regions selected in brain as shown in Figure 2.5) and  $\sigma_n$  is the standard deviation of the noise (from background as shown in Figure 2.5). CNR was calculated using the following equation:

$$CNR_{hl} = \frac{|S_h - S_l|}{Max(\sigma_h, \sigma_l)} \quad (2.9)$$

where  $S_l$ ,  $S_h$  and  $\sigma_l$ ,  $\sigma_h$  are mean signal intensity and standard deviation in low and high signal intensity ROIs. Following the procedure described in 2.2.2.1, the mean edge width was calculated from 20 edge profiles obtained across the liver boundary as illustrated in Figure 2.5.

#### **2.2.4 *In vivo* Experiment**

MR imaging of a live mouse was performed using a Bruker Biospin Avance<sup>TM</sup> 400 MHz 9.4T magnet (Bruker Biospin, Karlsruhe, Germany). All animal protocols were approved by the Institutional Laboratory Care and Use Committee of The Ohio State University. The mouse was placed prone on a temperature controlled mouse bed and inserted into the 35 mm diameter quadrature volume coil. The mouse was anesthetized with 2.5% isoflurane mixed with 1 liter per minute carbogen and maintained with 1-1.5% isoflurane during imaging. The respiration and temperature of the animal were monitored during the course of the experiment using a Small Animal Monitoring and Gating System (Model 1025, Small Animals Instruments, Inc. Stony Brook, NY). A bolus of 11  $\mu$ l of 11.2 mg iron oxide I.V. (Feridex, AMAH Pharmaceuticals, Lexington MA) per 1 ml PBS was injected via tail vein approximately 20 min. prior to imaging. An orthogonal set of LR image stacks (voxel AR of 1:1:10) of the live mouse were acquired using a respiratory-gated T1-weighted FLASH imaging

sequence (TR = 200 ms, TE = 2.72 ms, FA = 55.0, FOV = 2.5\*2.5 cm, navgs = 8, matrix = 256\*256, 1 mm slice thickness, acquisition time = 15 min). Contiguous slices covering 25 mm of the upper abdominal region were acquired.

## 2.3 Results

### 2.3.1 Resolution Phantom

Short-axis images of the resolution phantom (voxel AR = 1:1:5) where the long axis of the tubes were positioned along the Y-axis of Figure 2.2 are shown in Figure 2.6a-e. The lack of resolution in the slice-select direction is apparent in Figure 2.6a, where the 2D images are acquired at a slice thickness greater than the distance between the tubes and linear interpolation is used for reconstruction. Figure 2.6b-d are the corresponding short axis images from the SRR images based on shifted, rotated, and orthogonal acquisition geometries, respectively. The five tubes are resolved in the SRR images based on all three acquisition geometries, however a significant blurring is observed in the slice-select direction for the SRR image based on parallel shifts (Figure 2.6b) and to a lesser extent for the SRR image based on rotational acquisition (Figure 2.6c). The SRR image based on orthogonal acquisition (Figure 2.6d) reproduced the five tubes with the least amount of blurring artifact and looked similar to that observed in the in-plane short-axis image (Figure 2.6e), where the sampling rate is great enough to resolve the tubes in the image. The intensity line plot shown in Figure 2.6f illustrates a decrease in peak intensities in the SRR images relative to that observed for the in-plane image, with the least amount of change observed in the SRR image based on the orthogonal acquisition geometry. Similar results were

observed for the SRR HR images when the LR image stacks were collected with a voxel AR of 1:1:10 (Figure 2.7).

Short axis images of the line pair phantom (voxel AR = 1:1:5) where the long axes of the tubes were aligned oblique to the slice-select direction of the acquisition geometries are shown in Figure 2.6g-k. The lack of resolution in the slice-select direction is observed in Figure 2.6g, where the 2D images are acquired at a slice thickness greater than the distance between the spaced tubes. The five tubes are not resolved in the reconstruction based on the parallel shift acquisition geometry (Figure 2.6h), but are resolved in the reconstructions based on rotational (Figure 2.6i) and orthogonal (Figure 2.6j) acquisition geometry. However, blurring is observed in the slice-select direction of the SRR image based on rotational acquisition geometry but not in the SRR image based on orthogonal acquisition geometry. This is better illustrated in the intensity line plot presented in Figure 2.6l. Similar results were observed for low resolution data sets collected with a voxel AR of 1:1:10 (Figure 2.7).

Mean edge width and contrast along the line profile for the SRR images and the HR image of the line pair phantom are listed in Table 2.1. An increase in mean width was observed for the SR images based on orthogonal geometry at AR of 1:1:5, 1:1:5(oblique), 1:1:10 and 1:1:10(oblique). The relative contrast for the SRR images were greatest for the SRR images based on the orthogonal geometry followed by SRR images based on the rotated and shifted geometries.

### **2.3.2 Biological Phantom**

Increased resolution of biological structures in the *ex vivo* embryo was observed in the SRR images over a single LR image stack using straight linear interpolation

Mean Edge Width (in HR pixels)				
AR	Int <sup>b</sup>	Shifted	Rotated	Orthogonal
	1:1:1 <sup>a</sup>		1.7	
1:1:5	4.6	4.1	3.9	2.8
1:1:10	9.7	8.9	7.8	6.1
	1:1:1(oblique) <sup>a</sup>		4.2	
1:1:5(oblique)	5.3	4.7	4.0	3.9
1:1:10(oblique)	10.2	9.3	8.1	6.6
Contrast (with respect to HR image)				
AR	Int <sup>b</sup>	Shifted	Rotated	Orthogonal
	1:1:1 <sup>a</sup>		201(100%)	
1:1:5	43(22%)	51(25%)	56(28%)	116(58%)
1:1:10	46(23%)	69(34%)	99(49%)	127(63%)
	1:1:1(oblique) <sup>a</sup>		130(100%)	
1:1:5(oblique)	68(53%)	71(55%)	75(58%)	94(73%)
1:1:10(oblique)	6(5%)	24(19%)	73(56%)	97(75%)

a – isotropically acquired 3D image

b – linear interpolation from LR image stack

Table 2.1: Quantitative measures of image quality calculated from line phantom

(Figure 2.8). This was true for the SRR images based on LR image stacks acquired at both 0.19 mm (AR = 1:1:4) and 0.26 mm (AR = 1:1:6) slice thickness. Small structures (1-2 mm in width), such as those highlighted in the sinuses and the vertebrae, were not as clearly delineated in the SRR images as that observed in the isotropically acquired 3D image (Figure 2.8e).

The SRR image based on rotational geometry appeared more smooth than those based on the shifted and orthogonal geometries. This smoothing effect increased when the slice thickness of the LR images was increased from 0.19 mm (AR of 1:1:4) to 0.26 mm (AR of 1:1:6). Streaking artifacts were observed in uniform regions of the SRR images based on shifted (Figure 2.8b) and orthogonal (Figure 2.8d) geometries but were not as apparent in the SRR image based on rotational geometry (Figure 2.8c). These streaking artifacts were observed in the direction of linear interpolation used for upsampling in the LR direction in the iterative backprojection algorithm.

The SRR images based on orthogonal acquisition for different voxel ARs are shown in Figure 2.9. The SRR images exhibited increased streaking artifacts with increasing slice thickness. Once the slice thickness was increased beyond voxel AR of 1:1:6, we observed structures from adjacent slices that were not located in their proper through-plane location (Figure 2.9d). This artifact was not consistently observed with increasing slice thickness, as can be seen in Figure 2.9e, suggesting the artifact is dependent upon where those structures are positioned in the original LR sampling.

Mean edge width, SNR, CNR and acquisition time for the SRR images and the isotropically acquired image of the *ex vivo* embryo are listed in Table 2.2. SNR and CNR increased for SRR images with increasing voxel AR. The SNR and the CNR for the SRR images were greatest for the SRR images based on the orthogonal geometry followed by SRR images based on the rotated and shifted geometries. Mean edge width was similar for SRR images with voxel ARs of 1:1:4 and 1:1:6, but an increase was observed for the SR images based on orthogonal geometry at increased voxel AR of 1:1:8 and 1:1:10.

### 2.3.3 *In vivo* Experiment

A 3D volume rendering of the SRR image of the live mouse is presented in Figure 2.10. Biological structures, such as the wall of the stomach, kidneys, and liver vasculature are clearly observed in all three image planes of the SRR image. A 3D volume rendering based on the sagittally acquired LR image with linear interpolation illustrates the loss of image quality in planes other than the primary HR acquisition plane. The streaking artifacts normally observed in the 2D slice view of the SRR images obtained from orthogonal acquisition are not observed in the volume rendered images because of the ray projection used for rendering in Vol suite. The total time taken to acquire all three LR image stacks used for the *in vivo* SRR was 45 minutes due to the respiratory and cardiac gating. A full 3D isotropic scan of this mouse would have taken more than 4 hrs with gating and would not be possible for live animal applications.

## 2.4 Discussion

The results from this study illustrate that SRR using multiple LR views improves image content and spatial resolution in the slice-select direction of 2D multi-slice acquisitions. In the resolution phantom, improvement in mean edge width and contrast were observed in SRR images based on orthogonal and rotational acquisition geometry when compared with shifted SRR and interpolated images. In line pair phantom experiments the blurring in the slice select direction was caused by inter-voxel mixing and the improvement in mean edge width and the contrast help in reducing the blurring and resolution of quartz tubes. Increased SNR and CNR were observed in the SRR images from the orthogonal acquisition compared to those reconstructed using

shifted and rotational geometries. SRR images based on rotational acquisition geometry exhibited a smoothing of the edges in both the resolution phantom and biological phantom. This was observed visually and in the mean edge width calculated from the SRR images. However, streaking artifacts were observed in the SRR images based on shifted and orthogonal geometries that became more pronounced at the higher ARs of 1:1:8 and 1:1:10. These streaking artifacts appear to be due to the linear interpolation used for upsampling the LR images and updated differences in LR and predicted HR images. Use of higher order or standard sigmoid-shaped interpolation kernels did not improve this streaking artifact.

Streaking artifacts may not be as apparent in the SRR images based on rotational geometry because the linear interpolation is occurring at oblique angles to the view plane or they may be blurred due to the number of rotational angles used for the SRR. Streaking artifacts were only observed in 2D slice views of the SRR images and not the volume rendered images. This suggests that the ray tracing used for creating the volume rendered image has also reduced the appearance of the streaking artifacts.

The main advantage of using orthogonal acquisition for SRR over the other proposed acquisition geometries is that it requires the minimum number of views and thus the minimum amount of acquisition time. Additionally, orthogonal or nearly orthogonal acquisitions are typically acquired in most clinical and small animal imaging applications. SRR based on orthogonal views may result in better 3D volumes than those based on the other two geometries because the high resolution volume space is more uniformly sampled in all three directions.

Theoretically, SRR images based on three views is an under-determined problem when the slice thickness is greater than three times the in-plane voxel size ( $AR =$

1:1:3). Practically, the image quality of SRR images based on the orthogonal geometry and limited number of views was not significantly affected until the slice thickness of the LR image stacks was greater than six times the in-plane voxel size (AR = 1:1:6). This was also observed in orthogonal super resolution reconstructions of a digital brain phantom by Gholipour [13].

Whole body mouse phenotyping is typically performed in *ex vivo* specimens [7]. However, phenotyping in live animals has significant advantages in that you can observe structures in their native environment and monitor changes in structure and function over time. The main factors that affect the acquisition of HR images in live mice are the large FOV required for the whole body and the gated acquisitions required for respiratory and cardiac motion. We have successfully demonstrated that SRR can be implemented in a live animal model that requires respiratory- and ECG-gating to account for motion. A full 3D isotropic acquisition of the mouse used in this study would have taken more than 4 hrs with gating and would not be possible in a live animal imaging setting. This SRR acquisition was limited to an AR of 1:1:10 which is common for 2D multi-slice *in vivo* imaging applications. Visual comparison of different phenotypes using volume rendering would be possible at this resolution however image post-processing such as object segmentation and quantitative analysis may suffer from the reconstruction artifacts observed in SRR images obtained at higher ARs.

SRR has been shown to be useful in clinical applications where images are corrupted by motion such as fetal brain imaging in-utero [14], [57], [36] and imaging of the tongue [72]. These approaches use registration to align the data to an anatomical model. Gholipour et al. [14] developed a model based super resolution reconstruction

framework using arbitrarily oriented slices in 3D acquisition space. This algorithm was applied to volume reconstructions from fetal brain MR images where inter-slice motion is prevalent. Rigid body registration was used to correct inter-slice motion using a slice-to-volume registration approach. Although this approach has shown to be effective using 2D acquisitions from arbitrary orientations, they have also suggested using multiple orthogonal or overlapped slice acquisitions for high resolution reconstructions. Woo et al. [72] used an orthogonal SRR approach to obtain high resolution 3D images of the tongue. Super resolution offered a viable alternative to obtain 3D volumes where acquisition time is limited by the involuntary motion of the tongue.

SRR has also recently been implemented for improving spatial resolution in DW imaging of the human brain using single-shot echo-planar imaging (EPI) acquisition protocols [59]. Spatial resolution in DW imaging is inherently low relative to the structures of interest and isotropic acquisition at high spatial resolution is virtually impossible due to the long scan times required for data acquisition. Although improvements to hardware and acquisition protocols have been implemented to address this problem, it still remains a challenge to obtain high resolution isotropic DW images.

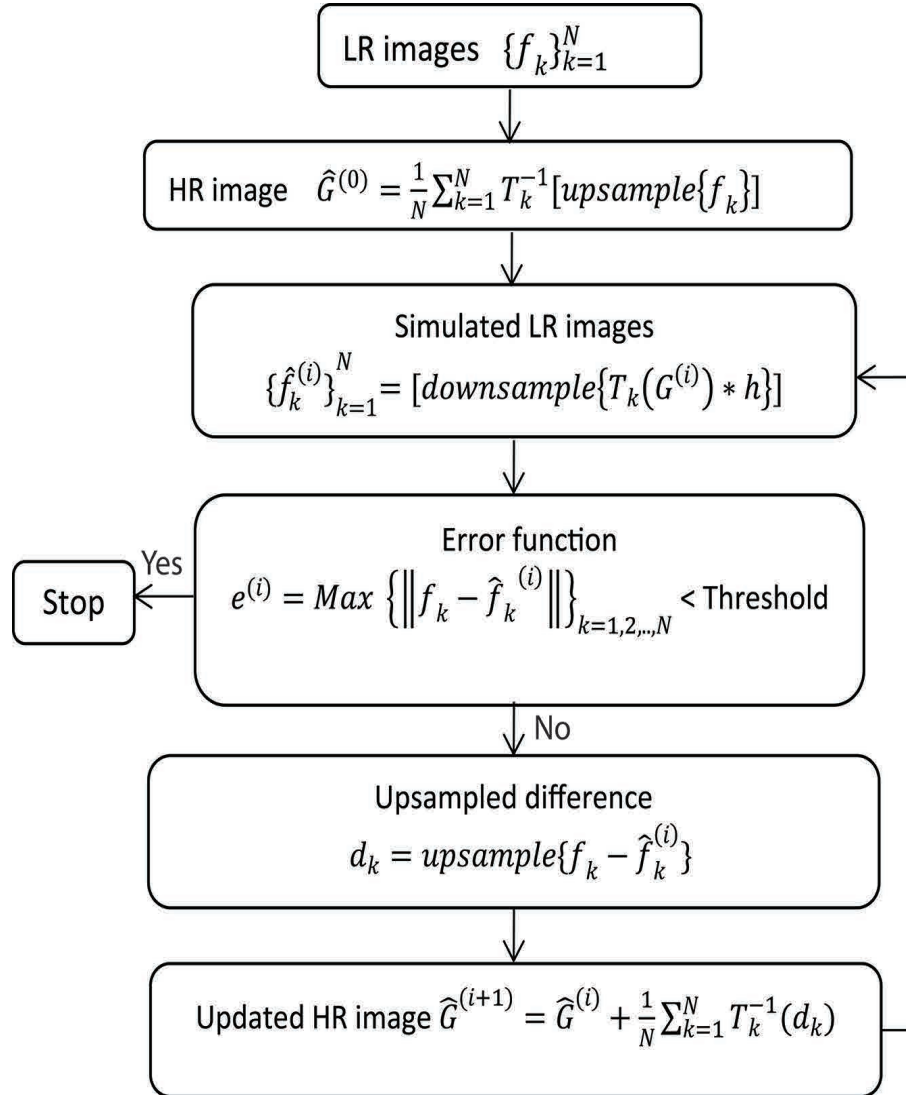


Figure 2.1: Block diagram of Irani and Peleg's IBP algorithm

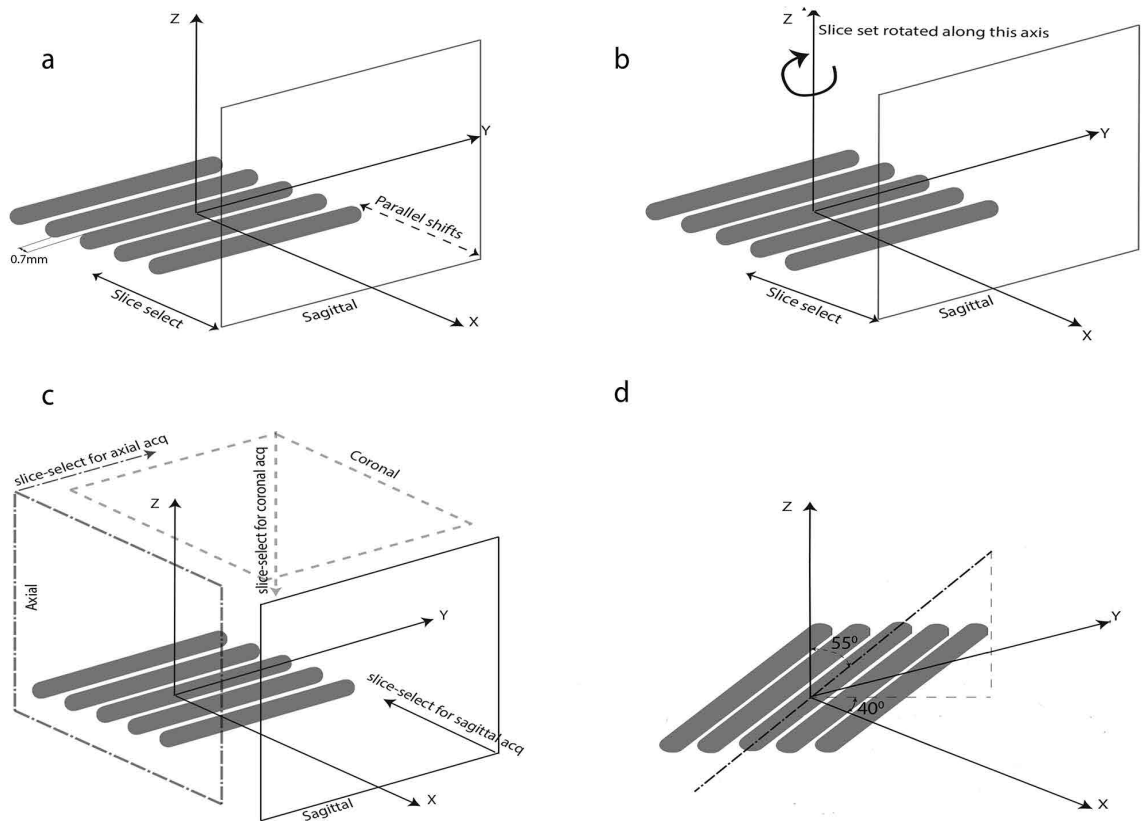


Figure 2.2: Schematic illustrating the orientation of the resolution phantom where the long axis of tubes were positioned orthogonal to the slice-select direction of the a) shifted, b) rotational, c) orthogonal acquisition geometries, and d) orientation of tubes in the resolution phantom for the oblique setup and the acquisition geometries shown in Figure 2.2a, 2.2b, 2.2c were repeated for this oblique orientation. (Axes in this image represent physical coordinates and the main magnetic field is in Z direction)

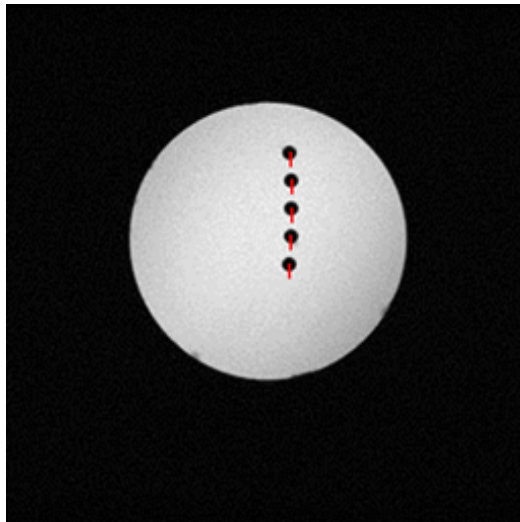


Figure 2.3: Axial view of the line pair resolution phantom illustrating sample edge profiles chosen to calculate the edge width

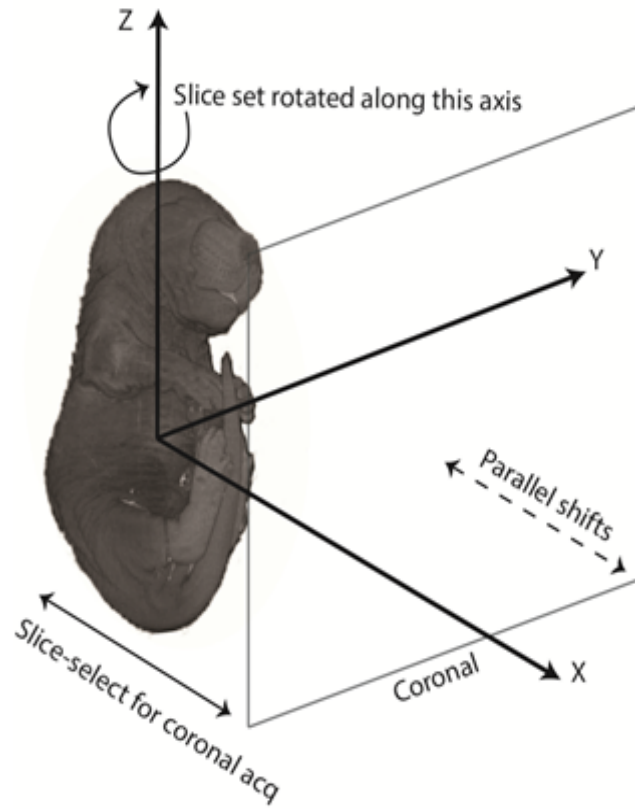


Figure 2.4: Schematic illustrating the orientation of the *ex vivo* embryo with respect to the slice-select direction of the acquisition geometries

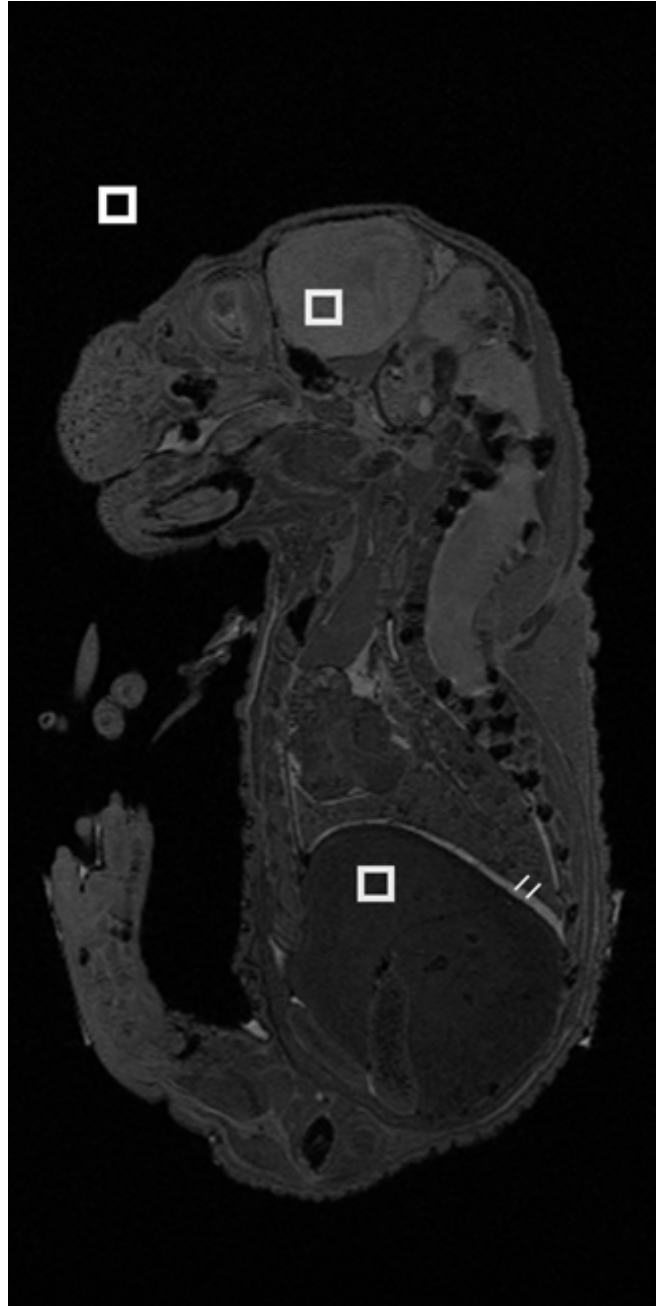


Figure 2.5: 2D slice image of the *ex vivo* embryo illustrating the location of  $9 \times 9 \times 9$  voxel ROI chosen for SNR and CNR calculations and sample edge profiles chosen to calculate the edge width

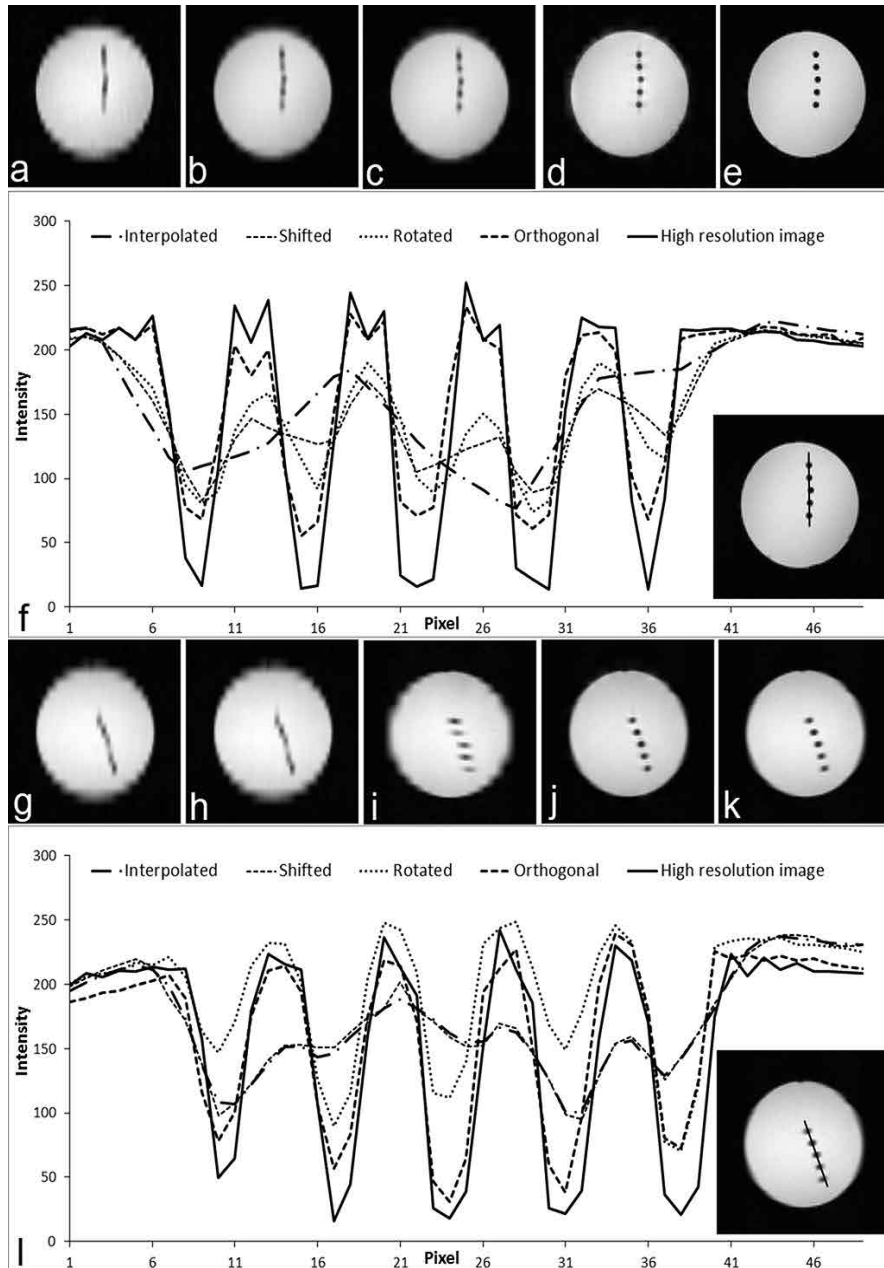


Figure 2.6: 2D slice images (Image plane represented is orthogonal to the long axis of the tube which is placed along Y-axis in Figure 2.2a) of resolution phantom where the long axis of the tubes is orthogonal to the acquisition plane and LR image stacks were collected with a voxel AR of 1:1:5: a) interpolated, b) shifted, c) rotational, d) orthogonal, e) in-plane, f) line plot, and where the long axis of the tubes is oblique to the acquisition plane: g) interpolated, h) shifted, i) rotational, j) orthogonal, k) in-plane, l) line plot

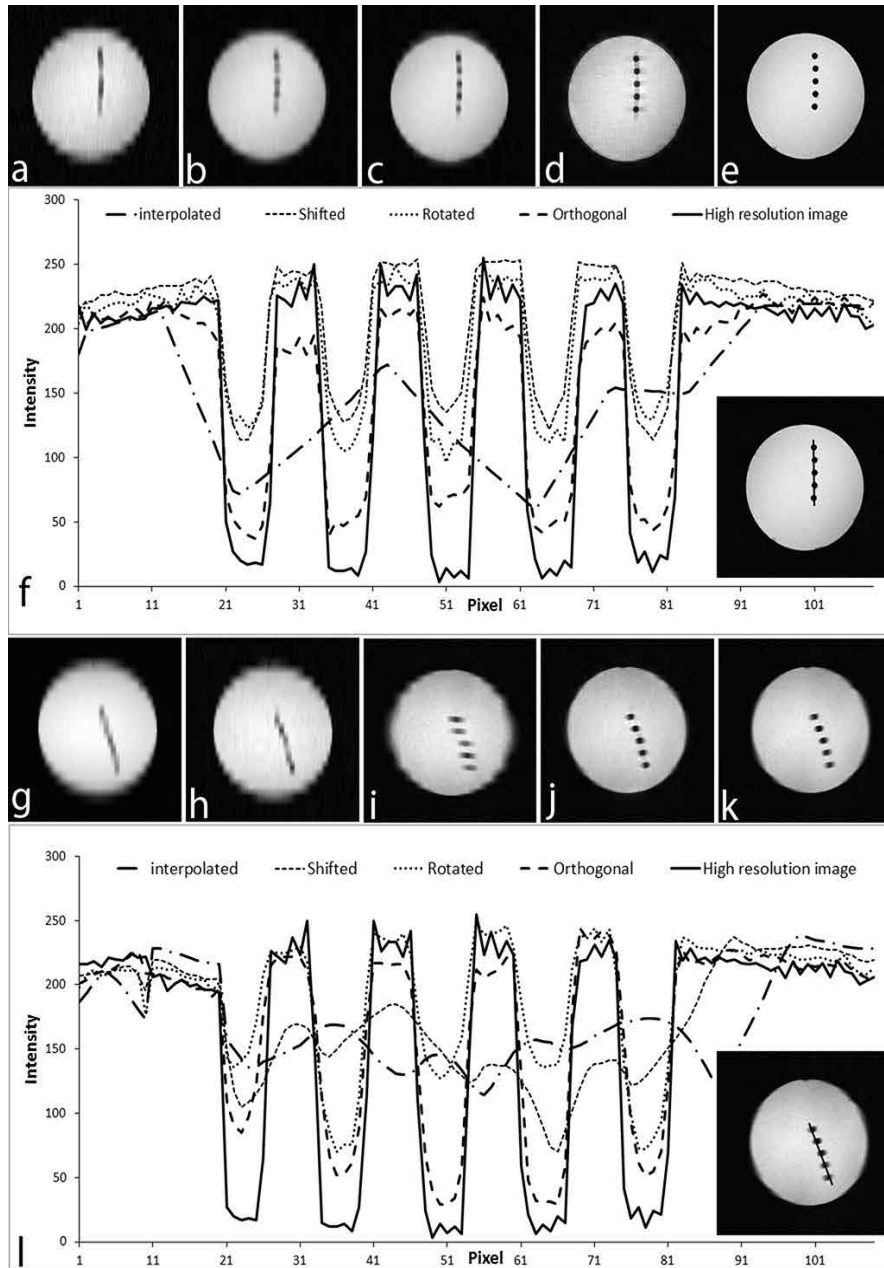


Figure 2.7: 2D slice images (Image plane represented is orthogonal to the long axis of the tube which is placed along Y-axis in Figure 2.2a) of resolution phantom where the long axis of the tubes is orthogonal to the acquisition plane and LR image stacks were collected with a voxel AR of 1:1:10: a) interpolated, b) shifted, c) rotational, d) orthogonal, e) in-plane, f) line plot, and where the long axis of the tubes is oblique to the acquisition plane: g) interpolated, h) shifted, i) rotational, j) orthogonal, k) in-plane, l) line plot

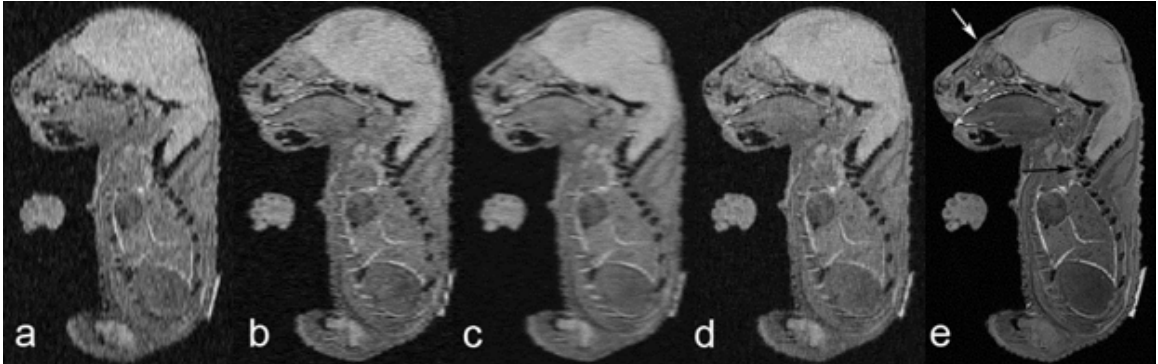


Figure 2.8: 2D sagittal view of SRR images of the *ex vivo* embryo based on different acquisition geometries: a) interpolated, b) shifted, c) rotational, d) orthogonal, e) isotropic. White arrow indicates structures in the nasal cavity not clearly observed in the corresponding SRR images

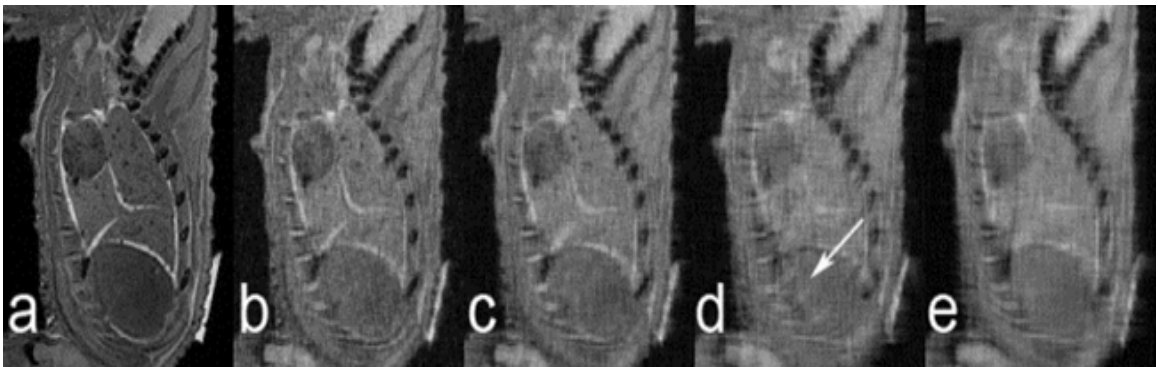


Figure 2.9: 2D sagittal view of the *ex vivo* embryo for a) 3D isotropic acquisition, and SRR images based on LR image stacks with AR equal to b) 1:1:4, c) 1:1:6, d) 1:1:8, and e) 1:1:10. White arrow highlights rib structures that are present in the SRR image but not present in the isotropic 3D image

SNR				
		1:1:1 <sup>a</sup>	26.8	
AR	Int <sup>b</sup>	Shifted	Rotated	Orthogonal
1:1:4	20.0	21.6	23.3	25.4
1:1:6	22.2	25.0	27.1	28.4
1:1:8				35.2
1:1:10				41.5
CNR				
		1:1:1 <sup>a</sup>	5.6	
AR	Int <sup>b</sup>	Shifted	Rotated	Orthogonal
1:1:4	5.1	5.3	6.0	6.9
1:1:6	5.8	6.8	7.2	8.0
1:1:8				7.9
1:1:10				7.9
Mean Edge Width (in HR pixels)				
		1:1:1 <sup>a</sup>	2.4	
AR	Int <sup>b</sup>	Shifted	Rotated	Orthogonal
1:1:4	5.9	4.2	3.7	3.2
1:1:6	6.1	4.1	3.8	3.5
1:1:8				3.9
1:1:10				4.4
Acquisition Time (mins)				
		1:1:1 <sup>a</sup>	18.5	
AR	Int <sup>b</sup>	Shifted	Rotated	Orthogonal
1:1:4	3	12	18	9
1:1:6	3	18	18	9
1:1:8				9
1:1:10				9

a – isotropically acquired 3D image

b – linear interpolation from LR image stack

Table 2.2: Quantitative measures of image quality calculated from images of biological phantom

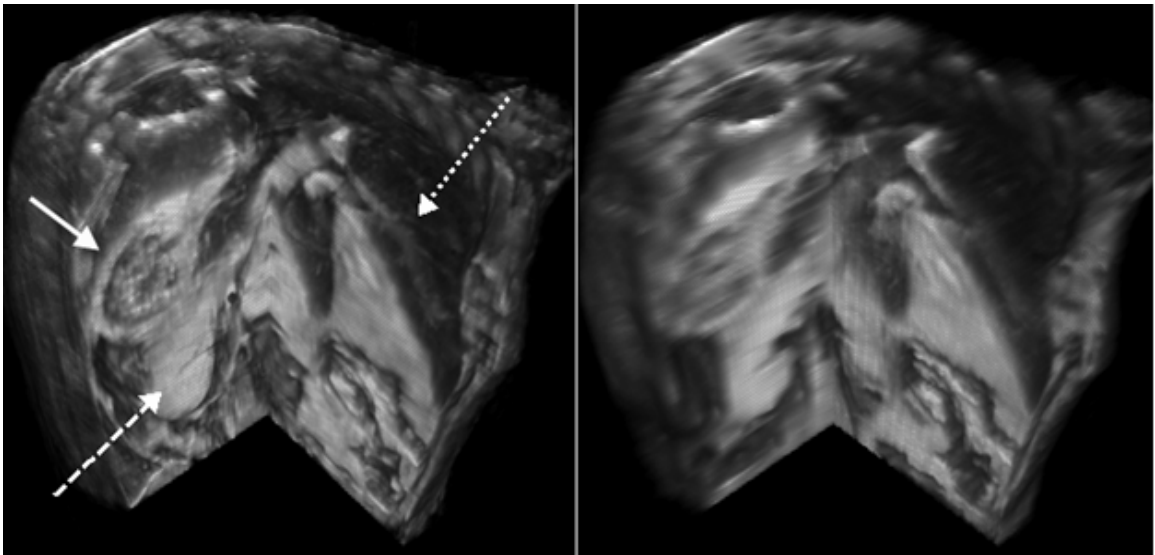


Figure 2.10: Cutaway section from 3D volume rendering of the *in vivo* mouse abdomen based on orthogonal SRR (left) with AR equal to 1:1:10 and single interpolated view (right). The solid arrow points to the wall of the stomach, dashed arrow to the kidney, and dotted arrow to the liver vasculature. Biological structures can be observed clearly in any oblique cutting plane of the SRR image as opposed to single 2D multi-slice image with linear interpolation

## Chapter 3: Addressing Streaking Artifacts in Orthogonal SRR

### 3.1 Introduction

In order for SRR to be useful in many clinical and small animal imaging applications, SRR should be implemented using LR image stacks that have ARs on the order of 1:1:5 to 1:1:10. However, SRR images based on three orthogonal views exhibited significant streaking artifacts and mislocalization when the LR data sets were acquired with a slice thickness 6 times greater than the in-plane voxel size [Figure 2.8, 2.9]. Preserving structural boundaries and reduction of the streaking artifacts is very important in making the orthogonal SRR applicable to *in vivo* applications.

Therefore, the main objective of this study was to determine whether we could develop a method for reducing the streaking artifacts and mislocalization of structures observed in SRR images reconstructed from 2D LR images with the larger voxel aspect ratio. In this chapter we explored two ways of solving this problem:

1. Adding additional oblique LR views to the 3-view orthogonal super resolution reconstruction
2. Incorporating a sigmoid based model which is modulated by the local gradient profile of orthogonal datasets. Experiments were carried out using a phantom

and *in vivo* mouse images. Both qualitative (visual inspection) and quantitative measures are used for comparison of the images

## 3.2 Method 1: Adding Additional Oblique Views

### 3.2.1 Theory

In the super resolution geometries other than orthogonal views, the number of LR images used for reconstruction can be increased to achieve fully-determined reconstruction [17], [60]. The number of LR images required for a fully-determined reconstruction is equal to the factor by which the through-plane resolution is improved [60]. But in SRR by orthogonal views, 3 sets of low resolution images are used, irrespective of the factor by which through-plane resolution is improved. As a result, SRR by orthogonal views is an under-determined problem.

In the orthogonal super resolution, the images have high resolution for in-plane directions and low resolution along the through-plane direction (the number of samples in the high resolution directions is  $N_h$  and number of samples in low resolution direction (number of slices) is  $N_l$ ). Assuming the FOV is same in all direction, if there are three orthogonal LR stacks and number of samples in in-plane direction is  $(N_h)^2$  then the number of measurements available for orthogonal SR reconstruction is given by  $M = (N_h)^2 * N_l * 3$ . The number of samples ( $U$ ) to be estimated to reconstruct a 3D isotropic image is equal to  $(N_h)^3$ . The necessary condition for the signal recovery is  $M \geq U$  (for a fully-determined reconstruction  $M = U$ , for over-determined reconstruction  $M > U$ , and for a under-determined reconstruction  $M < U$ ).

SRR based on three views is an under-determined problem when the slice thickness is greater than three times the in-plane voxel size (AR = 1:1:3). However, visual

evaluation of the results of preliminary studies done with *ex vivo* embryos shows that the image quality of SRR images based on the orthogonal geometry was not significantly affected until the slice thickness of the LR image stacks was greater than six times the in-plane voxel size ( $AR = 1:1:6$ ) and the 3D dataset produced by orthogonal SRR was comparable to that of isotropically acquired HR data set [Figure 2.9]. The above observation gives us a reason to believe that the addition of one or two oblique LR image stacks might be enough to provide a reasonable increase in image quality for AR greater than 1:1:6. For example to reconstruct a 3D isotropic dataset from LR views with ARs of 1:1:10, four to five LR views might be enough to produce an image with reasonable image quality comparable with that of an isotropically acquired high resolution 3D image.

Theoretically adding LR views to orthogonal images that are obtained from different viewpoints of the same FOV will increase the image quality, but these LR multi-slice images can be acquired using different orientations. The LR image can be obtained by shifting by sub-pixel along the through-plane direction, or by rotating along an axis or at an angle oblique to the orthogonal orientations. Shifting by subpixel corresponds to increasing the sampling density after convolving with slice excitation profile thus resulting in over sampling [17]. Acquiring at rotational increments or at an angle allows combining scans with different slice-selection direction and the slice-select direction of each image is oriented in a different direction in the 3D frequency spectrum, so combining these images will produce a 3D image with high spatial frequencies [60]. It was observed by Plenge et al. that the rotational SRR acquisition geometry is advantageous over the shifted acquisitions [52].

## 3.2.2 Experiments

### 3.2.2.1 Simulated Shepp-Logan phantom

Shepp-Logan is a standard phantom used to test image reconstruction algorithms in MRI. The advantage of the Shepp-Logan phantom is that it has a generally anatomical shape with no noise and with sparse gradients which facilitate testing the performance of algorithms in ideal conditions. Images of a 3D standard Shepp-Logan phantom ( $256 \times 256 \times 256$ ) were created using the available MATLAB program [33]. This standard Shepp-Logan phantom image is downsampled in the corresponding slice-select directions to simulate axial, coronal and sagittal views with ARs of 1:1:8 and 1:1:10. For example, to simulate an AR of 1:1:8 for two orthogonal image sets, we can use an axial image stack ( $256 \times 256 \times 32$ ) in which the phantom images are downsampled along z-axis by a factor of 8, and a coronal image stack ( $32 \times 256 \times 256$ ) as downsampled along x-axis by a factor of 8. LR image stacks were simulated at following oblique orientations for both the ARs (1:1:8 and 1:1:10):

- $45^\circ$  and  $135^\circ$  along an axis perpendicular to the coronal orientation. Three SRR images are reconstructed with basic orthogonal geometry (3-view ortho SRR), by adding  $45^\circ$  orientation to the basic geometry (4-view ortho SRR) and by adding both  $45^\circ$  and  $135^\circ$  to the basic orthogonal geometry (5-view ortho SRR).
- $30^\circ$ ,  $60^\circ$ ,  $120^\circ$  and  $150^\circ$  along an axis perpendicular to the coronal orientation. Five SRR images are reconstructed using basic orthogonal geometry (3-view

ortho SRR), basic with 30° (4-view ortho SRR), basic with 30° and 60° (5-view ortho SRR), basic with 30°, 60° and 120° (6-view ortho SRR) and basic geometry with 30°, 60°, 120° and 150° (7-view ortho SRR).

IBP algorithm is used for the orthogonal SRR reconstructed [28]. Multiples of 30° and 45° are chosen because these are commonly used in SRR rotational acquisition geometry [60], [52]. Both qualitative and quantitative parameters are used to compare the results with the HR 3D image.

### 3.2.2.2 Simulated biological phantom

A 3D isotropic data set (3DFLASH, TR = 11.3 ms, TE = 4.0 ms, FA = 90.0, FOV = 2.2\*2.2\*1.2 cm, matrix = 512\*512\*256, navg=4) of a gadolinium-stained E17.5 embryo was used to study the effects of SRR using oblique views. The advantage of using *ex vivo* embryo as biological phantom is discussed in 2.2.3. Three LR 2D multi-slice image stacks (voxel aspect ratio (AR) of 1:1:8 and 1:1:10) were obtained from the high resolution data set by mean subsampling in one of three orthogonal directions (axial, sagittal, coronal). Two additional LR image stacks were simulated at oblique orientations along an axis perpendicular to the through-plane directions (45° and 135° along an axis perpendicular to the coronal orientation). Iterative back projection was used for reconstructing the SRR data set from the LR image stacks (using 3 LR image stacks, 4 LR image stacks and 5 LR image stacks). Images were visually reviewed and quantitative parameters are calculated and compared to the original HR 3D data set.

### 3.2.2.3 *In vivo* experiment

For *in vivo* imaging, the live mouse is scanned using a Bruker Biospin Avance<sup>TM</sup> 400 9.4T magnet (Bruker Biospin, Karlsruhe, Germany). The mouse is prepared for imaging following the procedure outlined in 2.2.4 and placed prone on a temperature controlled mouse bed. Five set of LR image stacks (three orthogonal stacks along with 45°, 135° along an axis perpendicular to the coronal orientation) (voxel AR of 1:1:10) of the live mouse were acquired using a respiratory-gated T1-weighted FLASH imaging sequence (TR = 200 ms, TE = 2.8 ms, FA = 55.0, FOV = 2.5\*2.5 cm, navgs = 4, matrix = 256\*256, 1 mm slice thickness, acquisition time = 7.5 min). The respiration and temperature of the animal are monitored during the course of the experiment. Contiguous slices covering 25 mm of the upper abdominal region were acquired. Images were visually reviewed and quantitative parameters calculated from SRR images are compared to the HR image acquired from in-plane view as acquiring 3D HR image in *in vivo* settings is difficult.

### 3.2.3 Quantitative Measures

The image quality of the SRR image is evaluated by visual inspection. SNR, CNR, mean edge width and contrast metric were commonly used for quantitative evaluation of MR images. SNR and CNR were calculated using 20\*20 pixel window within homogenous regions as shown in Figure 3.1. The mean edge width was calculated from 8 edge profiles obtained across the boundary of ellipsoid as shown in the Figure 3.1. The measurement of these parameters is discussed in detail in 2.2.2.1 and 2.2.3.1.

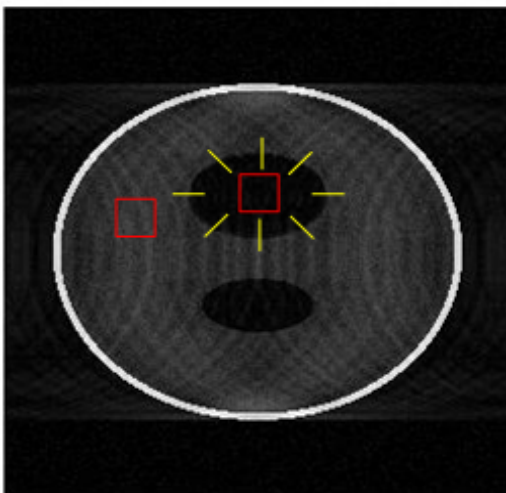


Figure 3.1: Image of SLP showing line profiles along which edge width is measured and CNR, SNR measurement windows

### 3.3 Method 2: Gradient Guided Sigmoid Based Interpolation Model

#### 3.3.1 Theory

Linear interpolation was used for upsampling the MRI images in the SRR algorithm [39]. Linear interpolation has a strong degradation for boundaries between tissues, which should have an abrupt difference in signal strength. However linear interpolation smooths boundaries as gradual (linear) transitions. Interpolations representing a high degree of upsampling cause considerable smoothing of edges. To

mitigate this problem we used the gradient information available from the corresponding orthogonal views of the same object to aid in controlling a sigmoid-based interpolation at tissue boundaries to upsample each LR image.

The sigmoid interpolation model provides a level of smoothing along the boundaries while maintaining sharp intensity contrast across the boundaries [47]. The sigmoid function used for interpolation is given below

$$S(z_i) = 1 + \exp[-\text{sgn}\{f'(z_i)\} * a * (x - \eta)] \quad (3.1)$$

The smoothness of the transition between the structural boundaries can be controlled by modifying the slope ( $a$ ) of the sigmoid interpolation kernel, and  $\eta$  allows us to choose the location of the inflection point. Using the gradients from the orthogonal views can help to better localize the inflection point instead of just assigning it to the center of the LR slice. As a part of this experiment we explore how model-based interpolation affects the location and sharpness error in SRR images.

Figure 3.2 shows the error (difference image) obtained while comparing the HR 3D image of *ex vivo* embryo and SRR result from section 2.3.2 with AR 1:1:8 (using linear interpolation) overlaid on top of the edge profile obtained from thresholding the 2D gradient magnitude (red mask) obtained from isotropic 3D HR image. It is clear that the edges are more susceptible to distortions resulting in error to be high along the structural boundaries [Figure 3.2]. Figure 3.3 shows that mislocalization of blood vessels in the liver is apparent in orthogonal SRR image reconstructed (with linear interpolation) from LR multi-slice image with AR 1:1:8 (section 2.3.2). The average image (average of three linear interpolated LR image stacks) used as starting guess for the orthogonal SRR algorithm also has similar mislocalization artifact [Figure 3.3],

which implies the artifact is not introduced by the SRR algorithm, but is because of the linear interpolation used for upsampling LR image stack with a high AR. The mislocalization observed in the axial view of the average image is also observed in the axial view of interpolated coronal image but absent in interpolated axial and sagittal images. The reason for presence of mis localized blood vessel in the interpolated coronal image stack is due to the partial volume mixing caused by through-plane interpolation. The average of two linear interpolated axial and sagittal images does not have mislocalization of blood vessels in this direction as it is high resolution direction in both the images. The effects of linear interpolation in axial and sagittal images along their through-plane direction are low in the high resolution direction of both the images. Making use of this gradient to aid the interpolation of coronal image in through-plane direction will help reducing the mislocalization artifact.

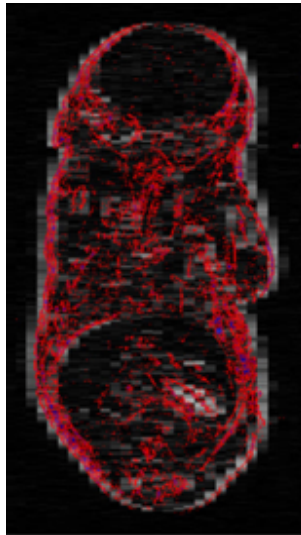


Figure 3.2: Gradient from the HR sagittal view (red mask) overlaid on the error resulting from the orthogonal SRR algorithm. Brighter the intensity, higher the error, it is evident that the homogeneous regions have lesser error when compared to the areas with higher gradients (structural boundaries or edges)

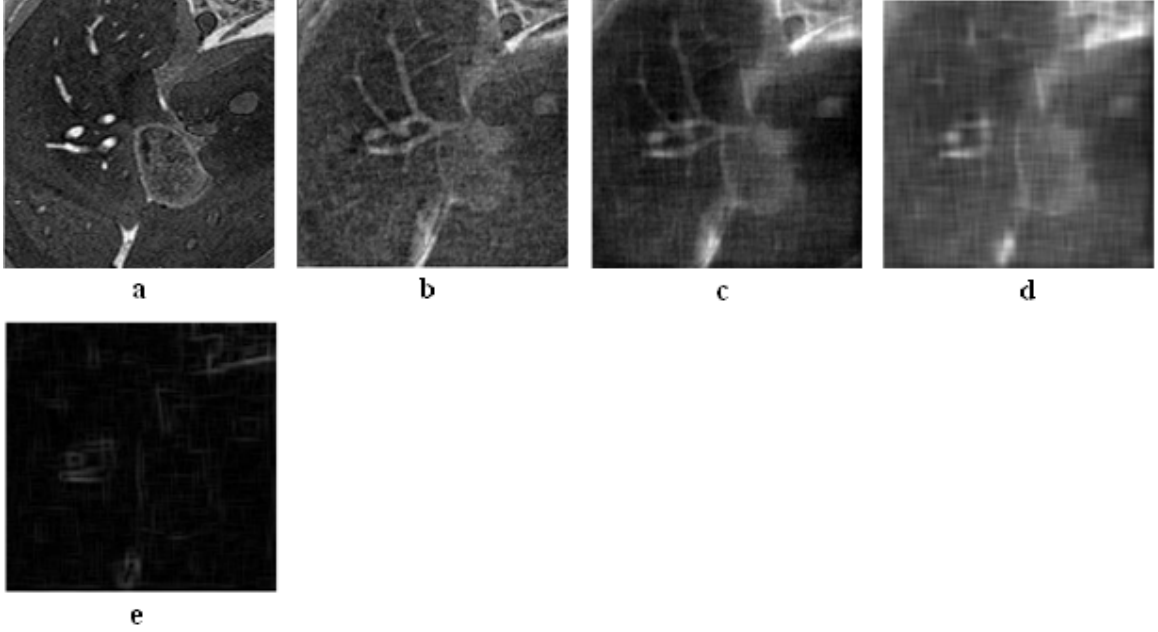


Figure 3.3: a) Isotropic 3D image of liver, b) HR volume reconstructed from LR image stacks with AR 1:1:8 by orthogonal SRR, c) average image used as initial guess for orthogonal SRR, d) average of two images orthogonal to image with partial volume mixing, e) gradients from average upsampled image

### 3.3.2 Algorithm

The step-by-step implementation of the algorithm is shown in the flow chart [Figure 3.4]. In this figure, the algorithm is using sigmoid interpolation for the LR interpolating slice-selection direction ( $z$ ) of axial images ( $I_A$ ) by using information from the sagittal images ( $I_S$ ) and coronal images ( $I_C$ ) which have high resolution in the  $z$ -direction. To find the best sigmoid interpolation for the axial LR multi-slice stack  $I_A$ , the linearly interpolated versions of sagittal  $\hat{I}_S(X, Y, Z)$  and coronal images  $\hat{I}_C(X, Y, Z)$  are averaged, and the gradient of this average image is calculated

using first order derivative masks along z-direction, which is axial slice selection direction 3.2. Here the linear interpolation of the sagittal and coronal image sets has modest effect on the z-direction, which is high resolution in both sagittal and coronal views.

$$f'(z_i) \approx \frac{f(z_i) - f(z_{i-1})}{z_i - z_{i-1}} \approx f(z_i) - f(z_{i-1}) \quad (3.2)$$

The inflection point is the position of the local maximum of magnitude of the gradient in the sampling window which occurs at  $z_{imax}$ . The position of inflection point  $\eta$  (in eq 3.1) is set as  $z_{imax} + 0.5$  as the gradients are shifted by a half pixel. The parameter  $a$  (in eq 3.1) is determined from the gradient. The parameter  $a$  linearly is mapped to the magnitude of the gradients by

$$a = a_{min} + (a_{max} - a_{min}) * \left| \frac{\nabla I_{lmax}}{\nabla I_{max}} \right| \quad (3.3)$$

Where as  $|\nabla I_{max}|$  is the maximum intensity gradient of the image,  $|\nabla I_{lmax}|$  is the local maximum of sampling window which occurs at  $z_{imax}$  and  $\frac{\nabla I_{lmax}}{\nabla I_{max}}$  is the normalized gradient.  $a_{min}$  and  $a_{max}$  delimit linear mapping between the  $|\nabla I|$  and  $a$ , so that  $a$  will fall into a user defined range.  $a_{min}$  and  $a_{max}$  are empirical values which are set as 0 and 20 for this experiment and more information on this can be found in the study carried out by Mishra et.al. [47]. Well-defined values of  $a_{min}$  and  $a_{max}$  allow adjustment of the sharpness across structural boundaries and smoothness along structural boundaries to a desired user defined level [47]. If the gradients are equal for all the points in sampling window or when local maximum occurs at more than one point in sampling window, then linear interpolation is chosen.

The method for choosing the parameters  $\eta$  and  $a$  are further explained by the following numerical example. The 1D plot of the intensity along the interpolation window (line highlighted in the Figure 3.5) is obtained from *ex vivo* biological phantom experiment outlined in section 2.2.3. The sampling window along which the data is interpolated is highlighted with line profile. The local maximum  $|\nabla I_{lmax}|$  is found to be 0.62 which occurs at  $z_{imax} = 7$  (inflection point,  $\eta = 7.5$ ). The maximum intensity gradient  $|\nabla I_{max}|$  of the image is 3.54, and by substituting these values along with  $a_{min} = 0$  and  $a_{max} = 20$  in eq 3.3, we get  $a = 3.5$ . The parameters  $\eta$  and  $a$  are substituted in sigmoid equation (eq 3.1) and plotted (Figure 3.5).

Similar interpolation procedure is repeated for interpolating sagittal and coronal orientations. To interpolate sagittal image stack the gradient from average of coronal and axial image stacks along the x-direction is used. The gradient from average of sagittal and axial images along the y-direction is used to interpolate coronal image stack in through-plane direction. The average of interpolated axial, sagittal and coronal images is used as starting guess for IBP algorithm. The SRR images are reconstructed using the IBP approach proposed by Irani and Peleg (detailed discussion in 2.2.1).

### 3.3.3 Experiments

To test the effectiveness of the sigmoid interpolation in reducing the sharpness and location errors in interpolated image, the experiments are done using simulated phantoms (3D wedge phantom, concentric sphere and simulated SLP), a biological phantom (*ex vivo* embryo) and an *in vivo* experiment. In all these experiments LR

image stacks are simulated/acquired with anisotropy factor equal to or greater than 6.

### 3.3.3.1 3D wedge phantom

A 3D wedge phantom of size  $300*300*300$  is created (Figure 3.6). The advantage of using simulated phantom is that, we have an original HR image which can be used as ground truth for comparison and wedge shape is used as it has regular geometric structure and the staircase effect caused by the interpolation is apparent along the diagonal edge separating two gray levels. Three LR 2D multi-slice image stacks were obtained from the high resolution data set by mean subsampling in one of three orthogonal directions: axial ( $300*300*50$ ), sagittal ( $50*300*300$ ), and coronal ( $300*50*300$ ). All three LR image stocks have a AR of 1:1:6. Algorithm as shown in the flowchart in Figure 3.4 is implemented in a simulated 3D wedge phantom.

### 3.3.3.2 Concentric sphere phantom

The structural boundaries present in the *in vivo* studies don't have planar boundary structure like the wedge phantom, hence a sphere phantom is used to study the effects of sigmoid interpolation on rounded boundaries with the orthogonal SRR approach. The presence of small structures can complicate the problem, so for preliminary experiment, a simulated  $256*256*256$  phantom consisting of two concentric spheres is used to study the effect of the interpolation algorithm along the surface of the sphere. Three sets of orthogonal anisotropic LR slices with the matrix size of  $256*256*42$ ,  $256*42*256$ ,  $42*256*256$  are simulated from isotropic phantom. From these three LR images orthogonal SRR images of size  $256*256*256$  are reconstructed

by linear, cubic, sigmoid interpolation followed by IBP algorithm. The 3D isotropic image of size 256\*256\*256 is used as the ground truth for comparison.

### 3.3.3.3 Simulated SLP experiment

The SLP phantom experiment simulates another case in which the acquisition model is accurately known. This SLP phantom has many small ellipsoids embedded in an outer ellipsoid, so we can study about how the interpolation algorithm affects both the surface of outer ellipsoid and the small structures within them. Three set of orthogonal anisotropic LR slices with the matrix size of 300\*300\*50, 300\*50\*300, 50\*300\*300 are simulated from 300\*300\*300 isotropic SLP volume created using MATLAB program [33]. From these three LR images orthogonal SRR images of matrix size 300\*300\*300 are reconstructed by linear, cubic, sigmoid interpolation followed by IBP algorithm. The 3D isotropic image is used as the ground truth for comparison.

### 3.3.3.4 Simulated biological phantom

The *ex vivo* embryo is used as biological phantom as it possesses anatomic structures similar to those observed in live animals but does not suffer from motion artifacts observed for *in vivo* imaging. The various advantages of using biological phantom are discussed in 2.2.3. LR image stacks with AR of 1:1:8 of an *ex vivo* E17.5 wild type embryo in obtained using the protocol described in section 2.2.3. 3D isotropic images of the same embryo were acquired using a T1-weighted 3D FLASH sequence (TR = 11.3 ms, TE = 4.0 ms, FA = 90.0, FOV = 2.2\*2.2\*1.2 cm, matrix = 512\*512\*256, navg=1). Orthogonal SRR is used to reconstruct images using linear, cubic and sigmoid interpolation.

### 3.3.3.5 *In vivo* experiment

For *in vivo* experiment, the live mouse is prepared for imaging following the procedure outlined in 2.2.4 and the mouse is laid prone so that the flank tumor is not disturbed. A T2-weighted RARE imaging sequence (TR = 4500 ms, TE = 36 ms, FA = 180, FOV=2.5\*2.5 cm, navgs = 4, rare factor = 8, matrix=256\*256, 1 mm slice thickness, acquisition time = 8 min) is used. The respiration and temperature of the animal are monitored during the course of the experiment. Contiguous slices covering 25 mm of the flank region are acquired. Images are visually reviewed and quantitative parameters calculated from SRR images are compared to the HR image acquired from in-plane view as acquiring 3D HR image for *in vivo* settings is difficult.

### 3.3.4 Quantitative Measures

Mean edge width is calculated for all experiments. SNR and CNR measurements are calculated for the *ex vivo* and *in vivo* experiments. SNR and CNR are not evaluated in 3D wedge phantom and concentric sphere as there are very few grey levels in the histogram of these images and no noise is present. A HR 3D isotropic image acquired using a direct acquisition or HR image acquired in-plane (in the case of the *in vivo* experiment) is used as ground truth for comparison. More information about the quantitative parameters can be found in 2.2.2.1 and 2.2.3.1.

The ability to correctly identify the location of inflection point (maximum gradient) in the image to be interpolated based on the gradient of the orthogonal view is very important in implementing the sigmoid interpolation. Location of the inflection point is plotted along line profiles chosen in the phantom experiments. A line profile is plotted along the surface (in the sphere experiment) and along the small structures

(in SLP experiment). The line profile of ground truth and all SRR images formed by different interpolation (linear, cubic and sigmoid) are plotted together for the comparison. Location of inflection point is not analyzed for 3D wedge phantom, biological phantom and *in vivo* experiments. Analyzing the location of inflection point will not be useful in wedge phantom as there only two grey scale levels present in the phantom. The *ex vivo* and *in vivo* experiments are acquired in the MRI scanner and therefore they are susceptible to noise. If there is too much noise in the images, the line plot over a small profile does not provide much useful information and noise affects the accuracy of the detected inflection point.

### **3.4 Results for Method 1: Adding Additional Oblique Views**

#### **3.4.1 Simulated Shepp-Logan Phantom**

##### **3.4.1.1 Qualitative evaluation**

Figure 3.7 shows the result for the addition of oblique views in  $45^\circ$  increments to the standard orthogonal geometry with LR image stacks of AR 1:1:8. The visual inspection of the image shows that all SRR images are able to resolve three ellipsoids (highlighted by arrow), but three ellipsoids are not resolved in linear interpolation. The addition of one or more oblique views reduces the streaking effect (highlighted in the Figure 3.7c and Figure 3.7d). When two oblique views are added, the image looks smoother than the 4-view ortho SRR. Similar results are observed when LR image stacks with AR of 1:1:10 are used. The SRR images reconstructed by adding oblique views in  $30^\circ$  increments to the orthogonal SRR acquisition geometry with AR of 1:1:8 are shown in Figure 3.8. The streaking artifacts observed in 3-view ortho SRR are reduced when oblique views are added. The images obtained from 6-view

and 7-view ortho SRR are smoother than the images obtained from other ortho SRRs. We observed similar results when LR image stacks with AR of 1:1:10 are used.

### 3.4.1.2 Quantitative evaluation

SNR, CNR, mean edge width, contrast metric (with respect to reference image) for SLP experiment when oblique views are listed in Table 3.1 for various SRR acquisition geometries with ARs of 1:1:8 and 1:1:10. As expected SNR increased when number of LR image stacks used is increased. The CNR and mean edge width are also improved when oblique views are added to the basic orthogonal geometry. The percentage of increase in CNR is high when first oblique view is added, for additional oblique views, the percentage goes down. The mean edge width and contrast metric remains the same for both 4-view and 5-view ortho SRR. The quantitative parameters followed similar pattern as observed in chapter 2 when AR is increased from 1:1:8 to 1:1:10. The quantitative parameters for SLP orthogonal SRR experiment with 30° incremental oblique views are listed in Table 3.2. The results show similar pattern as the SRR images with additional 45° oblique views.

## 3.4.2 Simulated Biological Phantom

### 3.4.2.1 Qualitative evaluation

Figure 3.9 shows the coronal view of the *ex vivo* embryo for the various SRR orthogonal geometries. SR reconstructed images based on three orthogonal views and one additional oblique view resulted in improved visual quality and reduced streaking artifacts in simulations based on LR data sets with voxel ARs of 1:1:8 and 1:1:10. Addition of a fifth oblique view did not improve the visual quality of the SRR image for either voxel AR. Although streaking was still apparent in SRR

images reconstructed from four LR views, the streaking was significantly less at high contrast boundary regions such as lung-liver boundary (white arrow in Figure 3.9c), whereas a typical staircase pattern due to linear interpolation is observed in the 3-view orthogonal SRR (white arrow in Figure 3.9b). In addition, the stomach wall is well defined in the four-view SRR image (yellow arrow in Figure 3.9c) and is almost similar to the ground truth (yellow arrow in Figure 3.9d), whereas the stomach wall from the three-view orthogonal SRR looks blurry (yellow arrow in Figure 3.9b).

### 3.4.2.2 Quantitative evaluation

The CNR, SNR and edge width for the simulated *ex vivo* experiment are listed in Table 3.3. As expected SNR increased when additional LR image stacks are added. The increase in SNR is higher for AR with 1:1:8 (SNR increased by 6%) when compared with AR of 1:1:10 (SNR increased by 3%). Adding one LR view to 3-view ortho SRR increased the CNR, but when one more view is added to 4-view ortho SRR, the increase in CNR is not substantial. Adding one LR view to standard orthogonal geometry has decreased the mean edge width, but 5-view ortho SRR doesn't improve the edge width substantially.

## 3.4.3 *In vivo* Experiment

### 3.4.3.1 Qualitative evaluation

Figure 3.10 shows the *in vivo* SR image reconstructed from 3 orthogonal views and one oblique view. The SRR image is compared with the HR image acquired in-plane. Visual review of Figure 3.10 shows that the spinal cord (highlighted by yellow arrow) and intestinal tract (white arrow) are clearly defined in the 4-view SRR when compared with 3-view SRR. There is no obvious improvement observed during the

visual inspection in 5-view SRR when compared with 4-view SRR. The streaking artifact apparent in 3-view ortho SRR is highlighted with red arrow, the appearance of the streaking artifact is reduced in 4-view and 5-view ortho SRR. It should be noted that streaking artifact is not completely eliminated or reduced uniformly across the image and still some of the streaking can be observed in both 4-view and 5-view ortho SRR images.

### **3.4.3.2 Quantitative evaluation**

Quantitative parameters such as CNR, SNR and mean edge width are calculated and are tabulated in Table 3.4. Adding one LR view to 3-view ortho SRR improved the CNR and mean edge width by 8% and 2% respectively. Mean edge width remained the same and CNR decreased by 4% when five LR image stacks are used. As expected SNR is increased when number of views used for the reconstruction is increased. The total acquisition time for 4-view ortho SRR is 30 minutes and adding one more view to obtain 5-view ortho SRR increases the acquisition time by 25%.

## **3.5 Results for Method 2: Gradient Guided Sigmoid Based Interpolation Model**

### **3.5.1 3D Wedge Phantom**

#### **3.5.1.1 Qualitative evaluation**

Figure 3.11 shows the 2D view of the wedge phantom reconstructed from nearest neighbor, linear, cubic and sigmoid interpolation. The edge in the result [Figure 3.11e] appears to be smoother than the other interpolation schemes. The difference between the linear and sigmoid interpolation shows [Figure 3.11f] the typical staircase in the

lower side and smooth edge in the upper side, which shows that the staircase pattern in linear interpolation is replaced by smooth edge in the sigmoid.

### **3.5.1.2 Quantitative evaluation**

The mean edge width is listed in Table 3.5. The mean edge width is increased by 29%, 19% and 10% in linear, cubic and sigmoid interpolations respectively. The lesser the mean width, better is the quality of the image.

## **3.5.2 Concentric Sphere**

### **3.5.2.1 Qualitative evaluation**

The orthogonal SRR images reconstructed from different interpolation techniques are shown in Figure 3.12. Visual inspection of the results shows that the resultant image from sigmoid interpolation is marginally better than the cubic interpolation. Both cubical and sigmoid interpolations produce SRR images which are qualitatively superior to the linear interpolation. The boundary of the sphere reconstructed by SRR-linear shows a typical staircase pattern formed by linear interpolation; the staircase pattern is reduced in case of sigmoid and cubical interpolation. The line profile which is plotted for the qualitative comparison is showed in Figure 3.12e.

### **3.5.2.2 Quantitative evaluation**

20 line profiles are considered across the boundary of the sphere for the calculation of edge width. The mean of 20 edge widths is reported in Table 3.6. The inflection points in ground truth and the inflection point (maximum change of intensity) identified based on the gradient of orthogonal views in sigmoid SRR are highlighted in the graph to verify whether they are correctly identified. The line plot shows that the inflection point of the ground truth and the inflection point identified by the

algorithm both coincides (at pixel location= 14.5) and as expected the transition of the HR image is the steepest followed by sigmoid and cubic interpolated SRR images. Edge width measurement from the Table 3.6 shows that the linear SRR has wider edge width when compared to others which makes the edges less sharp.

### **3.5.3 Simulated SLP Experiment**

#### **3.5.3.1 Qualitative evaluation**

Figure 3.13 shows all the reconstructed SRR images along with the HR image for the SLP experiment. Visual inspection of the images shows that sigmoid interpolated SRR has performed better in resolving the small ellipsoids from each other when compared with linear and cubic interpolated SRR. The structure of the ellipsoids resolved in the sigmoid interpolation image is almost comparable to that of HR image (highlighted in the Figure 3.13) whereas they are not resolved clearly in linear and cubic SRR. The line plot [Figure 3.13e] across the ellipsoid shows that the boundary between the first and second ellipsoid is not resolved clearly in linear and cubic SRR images whereas the line plot of the sigmoid SRR closely approximates the line plot of HR image.

#### **3.5.3.2 Quantitative evaluation**

Figure 3.13e shows that the inflection points in the sigmoid SRR images occur closely to those of HR image. The SNR, CNR, contrast metric (with respect to HR image) and mean edge width for the SLP experiment are listed in Table 3.7. The quantitative measurements of mean edge width suggest that edges are 19% wider in both linear and cubic SRR and 15% wider in sigmoid SRR when compared with HR edge profile. The SNR of the cubic and sigmoid interpolation schemes are higher than

the linear interpolated version. The contrast metric is reduced by 19%, 17% and 14% in linear, cubic and sigmoid SRR images respectively (with respect to HR image).

### **3.5.4 Biological Phantom**

#### **3.5.4.1 Qualitative evaluation**

The orthogonal SRR images reconstructed from different interpolation techniques along with 3D isotropic image is shown in the Figure 3.14. The visual inspection of the images shows that the boundary of the pleural cavity which is filled with contrast agent and fixative (highlighted with arrow) is clearly resolved in sigmoid interpolated SRR image when compared with cubic and linear SRR images.

#### **3.5.4.2 Quantitative evaluation**

The SNR, CNR and mean edge width are listed in the Table 3.8. The SNR and CNR of the sigmoid SRR are better than the other two interpolation schemes. The mean edge width of the sigmoid SRR is marginally better than the cubic and linear SRR images. But the mean edge width of the edge profile chosen in the sigmoid SRR is much wider than (43% wider) the HR edge width.

### **3.5.5 *In vivo* Experiment**

#### **3.5.5.1 Qualitative evaluation**

The orthogonal SRR images reconstructed from linear, sigmoid and cubic interpolation techniques along with the 3D HR image acquired in-plane is shown in the Figure 3.15. These images are acquired in *in vivo* setting so it is susceptible to motion artifacts and noise. Visual inspection of the images shows that the structures in cubic interpolated SRR are smoother than the linear SRR and certain structures

(highlighted by white and yellow arrows) are better resolved in sigmoid interpolation. The streaking is less apparent in cubic interpolated SRR.

### 3.5.5.2 Quantitative evaluation

The quantitative measures of SNR, CNR and mean edge width are given in the Table 3.9. The SNR, CNR and mean edge width of the sigmoid SRR are better than the other two interpolation schemes. But the mean edge width of the edge profile chosen in the sigmoid SRR is 94% wider than the HR edge width.

## 3.6 Discussion

The above phantom and *in vivo* experiments show that adding one oblique view improves the image quality on visual inspection, but adding more views doesn't provide substantial improvement. Adding more oblique views resulted in SRR images which appear smoother than the SRR images obtained from basic orthogonal geometry. Streaking artifacts may not be as apparent in the SRR images with oblique views because the interpolation is occurring at oblique angles to the view plane. Adding oblique views which are rotated along the phase encoding direction to the orthogonal SRR is like combining orthogonal SRR architecture with rotational SRR architecture. We have already observed in chapter 2 that in rotational SRR architecture the reconstructed images have smoother edges owing to the interpolation along the circular grid.

Adding more LR image stacks to standard orthogonal SRR architecture would result in improved quantitative parameters. It was observed from the *in vivo* results that the streaking artifacts are not uniformly reduced across the image, and this might be because of anisotropic sampling in oblique direction. Since only one/two oblique

angle is used, the whole grid is not covered uniformly by these oblique stacks. This might be the reason for reduction of streaking artifacts in certain areas when compared to other. As we have already discussed in chapter 2, in MRI studies along with views required for the study, additional views are always acquired to aid the acquisition of required geometry. It might be useful to add those views to the standard orthogonal SRR to improve the image quality. LR image stacks acquired along any angle can be added to standard orthogonal SRR architecture to improve the quality of the reconstructed image.

There is always a trade-off between the number of LR images used in SRR algorithm, image quality and the total acquisition time. Increase in LR images will enhance the quantitative parameters, even when there is no noticeable improvement in image quality detected upon visual inspection. The improvement in CNR and edge width is not substantial between 4-view and 5-view SRR. In these cases the addition of one oblique view suffices. The total acquisition time is an important parameter to consider for *in vivo* imaging. The phantom and *in vivo* experiments (AR =1:1:8, 1:1:10) indicate that the quality of an SRR image based on orthogonal acquisition may be improved by the addition of a fourth view acquired obliquely to the through-plane direction of the coronal or sagittal view and the addition of fifth oblique doesn't provide noticeable visual enhancement in image quality. Thus in this case, observed increase in image quality would be worth the minimal increase in acquisition time required for the one additional view.

When comparing between SRR with one oblique view of  $45^\circ$  and  $30^\circ$ , visual inspection shows that the results are similar, but the quantitative parameters show that the 4-view ortho SRR with  $45^\circ$  yields marginally better results. This might

be because that LR image stacks acquired along  $45^\circ$  is positioned midway between two orthogonal acquisitions. It still needs to be explored, whether adding LR view at certain angle is better than another or adding LR views oblique to one particular axis is better than the other and the optimum number of LR images to be added to the orthogonal SRR to get the required image quality with optimum increase in acquisition time.

If the resolution of LR is very poor compared to HR image (for example 10 times less), then linear interpolation is not a precise way to interpolate the image, as the relationship between the pixels are not always linear over a large interpolation window. Linear interpolation is used for upsampling in MRI images as the relationship between pixels over the upsampling window is usually not known. In case of orthogonal SRR algorithm three orthogonal views of each object are already acquired and it is advantageous to use the available information from one or two views to interpolate the orthogonal view. This gradient information can be incorporated in an interpolation model for LR images.

To summarize, the sigmoid based interpolation method using the gradient of the orthogonal view is applied in orthogonal SRR and the quantitative and qualitative evaluations are done in various phantoms and *in vivo* studies. As seen from the phantom experiments, in the absence of noise and multiple inflection points, the basic sigmoid model based interpolation described in this work has improved the location and sharpness of the edges in the reconstruction of surfaces and small objects. The quantitative and qualitative evaluation of the *in vivo* experiment shows that sigmoid SRR performs better than other two interpolation schemes. But the mean edge width of the edge profile chosen is 94% wider than the HR edge width. This might

be because of the fact that the above mentioned sigmoid SRR deals with only one inflection point identification and assignment in a single interpolation window.

Images which have very minute anatomical structures (of the order of  $40 \mu\text{m}$ ) can have multiple structures crossing in the same interpolation window which might lead to two or more inflection points owing to the presence of multiple local maximum in the gradient values. In this case assigning the location of global maximum within the interpolation window as a single inflection point will not yield good results. The accurate detection of inflection point is crucial for this algorithm which in turn dictates the location of the edges in the interpolated image both in reconstructing surfaces and small objects. Noisy images can affect the gradient measurement which can in turn affect the accuracy of the detection of inflection points. In this algorithm, the gradient from the average of two orthogonal images is used. Using the gradient from the average image essentially reduces some of the rapid changes in the intensity, which might correspond to the edges/ structures located in slightly different location in orthogonal data sets because of the partial volume averaging. Some edge profiles might be stronger in one orientation than the other because of partial volume mixing in different orientations. In using the average image we may lose the significant gradients or end up with a reduced gradient intensity corresponding to these structures. The adverse effects of the averaging is more prominent in the biological phantom and *in vivo* experiments as the images have more anatomical structures as opposed the simulated phantom with well-defined geometrical structures.

AR	Int <sup>a</sup>	3-view ortho	4- view ortho	5-view ortho	3D <sup>b</sup>
SNR					
1:1:8	27.4	32.9	34.2	35.7	45.1
1:1:10	24.1	30.5	32.6	34.4	45.1
CNR					
1:1:8	6.1	9.3	9.9	10.1	12.4
1:1:10	5.8	8.9	9.4	9.3	12.4
Mean edge width (in HR pixels)					
1:1:8	1.6	0.7	0.5	0.5	0.4
1:1:10	1.9	0.8	0.6	0.6	0.4
Contrast metric (with respect to 3D HR image)					
1:1:8	-26%	-16%	-13%	-13%	100%
1:1:10	-31%	-18%	-16%	-16%	100%

a – linear interpolated from LR image stack

b – simulated 3D SLP

Table 3.1: Quantitative parameters for the SLP with added oblique views at 45° increment

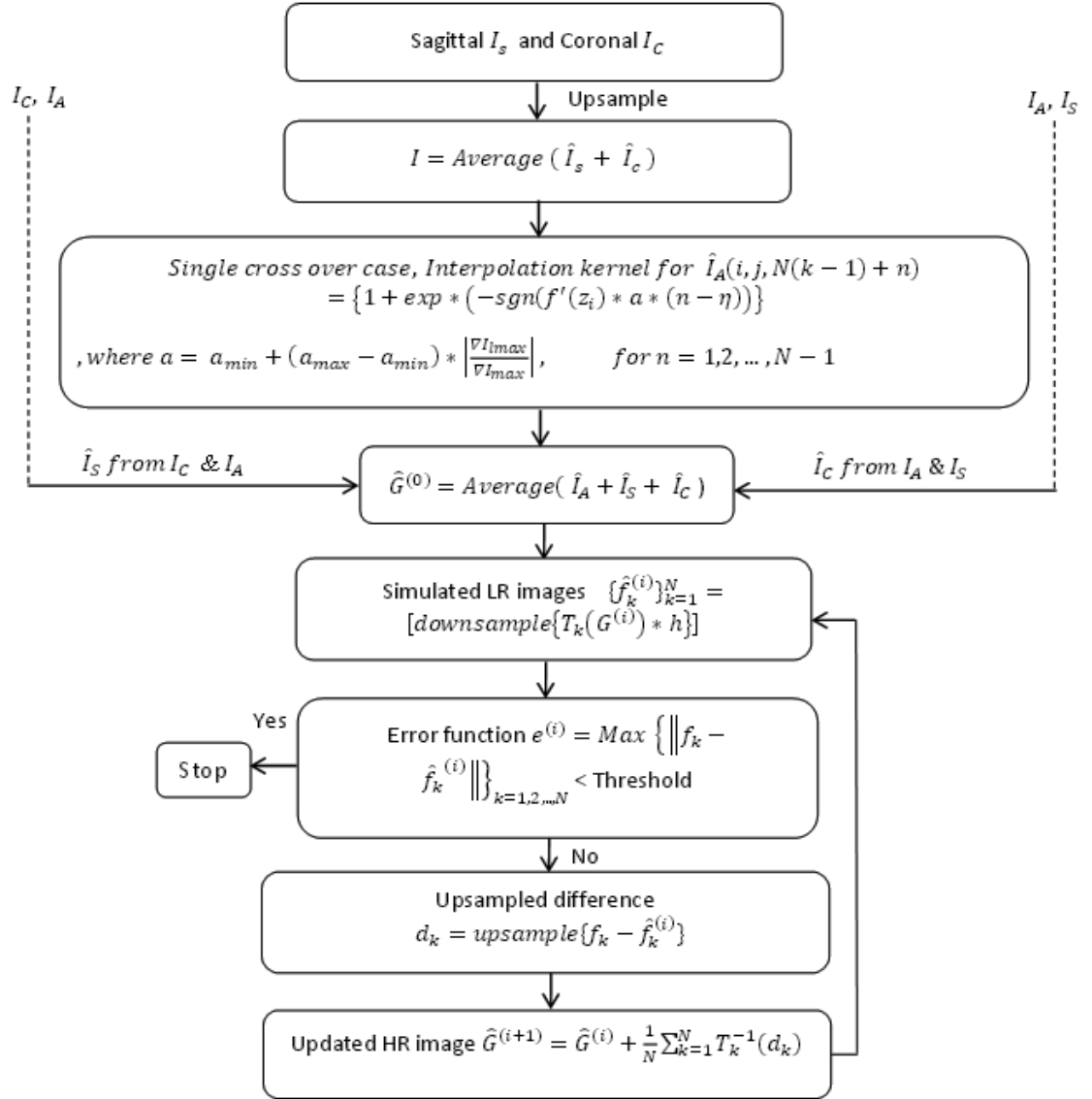


Figure 3.4: Flowchart for gradient based sigmoid interpolation in orthogonal SRR

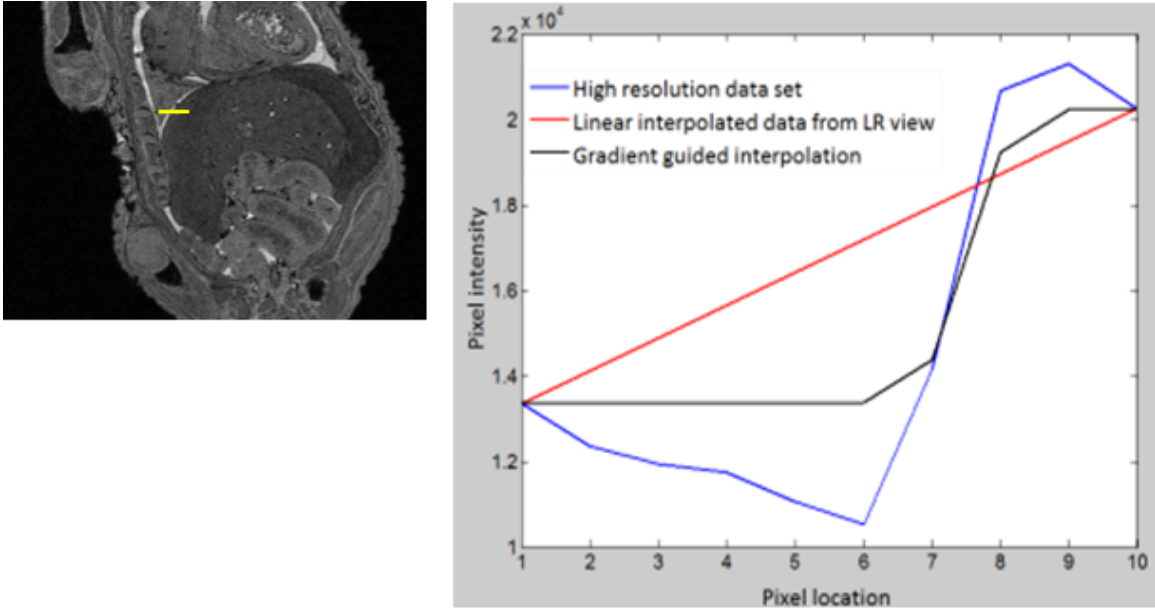


Figure 3.5: 1D line profile is highlighted in HR image (left), the plot of pixel intensities for HR image, linear interpolated image and gradient guided interpolation image along the line profile (right)

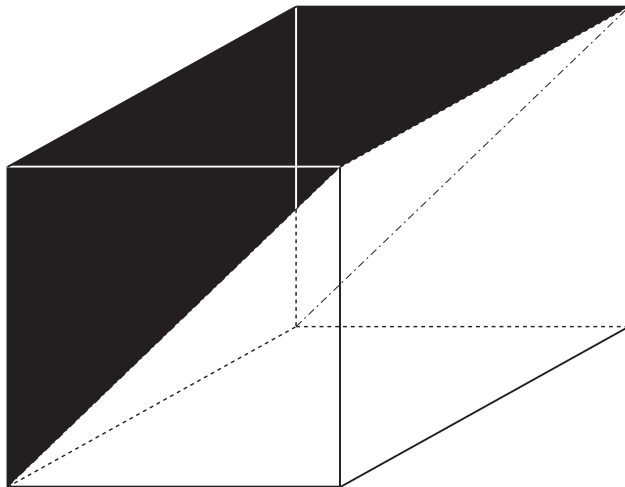


Figure 3.6: Three dimensional wedge phantom

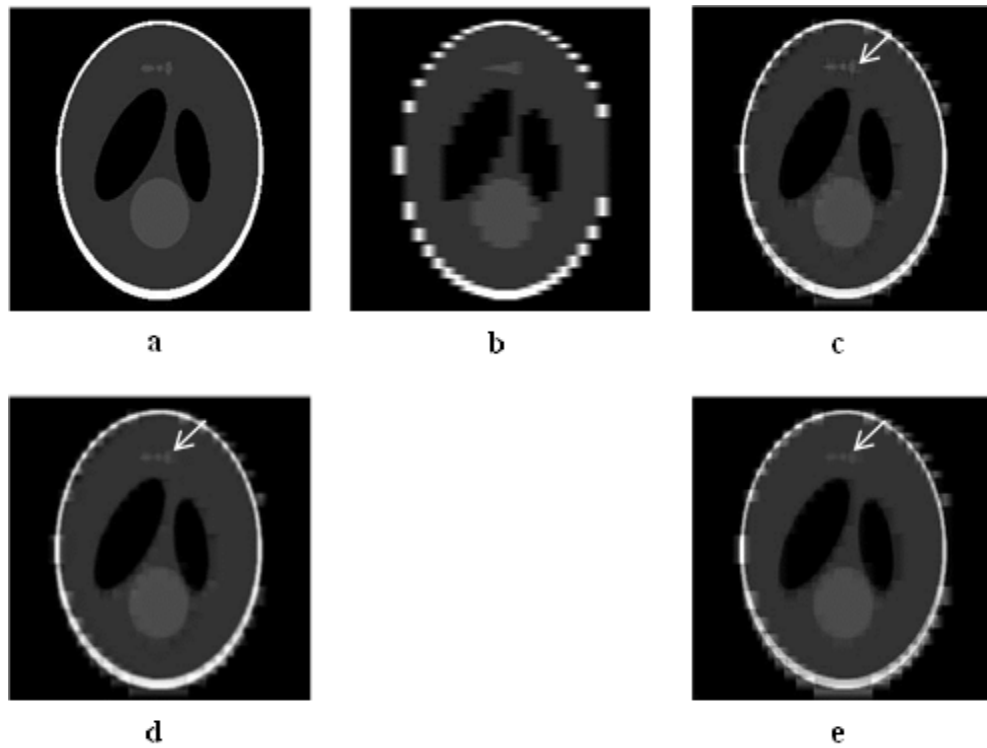


Figure 3.7: SRR orthogonal images with oblique views added at  $45^\circ$  increments; AR of LR image stack is 1:1:8 a) 3D, b) interpolated, c) 3-view ortho SRR, d) 4-view ortho SRR, e) 5-view ortho SRR. Arrow highlights the three ellipsoids which are resolved in ortho SRR but not in linear interpolated image stack

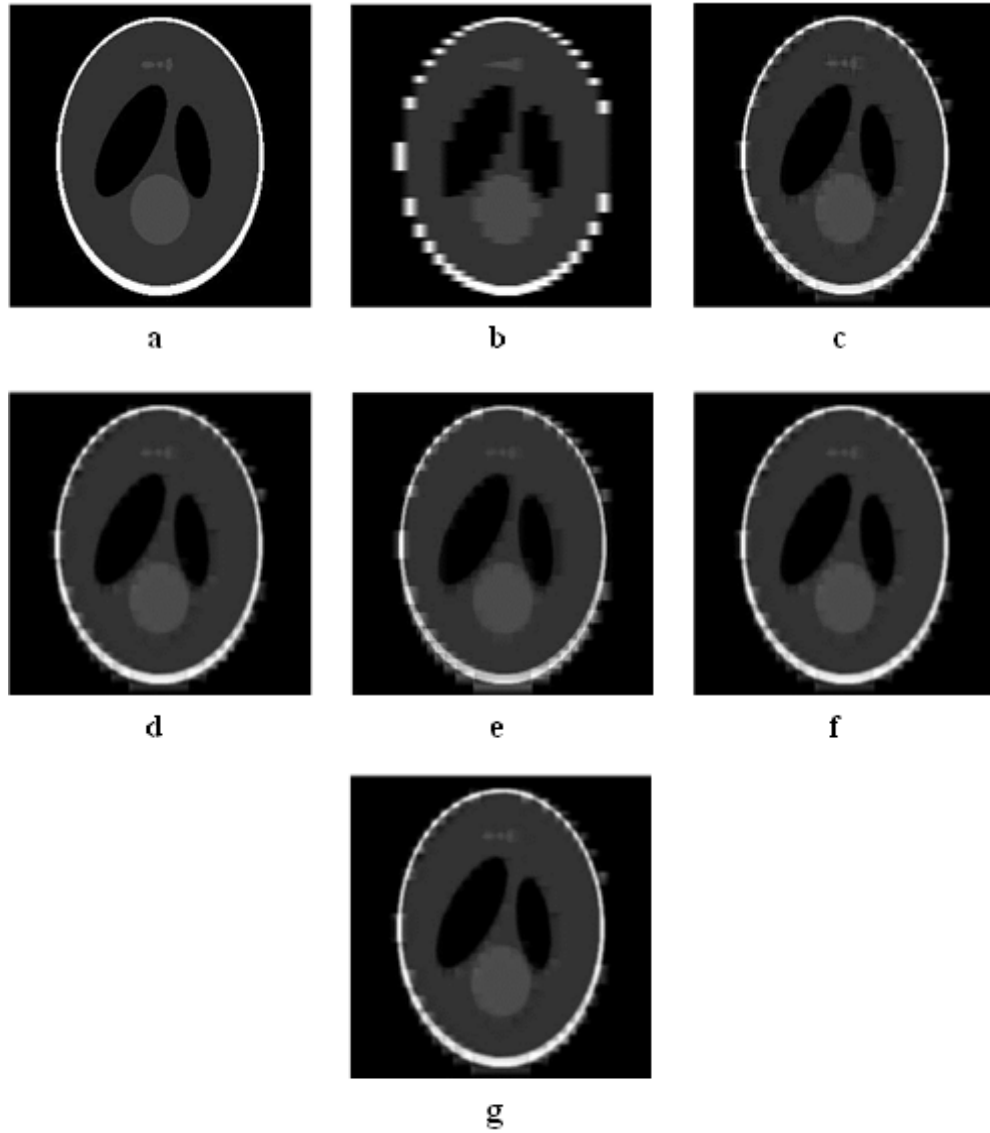


Figure 3.8: SRR orthogonal images with oblique views added at  $30^\circ$  increments; AR of LR image stack is 1:1:8 a) 3D, b) interpolated, c) 3-view ortho SRR, d) 4-view ortho SRR, e) 5-view ortho SRR, f) 6-view ortho SRR, g) 7-view ortho SRR

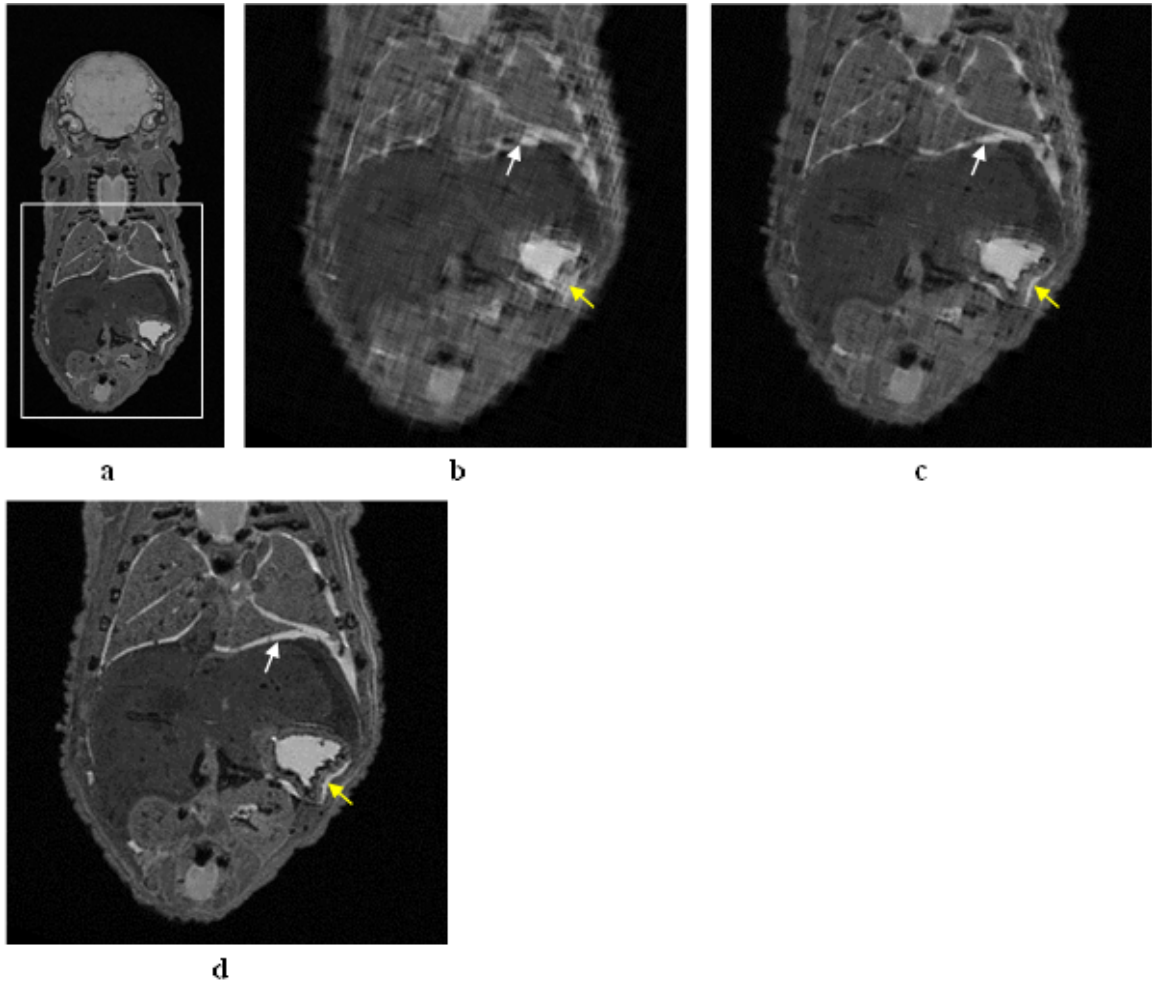


Figure 3.9: a) Isotropic 3D image and the area enlarged for the comparison is highlighted, b) HR volume simulated from LR image stacks with AR 1:1:10 by 3-view orthogonal SRR (enlarged ROI to show the area of interest), c) HR volume simulated from LR image stacks with AR 1:1:10 by 4-view orthogonal SRR, d) ground truth (isotropic 3D image). Lung-liver boundary is highlighted with white arrow and stomach wall is highlighted with yellow arrow.

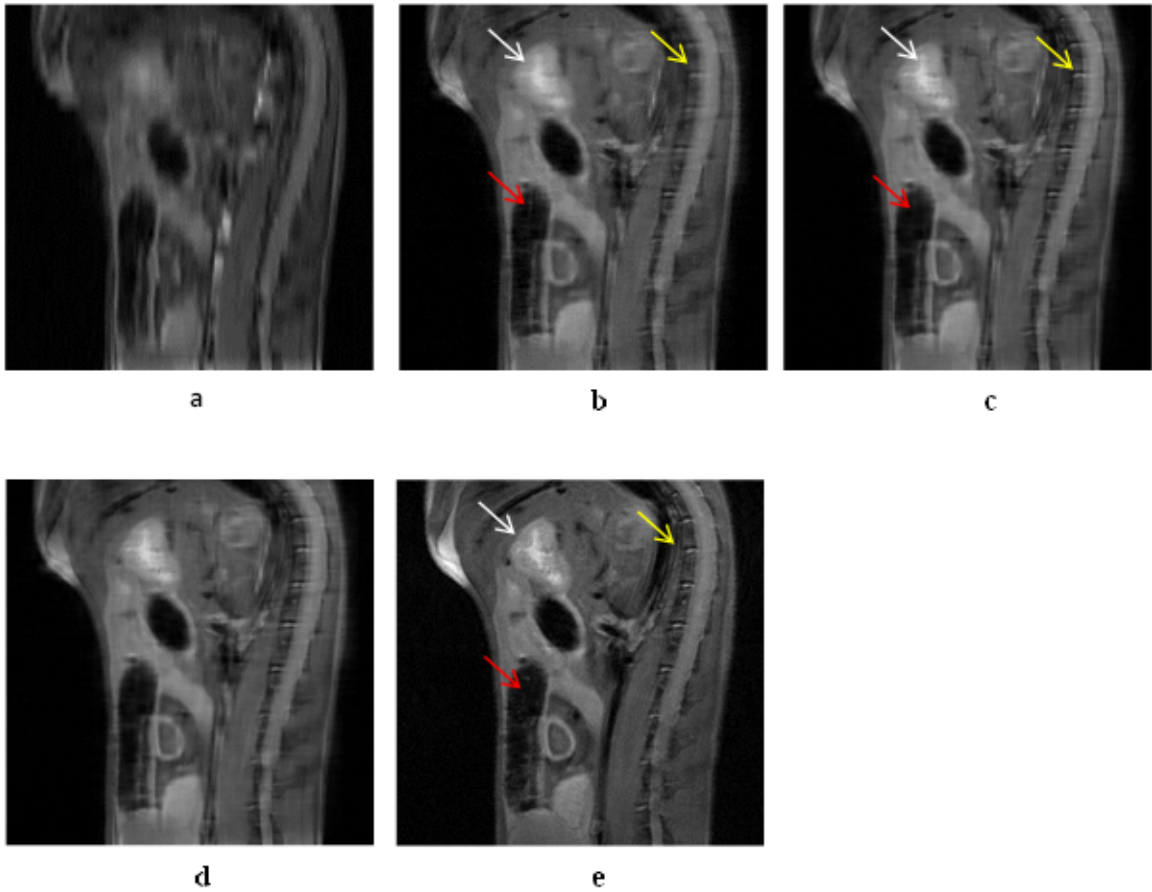


Figure 3.10: a) Interpolated image, b) HR volume reconstructed using 3-view orthogonal SRR, c) HR volume reconstructed using 4-view orthogonal SRR, d) HR volume reconstructed using 5-view orthogonal SRR, e) HR volume acquired in-plane. The spinal cord and the intestinal tract are highlighted by yellow arrow and white arrow respectively. Red arrow highlights the streaking artifact

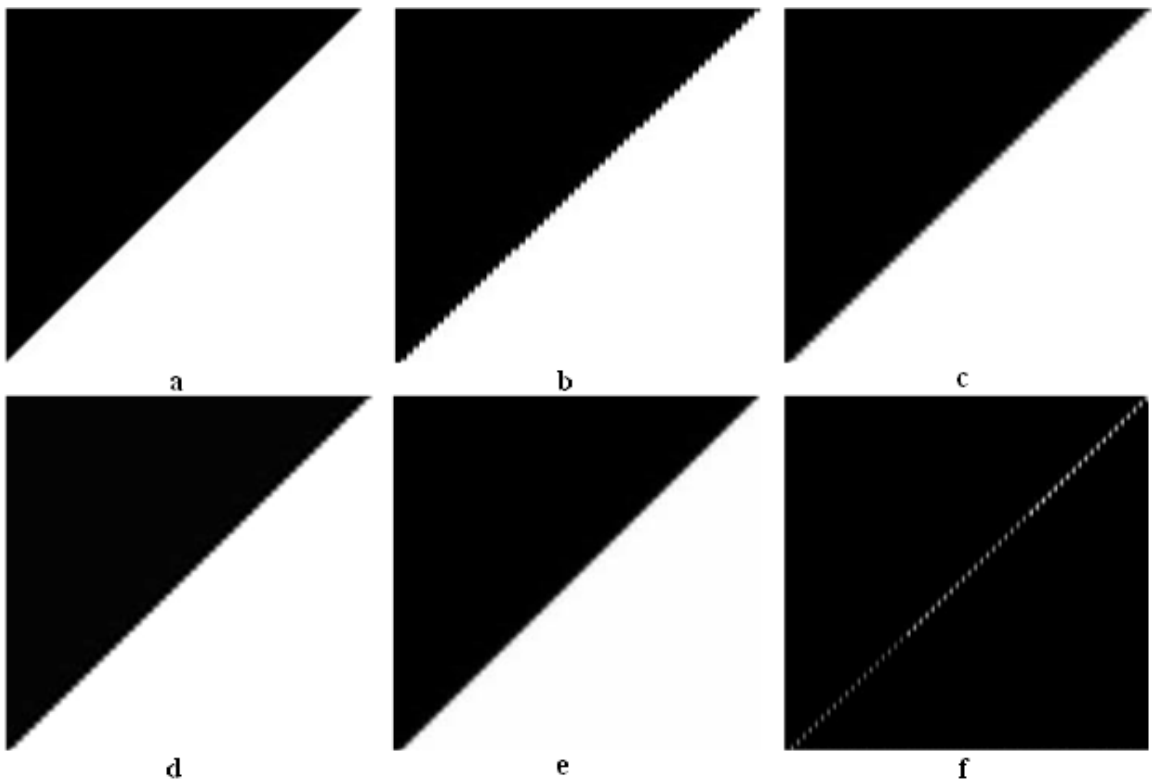


Figure 3.11: a) HR image from which LR images are simulated, LR images interpolated in through-plane direction using: b) nearest neighbor, c) linear, d) cubic, e) gradient based sigmoid interpolation, f) difference between the linear and gradient based sigmoid interpolation

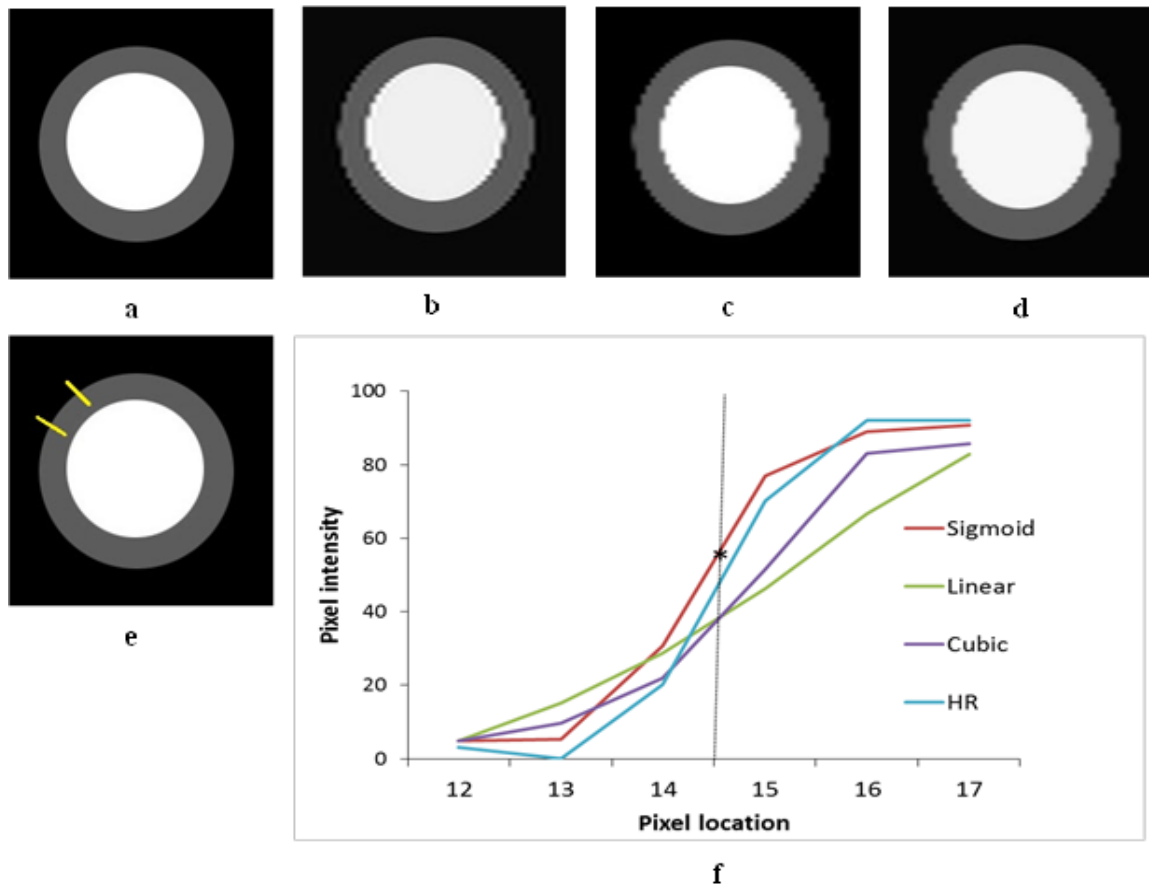


Figure 3.12: a) HR image from which LR images are simulated, orthogonal SRR images reconstructed direction using: b) linear, c) cubic, d) gradient based sigmoid interpolation, e) line profile for plotting and edge width calculation, f) line plot across the boundary of the sphere and the inflection point in the HR image and sigmoid SRR is denoted by dotted line and asterisk respectively

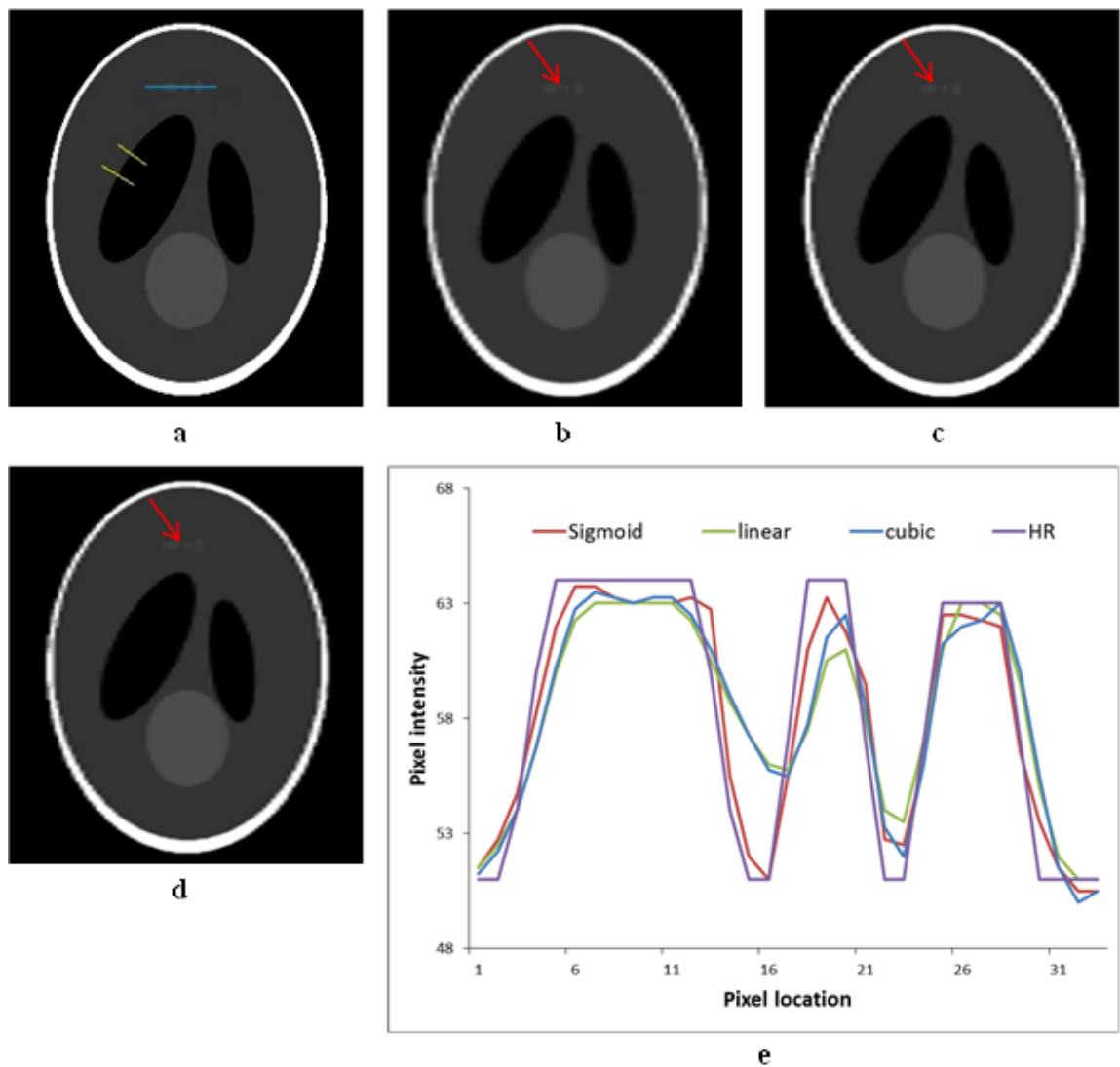


Figure 3.13: a) HR image from which LR images are simulated and the line profile (highlighted by blue line) to study the effect of SRR in small structures, and the line profiles (highlighted by yellow line) used for edge width calculations, orthogonal SRR images reconstructed using: b) linear, c) cubic, d) gradient based sigmoid interpolation, e) line profile across the boundary of the small ellipsoids, showing the location of the structures in sigmoid SRR is comparable with HR image. Red arrow highlights the three small ellipsoids

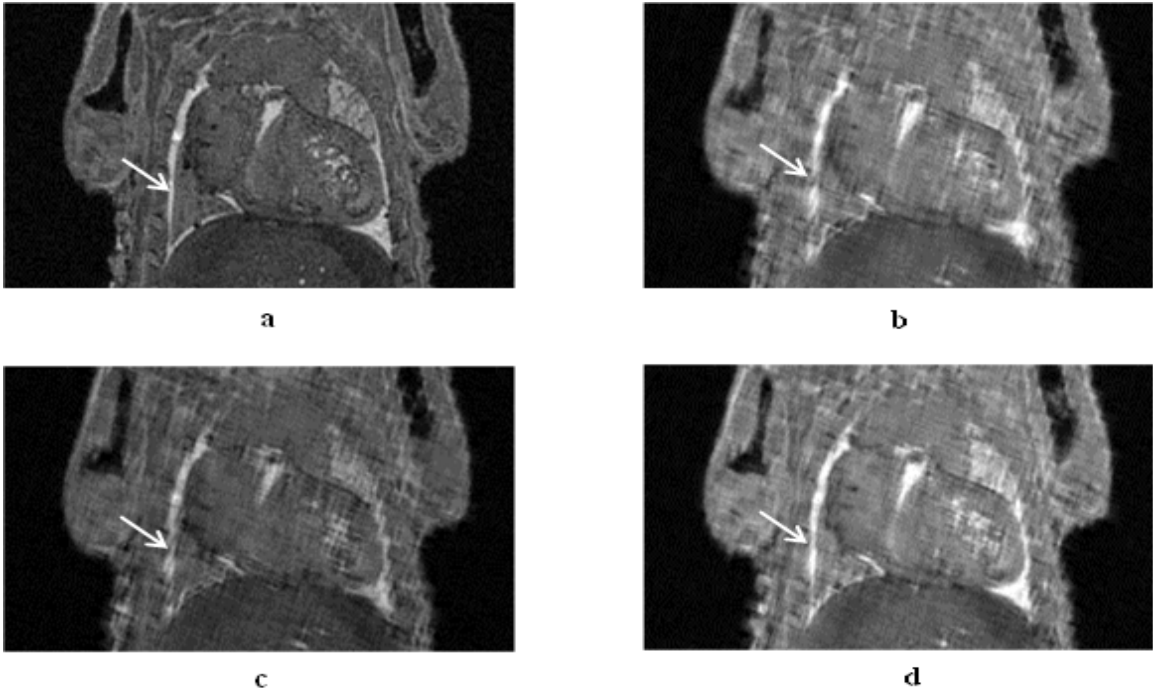


Figure 3.14: Enlarged thoracic area of *ex vivo* embryo showing developing heart, lungs and liver in: a) 3D isotropic image, b) linear SRR, c) cubic SRR, d) sigmoidal SRR (pleural cavity which is filled with contrast and fixative is highlighted with arrow)

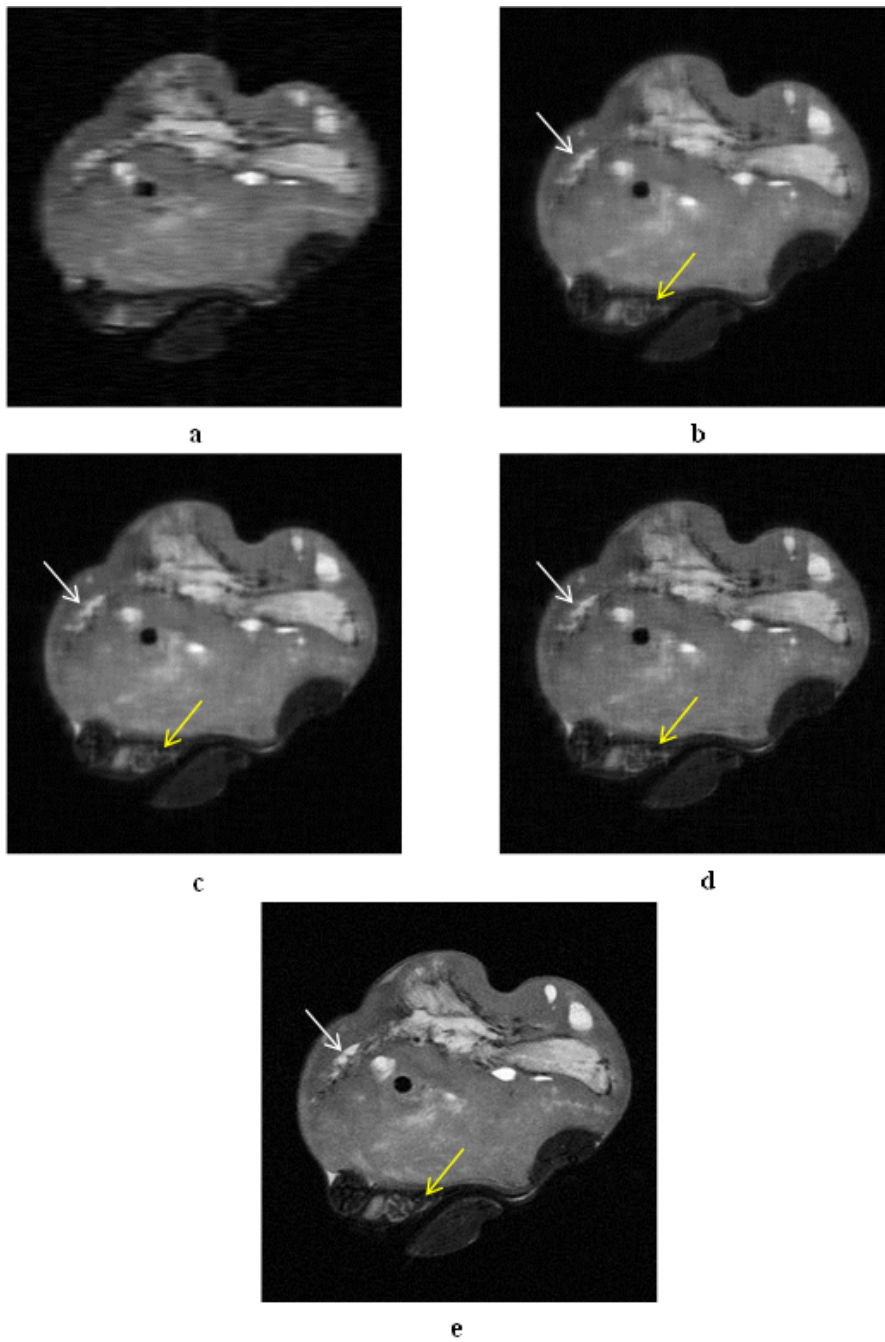


Figure 3.15: Flank area of *in vivo* mouse showing tumor in: a) interpolated, b) linear SRR, c) cubic SRR, d) sigmoidal SRR, e) HR in-plane (white and yellow arrows highlight the fat filled cavity in tumor and tail muscle). AR of LR image stacks used is 1:1:10

AR	Int <sup>a</sup>	3-view ortho	4-view ortho	5-view ortho	6-view ortho	7-view ortho	3D <sup>b</sup>
SNR							
1:1:8	27.4	32.9	34.6	35.6	37.1	39.7	45.1
1:1:10	24.1	30.5	31.8	33.9	36.3	39.8	45.1
CNR							
1:1:8	6.1	9.3	9.7	9.9	10.1	10.0	12.4
1:1:10	5.8	8.9	9.2	9.3	9.5	9.5	12.4
Mean edge width (in HR pixels)							
1:1:8	1.6	0.7	0.6	0.6	0.6	0.5	0.4
1:1:10	1.9	0.8	0.6	0.5	0.5	0.5	0.4
Contrast metric (with respect to 3D HR image)							
1:1:8	-26%	-16%	-16%	-14%	-13%	-13%	100%
1:1:10	-31%	-18%	-17%	-17%	-15%	-14%	100%

a – linear interpolated from LR image stack

b – simulated 3D SLP

Table 3.2: Quantitative parameters for the SLP with added oblique views at 30° increment

AR	Int <sup>a</sup>	3-view ortho	4-view ortho	5-view ortho	3D <sup>b</sup>
SNR					
1:1:8	24.7	36.5	38.7	39.9	26.8
1:1:10	28.1	42.2	42.9	44.1	26.8
CNR					
1:1:8	6.4	8.2	8.8	8.7	5.6
1:1:10	6.9	8.1	8.9	8.9	5.6
Mean edge width (in HR pixels)					
1:1:8	6.5	4.7	4.1	4.1	2.4
1:1:10	6.8	4.9	4.6	4.5	2.4

a – linear interpolated from LR image stack

b – isotropically acquired 3D image

Table 3.3: Quantitative parameters for biological phantom when oblique LR views are added

Parameter	Int <sup>a</sup>	3-view ortho	4-view ortho	5-view ortho	In-plane HR
SNR	16.2	24.6	27.2	29.5	18.4
CNR	1.9	2.6	2.8	2.7	3.5
Mean edge width (in HR pixels)	8.2	6.5	6.4	6.4	2.4
Acquisition time (in mins)	7.5	22.5	30.0	37.5	7.5

a – linear interpolation from LR image stack

Table 3.4: Quantitative parameters for *in vivo* experiment when oblique LR views are added

Parameter	Linear SRR	Cubic SRR	Sigmoid SRR	HR image
Mean edge width (in HR pixels)	2.7	2.5	2.3	2.1

Table 3.5: Mean edge width of wedge phantom for gradient guided sigmoid based interpolation

Parameter	Linear SRR	Cubic SRR	Sigmoid SRR	HR image
Mean edge width (in HR pixels)	3.1	2.8	2.7	2.5

Table 3.6: Mean edge width of concentric sphere phantom for gradient guided sigmoid interpolation

Parameter	Linear SRR	Cubic SRR	Sigmoid SRR	HR image
SNR	32.3	34.4	35.7	45.1
CNR	7.4	7.9	8.4	12.4
Contrast metric (with respect to HR image)	-19%	-17%	-14%	100%
Mean edge width (in HR pixels)	3.2	3.2	3.1	2.7

Table 3.7: Quantitative parameters for gradient guided sigmoid interpolation in SLP

Parameter	Linear SRR	Cubic SRR	Sigmoid SRR	HR image
SNR	26.1	28.3	29.8	36.5
CNR	6.0	6.1	6.5	7.2
Mean edge width (in HR pixels)	3.5	3.5	3.3	2.3

Table 3.8: Quantitative parameters for gradient guided sigmoid interpolation in biological phantom

Parameter	Linear SRR	Cubic SRR	Sigmoid SRR	HR image
SNR	32.4	32.9	35.1	28.2
CNR	4.6	4.6	4.9	5.8
Mean edge width (in HR pixels)	6.6	6.7	6.2	3.3

Table 3.9: Quantitative parameters for gradient guided sigmoid interpolation in *in vivo* experiment

## Chapter 4: Motion Correction Using Orthogonal Images

### 4.1 Introduction

Modulation of  $k$ -space data caused by cardiac, respiratory, peristaltic motion, subject movement, or flow produces severe ghosting artifacts in MRI. The ghosting artifacts caused by these various types of motion poses a big challenge in small animal imaging. The breath-hold technique which is primarily used to decrease respiratory artifacts in human clinical studies [64] cannot be applied to small animal studies. Even though the animal is under anesthesia, motion cannot be eliminated completely [2]. Especially when the scans have long acquisition times, the images are more susceptible to ghosting artifacts due to motion.

The modulation in  $k$ -space data which causes the motion artifacts in MRI occurs only in one direction (i.e., the phase encode direction). By acquiring multiple datasets with different phase encode directions image information is correlated between the data sets but the modulation caused by motion is uncorrelated. Previous works have exploited this property to reduce ghosting artifacts [35], [70]. The advantages of these methods are that no a priori knowledge about the type of motion is required for their implementation. They are post processing techniques and no changes in pulse sequence or hardware are needed for their implementation. These methods require

increased acquisition time, but have shown to improve the SNR and the quality of the image.

The above studies have shown that combining two MRI images acquired over the same FOV with their readout and phase encode directions interchanged can reduce motion artifacts and improve the SNR of the resultant image [35]. However, these studies used the same slice-select directions. The concept of using two MRI images acquired over the same region of interest using different slice-select directions (i.e., orthogonal views) has not been explored. In most small animal imaging studies both long axis (coronal or sagittal) and short axis (axial) images of the region of interest are obtained. In 2D MRI pulse sequences, the slice select gradients are followed by spatial encoding.

Figure 4.1 shows the encodings in different direction for both axial and coronal acquisitions. The axial view has phase encoding, readout, and slice selection along the y- x- and z-axis, respectively. The coronal view has phase, readout and slice encoding along x-, z- and y-axis respectively. For these two views the phase encoding direction is not the same, but the phase and readout encode directions are not reversed as in [35], instead, there is a three-way permutation of the MRI coding directions for this set. Phase encoding direction in the axial acquisition becomes slice-select direction in the coronal acquisition; slice-select direction in the axial acquisition becomes readout encoding in the coronal acquisition; and readout direction in the axial acquisition becomes phase encoding direction in the coronal acquisition. Note that these two sets of images would have motion artifacts in different (phase encoding) directions, and have different in-plane FOVs and slice-select directions.

Figure 4.2 shows coronal and axial images of the thoracic cavity of a mouse obtained for a rib tumor study. In this study the same region of interest is covered in two different acquisition geometries. The coronal and axial views are acquired orthogonal to each other. Typically more than one view is obtained in the small animal imaging studies and sometimes it includes orthogonal views that meet the condition for studying the geometry shown in Figure 4.1. It can be useful to study whether combining these orthogonal images will help in reducing the motion artifacts. Therefore, the goal of this study is to explore whether combining two orthogonal views obtained with different slice-select directions could improve the quality of the image by reducing artifacts due to motion.

To achieve this goal we investigate the effects of combining two orthogonal images in the motion simulated Shepp-Logan phantom (SLP) and *ex vivo* biological phantom and study the effects of the algorithm in the presence of various types of motion. For this study qualitative and quantitative assessments were performed to study the effects of motion artifact. The algorithm is implemented in two *in vivo* studies and the resultant effect in image quality is studied.

## 4.2 Materials and Methods

### 4.2.1 Algorithm

The flowchart for the implementation of the algorithm is shown in the Figure 4.3. Consider axial image stack  $I_a(X, Y, z)$  and coronal image stack  $I_c(x, Y, Z)$  acquired orthogonally to each other. To correct for motion in the axial view, the coronal view is upsampled along the x-axis and the axial view is upsampled along the z-axis. Linear interpolation is used for upsampling the image stacks. It was chosen because

it is conventionally used for projecting the data on to uniform grid and has been used widely for interpolating MR images [37].  $\hat{I}_a(X, Y, Z)$  and  $\hat{I}_c(X, Y, Z)$  represents the upsampled axial and coronal image stacks respectively. The complex conjugate product is obtained using the two upsampled views. The square root of the magnitude of the complex conjugate can then be downsampled in either direction to obtain a motion corrected image as shown in equation 4.1, 4.2 and 4.3.

$$\{P(i, Y, Z)\}_{i=1}^X = \left\{ \hat{I}_c(Y, Z) \cdot \hat{I}_a^*(Y, Z) \right\}_{i=1}^X \quad (4.1)$$

$$I_{CORR}(X, Y, Z) = \sqrt{|P(X, Y, Z)|} \quad (4.2)$$

$$I_{corr}(x, Y, Z) = \text{downsample} \{I_{CORR}(X, Y, Z)\}^{\text{along } X \text{ direction}} \quad (4.3)$$

The effective resolution achieved in the corrected image is lower than the original image. This resolution compromise is due to the combination of the in-plane view from an image stack with the through-plane view of the orthogonal image stack.

### 4.2.2 Motion Experiments

The proposed technique was evaluated by simulating motion artifact in both a Shepp-Logan phantom and in a set of *ex vivo* embryo images. Finally the technique was applied in two *in vivo* experiments (with and without cardiac and respiratory gating) in mice. Both qualitative and quantitative assessments were to done to evaluate the algorithm.

#### 4.2.2.1 Simulated motion in Shepp-Logan phantom

Images of a 3D standard Shepp-Logan phantom (256\*256\*256) were created using MATLAB program [33]. Following the procedure outlined in 3.2.2.1, this standard Shepp-Logan phantom image is downsampled in the corresponding slice-select directions to simulate the axial and coronal views with AR 1:1:5. Typically *in vivo* images in small animal MRI applications have an aspect ratio between 1:5 and 1:10. Choosing a lower aspect ratio enables the algorithm to be tested with less impact from interpolation related reconstruction errors. Different types of motion are simulated in the Shepp-Logan phantom images and the effects of the motion correction algorithm are explored. Finally the performance of algorithm is tested in the presence of added Gaussian noise and the effects of the aspect ratio (AR) on the motion correction are also explored.

- Random motion: Random motion is simulated in the coronal image stack using the procedure outlined in [43] and [21]. Any particular line/part of the  $k$ -space data, when shifted along the phase-encode direction, results in ghosting artifacts in the image. This test was designed to assess the performance of algorithm in imaging situations when an artifact occurs due to sudden subject motion or peristaltic motion. The  $k$ -space data is simulated. The farther from the center the shifting occurs in the  $k$ -space, the lesser pronounced the ghosting effect occurs in the image space. Since the contrast is determined by center of the  $k$ -space, shifting occurring farther from the center doesn't affect the contrast.

- Periodic motion: Motion was simulated in the phase encode direction in both orthogonal images using the method outlined in [43]. Periodic motion is simulated by shifting multiple lines of  $k$ -space in regular intervals which results in ghosting artifacts in the simulated image. A higher degree of motion was simulated in the coronal image stack than the axial image stacks to mimic *in vivo* conditions. Usually the effects of motion corruption are more visible in the coronal or sagittal views than the axial in the imaging. This is because the motion is propagated along the axis of body and the FOV of coronal views spans more area.
- Bulk Motion: This experiment is designed to evaluate the performance of the algorithm when motion causes bulk misalignment in one of the images. Any bulk movement of the subject being imaged is manifested as in plane rotation with a translation component. The bulk motion is simulated in the images by following the procedure outlined by Bones et al [4]. An arbitrary sequence of small rotation of angle  $\theta$  (here,  $\theta = 4^\circ, 8^\circ$ ) is applied in sampling of  $k$ -space data which results in ghosting artifacts in the image space.
- Gaussian noise: Gaussian noise was added to the real and imaginary components of an image in  $k$ -space and then reconstructed as described in [69]. Gaussian noise with  $\sigma = 0.001$  and  $\sigma = 0.005$  is introduced to test the effectiveness of the algorithm.
- Effect of AR: Since there is a resolution compromise, it is necessary to test the behavior of the algorithm with different ARs. This experiment compares the performance of motion correction algorithm with voxel ARs of 1:1:5 and 1:1:10.

#### 4.2.2.2 Simulated motion in biological phantom

Using a biological phantom to simulate motion and study the performance of algorithm in the environment very similar to *in vivo* is very helpful in analyzing its effectiveness and performance. The advantage of using biological phantom is discussed in 2.2.3. An *ex vivo* E17.5 wild type (WT) embryo was used as a biological phantom and the imaging protocol is discussed in detail in 2.2.3. There are many models used in the literature to simulate motion similar to the one observed in *in vivo* cases. Artificial motion as observed in *in vivo* case is simulated along the phase encode direction in both the images using one of these models as described in [21]. The bulk misalignment is simulated in these images by rotating the coronal image by  $3^\circ$ .

#### 4.2.3 Real Motion in *In vivo* Experiment

MR imaging of a live mouse was performed using a Bruker Biospin Avance<sup>TM</sup> 400 MHz 9.4T magnet (Bruker Biospin, Karlsruhe, Germany). All animal protocols were approved by the Institutional Laboratory Care and Use Committee of The Ohio State University. The mouse was prepared for imaging as described in 2.2.4 and placed prone on a temperature controlled mouse bed and inserted into the 35 mm diameter quadrature volume coil.

##### 4.2.3.1 *In vivo* gated experiment

For quantification of fat volume, coronal and axial image stacks of the abdominal region were acquired using RARE T1 weighted sequence (TR = 1200 ms, TE = 7.5 ms, FA = 180.0, FOV = 3\*3 cm, matrix = 256\*256, slice thickness = 0.75 mm, acquisition time = 12 min). The scans are respiratory triggered using Small Animal Monitoring System.

### 4.2.3.2 *In vivo* non-gated experiment

Coronal and axial MR images of the live mouse were acquired using a T1-weighted FLASH imaging sequence (TR = 200 ms, TE = 2.72 ms, FA = 55.0, FOV = 2.5\*2.5 cm, navgs = 8, matrix = 256\*256, 1 mm slice thickness, acquisition time = 7 min). Contiguous slices covering 25 mm of the thoracic and upper abdominal region were acquired. The images were acquired without gated triggering.

## 4.2.4 Quantitative Measures

SNR and CNR were calculated using 20\*20 pixel window within homogenous regions shown in Figure 3.1. The mean edge width was calculated from 8 edge profiles (shown in Figure 3.1) obtained across the boundary of ellipsoid. SNR, CNR and mean edge width were discussed in detail in 2.2.3.1 and 2.2.2.1.

## 4.2.5 Motion Artifact Metric

### 4.2.5.1 Contrast metric

Contrast is defined as difference between the mean maximum ( $S_{max}$  from 20\*20\*20 window in outside ellipsoid) and mean minimum ( $S_{min}$  from 20\*20\*20 window in small inner ellipsoid) signal intensities. The window used for the signal intensity calculation is shown in Figure 3.1. More on the contrast metric can be found in section 2.2.2.1

### 4.2.5.2 Mean square error (MSE) and root mean square deviation (RMS)

MSE is used for quantifying the difference between reference and test images. In the case of SLP, the simulated phantom image without motion is used as reference image. The MSE for two images is given by the equation

$$MSE = \frac{1}{XY} \sum_{i=1}^X \sum_{j=1}^Y \{R(i, j) - T(i, j)\}^2 \quad (4.4)$$

Where  $R(i, j)$  denotes the reference image and  $T(i, j)$  is test image, and  $X * Y$  is the dimension of the image.

RMS is defined as square root of MSE, given by this following equation

$$RMS = \sqrt{\frac{1}{XY} \sum_{i=1}^X \sum_{j=1}^Y \{R(i, j) - T(i, j)\}^2} = \sqrt{MSE} \quad (4.5)$$

The major disadvantage of MSE and RMS is that they are not invariant to the translation and rotation of the images. If there is significant distortion because of the motion, as in the *in vivo* case, it has to be combined with image registration step to get a meaningful value. It has been observed that misregistration or errors in registration step can result in significant difference in MSE values [43]. Because of this we have used this metric only for SLP phantom experiment. Irrespective of the disadvantages, because of the wide usage of MSE and RMS, they are included in this study for phantom experiment.

#### 4.2.6 Tests Using Automated Image Segmentation Algorithms

The ability to automatically extract exact contours of organs, tumors, or region of interest is of vital importance in the field of medical image analysis. The presence of moderate to severe motion artifact in the ROI can make even the manual tracing of a structure difficult [46]. Accurate tracing of a structure influences quantitative measurements like area and volume. The sharpness and the gradient intensity of the edges are some of the features which influence the optimal segmentation. The motion corruption artifacts often result in ghosting images with varying amplitude

being superimposed on the structures within the ROI and hence reduction in the edge sharpness. Ghosting artifact affects the accuracy of the edge detection and therefore significantly hampers the performance of automated segmentation algorithms. The reduction of ghosting artifacts in an image should result in an improved performance with automated segmentation methods.

Comparing the performance of the segmentation algorithms in the images before and after the application of motion correction helps in assessing the clinical applicability of the algorithm. We compare the organs traced by segmentation algorithms in both the motion-corrupted and motion-corrected images against segmentation traced by an expert observer used as a golden standard [3], [9], [66], [68]. There are various methods to compare outlines obtained from segmentation algorithms [6], [71]. We have designed three experiments to compare the performance of automatic segmentation algorithm on motion-corrected images. The segmentation algorithm was chosen based on the applicability for the specific application.

Organ or body volume was calculated from the automated segmentation and manually-traced outlines. The following statistical metrics were calculated to evaluate the performance of the automated segmentation algorithms used for calculating volume when applied to the motion-corrected images as compared to that of the gold standard method. The following statistical metrics were used for the comparison.

#### **4.2.6.1 Otsu's segmentation of brain in biological phantom**

For the first test, we used multi-level Otsu's segmentation algorithm to segment brain in *ex vivo* wild type embryo [50], [25]. The segmentation algorithm is applied to the images with simulated motion and it is compared with the motion corrected images and ground truth (no motion). Matlab was used for the Otsu segmentation

and brain volume was calculated from the segmented images. The statistical metrics described below in 4.2.7 were used to evaluate the segmentation algorithm. A comparison of segmented regions was also done by subtracting the motion simulated image from the original image and performing a pixel-by-pixel comparison of the boundary. Three different threshold levels are used for this implementation of multi-level Otsu algorithm.

#### **4.2.6.2 Active contour body segmentation in *in vivo* mouse model**

For the second test we used geodesic active contours to segment the outer body contours from *in vivo* images of a mouse model of obesity [32], [27]. Active contours segmentation from MIPAV [45] was used for segmenting the body in coronal images of a live mouse and body volume was calculated from the segmentation. The parameters used in this implementation of geodesic active contour models are step size = 0.05-0.75 with  $\delta = 0.005$ , and cut off error threshold  $\theta = 5 * 10^{-4}$ . Expert observer's tracings of the outer body in the *in vivo* images were compared with the segmented results from active contours before and after application of motion correction algorithm.

#### **4.2.6.3 Active contour kidney segmentation in *in vivo* mouse model**

For the third application we used the propagation active contour model to segment kidney from the coronal *in vivo* images of abdomen [32]. The propagation of contours in active contour is represented as a form of optimization problem [58]. This is a semi-automatic method in which the initial contour selected manually is propagated to all images in the stack using parametrical representation of contours and image properties [49]. The parameters used to implement this algorithm are as follows, step size = 0.2-0.5 with  $\delta = 0.01$ , the gradient increase  $\lambda = 0.05$  with the cut off error

threshold,  $\theta = 2 * 10^{-3}$ . The parameter which is measured in this application is the volume of kidneys. Estimation of the kidney volume is important in the study of chronic kidney diseases [76]. The expert observers' tracing of kidneys from before and after the application of the motion correction algorithm are compared with the results obtained from the segmentation using active contours in both the cases. Type I, type II error, RE, BCE, and FVE of kidneys are tabulated for comparison.

## **4.2.7 Statistical Metrics Used for Evaluation of Tests Using Automated Image Segmentation Algorithms**

### **4.2.7.1 Type I and Type II error**

Type I error denotes the number of pixels incorrectly classified as objects when in fact they are not. This can be referred to as false positive or over-segmentation. Type II error denotes the number of pixels incorrectly not classified as object when in fact they belong in the category. Both these errors are represented as percentages of ground truth segmentation.

### **4.2.7.2 Positive and negative predictive values**

Positive predictive values (PPV) are the proportion of the true positives among the positive results obtained from the diagnostic tests. False discovery rate (FDR) is the ratio of false positives among all the positive calls. FDR is complementary to PPV. Negative predictive values (NPV) are the proportion of the true negatives among the negative results obtained from the diagnostic tests. False omission rate (FOR) is the ratio of false negatives among all the negative results. FOR is complementary of NPV. Both FDR and FOR are closely related with type I and type II errors respectively.

$$PPV = \frac{\text{Number of true positives}}{\text{Number of positive calls}} \quad (4.6)$$

$$FDR = \frac{\text{Number of false positives}}{\text{Number of positive calls}} = 1 - PPV \quad (4.7)$$

Where *No. of positive calls* = *No. of true positives* + *No. of false positives*

$$NPV = \frac{\text{Number of true negatives}}{\text{Number of negative calls}} \quad (4.8)$$

$$FOR = \frac{\text{Number of false negatives}}{\text{Number of negative calls}} = 1 - NPV \quad (4.9)$$

Where *No. of negative calls* = *No. of true negatives* + *No. of false negatives*

#### 4.2.7.3 Rand index and rand error

Rand index (RI) is based on nonparametric test in statistics literature which measures the similarity between two data clustering methods [55]. The segmentation algorithms can be considered as clustering of pixels. Each segmented area is a cluster of pixels which shares the same label. Rand index is used as a metric to measure the performance of a segmentation algorithm [65]. The Rand index can be computed by using the formula

$$RI = \frac{(a + b)}{\binom{n}{2}} \quad (4.10)$$

Where, given two segments  $S_1$  and  $S_2$  obtained from the image  $I$  by observer's manual tracing and by using auto/semi-auto segmentation algorithm, then  $a$  denotes the pair of pixels in  $I$  which are classified as same object (in other words, belongs

to same clusters sharing same labels) in both  $S_1$  and  $S_2$ .  $b$  denotes the pair of pixels in  $I$  which are classified as different object (in other words, belongs to different clusters with different labels) in both  $S_1$  and  $S_2$ .  $(a + b)$  denotes the number of agreements between  $S_1$  and  $S_2$ .  $\binom{n}{2}$  gives the summation of number of agreements and disagreements between  $S_1$  and  $S_2$ .  $n$  refers to number of pixels enclosed in the area of interest chosen to exclude background noise in image  $I$ . This area of interest is specific to each application. Rand error (RE) gives the measure of disagreement between the methods, it can be calculated using the formula,

$$RE = 1 - RI \quad (4.11)$$

#### 4.2.7.4 Fractional volume error

Fractional volume error (FVE) measures the difference in the volume calculated using the manual segmentation and automated segmentation.

$$FVE = \frac{abs(V_M - V_A)}{V_M} \quad (4.12)$$

$V_M$  indicates the volume of the ROI obtained from the manual segmentation.  $V_A$  indicates the volume of the ROI obtained from using the automatic segmentation algorithm.

## 4.3 Results

### 4.3.1 Simulated Motion in Shepp-Logan Phantom

#### 4.3.1.1 Qualitative evaluation

- Random motion: Figure 4.4 shows the result for the motion correction when simulated random motion is introduced to a noiseless Shepp-Logan phantom

image. The ghosting artifact caused by the simulated motion is highlighted in the Figure 4.4a. It is evident that the motion is reduced in the coronal view with the help of the axial view which is not corrupted. The cross-correlated image does a better job at reducing the motion than the simple averaging operation.

- Periodic motion: Figure 4.5b shows the simulated motion in the phase encode direction which is similar to *in vivo* environment in the axial image stack. There is a visible improvement in the motion corrected image after the algorithm is applied as shown in Figure 4.5c. The point to be noted is that in the axial image before the algorithm is applied the ghosting artifacts are spread across only one axis, but the resultant image stack has ghosting artifact along both the axes which is visibly of lower magnitude than the one in the original image.
- Bulk motion: Figure 4.6 shows the performance of the algorithm in the presence of bulk misalignment used to simulate the case of sudden change in subject position. It is shown that when bulk motion is caused by rotation of  $4^\circ$ , the correction algorithm still removes a substantial amount of artifacts and potential misalignment in the resultant image is not evident, but when the rotation is increased to  $8^\circ$ , the misalignment between the structures when combining both the images is evident.
- Gaussian noise: Figure 4.7 shows the performance of the algorithm in the in the presence of Gaussian noise. The coronal and axial image stacks corrupted with Gaussian noise with  $\sigma = 0.001$  and  $\sigma = 0.005$  are shown in Figure 4.7a, 4.7b and Figure 4.7d, 4.7e, respectively. The correction algorithm works even in the

presence of noise, but as Figure 4.7c and Figure 4.7f show the performance of the algorithm deteriorates when the noise increases.

- Effect of AR: The result of the correction algorithm in the image stacks with different ARs (1:1:5 and 1:1:10) are shown in Figure 4.8. Visual inspection of the Figure 4.8 shows that the motion correction is more effective in case of voxel AR = 1:1:5 (Figure 4.8c). When the voxel AR is increased, we notice more ghosting artifacts (Figure 4.8f).

#### 4.3.1.2 Quantitative evaluation

- Random motion: RMS, MSE, mean edge width, contrast metric (with respect to reference image), SNR and CNR for SLP random motion experiment are listed in Table 4.1 for both motion corrupted image stack and complex conjugate motion corrected image stack . The SLP image before the motion simulation is used as the reference image for the contrast metric comparison. SNR and CNR increased with the application of algorithm. The contrast metric and mean edge width is improved by 12% and 40%, respectively, after the motion correction algorithm is applied. As expected MSE and RMS are decreased in the motion corrected image stack.
- Periodic motion: Table 4.2 shows the quantitative parameters for the periodic motion experiment in SLP. As seen from the Table 4.2, the quantitative parameters improved as a result of the motion correction algorithm.
- Bulk motion: The quantitative parameters for the 4° and 8° bulk motion rotation are listed in Table 4.3. In case of 4° bulk motion, correction algorithm

improved the contrast metric and mean edge width by 13% and 25%, respectively. When the bulk motion is increased to  $8^\circ$ , the motion correction algorithm improved the contrast metric and mean edge width by 9% and 11% only. The improvements shown by the correction algorithm is reduced when the bulk motion is doubled.

- Gaussian noise: The CNR and SNR of image with motion and the motion corrected image are listed in Table 4.4. The SNR and CNR are improved in the motion corrected images by 56% and 54% respectively when Gaussian noise with  $\sigma = 0.001$  is introduced, when Gaussian noise with  $\sigma = 0.005$  is added the SNR and CNR are improved by 37% and 45% respectively. Similar pattern is observed for mean edge width, contrast metric, MSE and RMS.
- Effect of AR: The quantitative parameters for the SLP motion stimulation experiment with different ARs are listed in Table 4.5. The increase in AR reduces the performance of the algorithm.

## 4.3.2 Simulated Motion in Biological Phantom

### 4.3.2.1 Qualitative evaluation

The axial image of the *ex vivo* embryo with simulated motion and the result of the correction algorithm is showed in Figure 4.9. In Figure 4.9a motion artifact caused by the simulated motion is evident in spinal cord region of coronal image. Figure 4.9c shows the result of motion correction algorithm which has less motion artifacts when compared to Figure 4.9a.

Parameter	Simulated motion	Motion corrected
MSE	120.4	82.2
RMS	11.0	9.1
Contrast metric (with respect to ideal image)	-22%	-10%
Mean edge width	1.5	0.9
SNR	39.4	43.8
CNR	9.3	11.2

Table 4.1: Quantitative parameters for SLP random motion simulation

#### 4.3.2.2 Quantitative evaluation

The SNR, CNR and mean edge width are the quantitative parameters used for the *ex vivo* (biological phantom) motion stimulation study and they are listed in Table 4.6. Different sets of quantitative measures are chosen for evaluating different experiments according to the suitability of the parameters to the experiment. MSE and RMS are not rotational and translational invariant, because of this reason these parameters are not used for biological phantom experiment. Contrast metric is not a useful measure because the biological phantom has soft tissues which are typical of *in vivo* and *ex vivo* experiments, and contributing to the wide range of gray scale information in the images instead of having uniform (constant) gray levels within a region. Finding contrast along the line profile might not be useful, as the variation in the mean signal intensity would be high along line profile, even in an homogeneous area. Mean edge width which measures the broadening of the edges is useful in *ex*

Parameter	Simulated motion	Motion corrected
MSE	143.6	85.4
RMS	12.0	9.2
Contrast metric (with respect to ideal image)	-25%	-14%
Mean edge width	1.8	1.3
SNR	37.2	41.6
CNR	9.0	10.8

Table 4.2: Quantitative parameters for SLP periodic motion simulation

*vivo* case. The SNR, CNR and mean edge width are improved by 12%, 14% and 23% respectively when the motion correction algorithm is applied.

#### 4.3.2.3 Otsu's segmentation of brain in biological phantom

The Table 4.7 shows the comparison between *ex vivo* images with no motion and *ex vivo* images with simulated motion and *ex vivo* images with motion correction algorithm by tabulating the type I, type II errors, PPV, NPV, FVE and RE for the manual and automatic segmentation algorithm. The results tabulated in the Table 4.7 show that the introduction of motion increased the type I and type II error to 4.35% and 3.86%. After the application of motion correction algorithm, type I and type II errors have been reduced to 3.94% and 3.33% respectively. These errors are still higher than the *ex vivo* images without motion, but lower than the simulated motion images without correction. The fractional volume error which indicates the change in the volume of ROI between manual tracing and the automated segmentation algorithm is

Parameter	Simulated bulk motion $\theta = 4^\circ$	Motion corrected $\theta = 4^\circ$	Simulated bulk motion $\theta = 8^\circ$	Motion corrected $\theta = 8^\circ$
MSE	150.9	116.7	168.2	132.5
RMS	12.3	10.8	13.0	11.5
Contrast metric (with respect to ideal image)	-28%	-15%	-61%	-50%
Mean edge width	2	1.6	3.1	2.8
SNR	33.5	38.7	31.1	34.6
CNR	8.3	10.4	7.1	8.5

Table 4.3: Quantitative parameters for SLP bulk motion simulation

increased after the addition of simulated motion. The application of motion correction algorithm to the *ex vivo* image with simulated motion decreased the FVE by 23% compared to the uncorrected image set. The RE which denotes the disagreement between the manual and automatic segmentation methods has increased due to the addition of simulated motion to the *ex vivo* images. The motion correction algorithm applied to *ex vivo* images brings down the RE by 31% compared to the uncorrected data.

### 4.3.3 Gated *In vivo* Experiment

#### 4.3.3.1 Qualitative evaluation

The coronal image of *in vivo* mice abdomen with visible motion and the result of the correction algorithm are shown in Figure 4.10. The ghosting caused by motion

Parameter	Simulated motion Gaussian noise $\theta = 0.001$	Motion corrected Gaussian noise $\theta = 0.001$	Simulated motion Gaussian noise $\theta = 0.005$	Motion corrected Gaussian noise $\theta = 0.005$
MSE	183.6	151.6	219.4	189.0
RMS	13.5	12.3	14.8	13.7
Contrast metric (with respect to ideal image)	-47%	-67%	-146%	-159%
Mean edge width	3.7	3.1	4.9	4.5
SNR	26.9	28.1	15.3	18.2
CNR	4.3	4.9	2.9	3.4

Table 4.4: Quantitative parameters for SLP simulation with Gaussian noise

(highlighted in the coronal image by red arrow) is reduced by the correction algorithm. Due to the presence of motion in the coronal view, the anatomical details inside the kidneys are blurred and those details are visible in the upsampled and rotated axial image stack, and by using the correction algorithm, some of these structures are recovered (highlighted by white arrow).

#### 4.3.3.2 Quantitative evaluation

SNR, CNR and mean edge width are the quantitative parameters used in the evaluation. The correction algorithm improved the SNR, CNR and mean edge width by 44%, 27% and 11% respectively as shown in Table 4.8.

Parameter	Simulated motion AR = 1:1:5	Motion corrected AR = 1:1:5	Simulated motion AR = 1:1:10	Motion corrected AR = 1:1:10
MSE	116.5	92.4	128.2	103.6
RMS	10.8	9.6	11.3	10.2
Contrast metric (with respect to ideal image)	-20%	-13%	-21%	-17%
Mean edge width	1.6	0.8	3.9	3.1
SNR	39.7	43.5	34.5	37.2
CNR	9.3	11.4	8.1	10.8

Table 4.5: Quantitative parameters for SLP simulation experiment with different ARs

#### 4.3.3.3 Active contour body segmentation in *in vivo* mouse model

Table 4.9 shows comparison results of active contour segmentation for the *in vivo* case. The results show that with the application of motion correction algorithm, type I and type II errors are reduced to 5.98% and 7.27%. The motion correction algorithm decreased the FVE by 34% compared to the uncorrected image set, and the RE was decreased by the motion correction algorithm by 25.6%.

#### 4.3.3.4 Active contour kidney segmentation in *in vivo* mouse model

The results tabulated in the Table 4.10 show that with the application of the motion correction algorithm, type I and type II errors are reduced to 10.50% and 12.64%. The application of the motion correction algorithm decreased the FVE by

Parameter	Simulated motion	Motion corrected
Mean edge width	3.8	3.1
SNR	22.5	25.1
CNR	4.3	4.9

Table 4.6: Quantitative parameters for *ex vivo* (biological) phantom simulation experiment

6.27% compared to the uncorrected data and RE is decreased by the motion correction algorithm by 9.8%.

### 4.3.4 Non-gated *In vivo* Experiment

#### 4.3.4.1 Qualitative evaluation

An *in vivo* coronal axis image of a mouse with no gating is shown in Figure 4.11 along with the result of correction algorithm. In this case the correction algorithm doesn't improve the quality of the image substantially.

#### 4.3.4.2 Quantitative evaluation

Although visual inspection of the non-gated *in vivo* experiment doesn't show substantial improvement of the ghosting artifacts caused by motion, quantitative parameters like SNR, CNR and mean edge width are improved by 25%, 10% and 6%, respectively, as a result of the motion correction algorithm (Table 4.11).

## 4.4 Discussion

The results of this study illustrate that the motion correction algorithm based on combining orthogonal images improves the image quality. In the Shepp-Logan

Image stack	Type I error	Type II error	PPV	NPV	FVE	RE
<i>Ex vivo</i>	3.69%	0.90%	96.3%	99.10%	1.86%	2.86%
<i>Ex vivo</i> with simu- lated motion	4.35%	3.86%	95.65%	96.14%	3.37%	5.50%
<i>Ex vivo</i> with simu- lated motion and motion correc- tion algo- rithm	3.94%	3.33%	96.06%	96.67%	2.60%	3.81%

Table 4.7: Statistical metrics when multi-level Otsu is used for segmentation of brain in biological phantom images with simulated motion

phantom experiment, considerable improvement in SNR, CNR, mean edge width, MSE and contrast metric are observed in the motion corrected image. It can be also noted from the SLP experiment with addition of Gaussian noise that the performance of algorithm decreases with increase in the noise. The motion correction algorithm combines a high resolution image with interpolated low resolution image by taking complex conjugate product. As a result, theoretically there should be a resolution compromise along with the motion reduction (i.e., decrease in the in-plane resolution compared to the original image).

Parameter	Simulated motion	Motion corrected
Mean edge width	7.8	7.0
SNR	16.9	24.4
CNR	3.7	4.7

Table 4.8: Quantitative parameters for *in vivo* gated study

Image stack	Type I error	Type II error	PPV	NPV	FVE	RE
<i>In vivo</i>	6.32%	8.71%	93.68%	91.29%	2.86%	8.63%
Motion corrected <i>In vivo</i> images	5.98%	7.27%	94.02%	92.73%	1.88%	6.42%

Table 4.9: Statistical metrics when active contour body segmentation is used in *in vivo* mouse model

In image processing terms, the spatial resolution of an image is defined as the smallest discernible detail in the image, in other words, how closely lines can be resolved in an image [16]. Spatial resolution is defined as line pairs per unit distance [16], [29]. In MRI, spatial resolution is typically defined as size of imaging voxels. In-plane resolution is given by FOV divided by the in-plane matrix size [19]. Therefore, the spatial resolution in MRI image depends on its FOV, matrix size and slice-thickness (through-plane resolution). The compromise in the resolution due to the motion correction algorithm noted above refers to the resolution in classical image

Image stack	Type I error	Type II error	PPV	NPV	FVE	RE
<i>In vivo</i>	10.75%	13.06%	89.25%	86.94%	8.05%	12.60%
Motion corrected <i>In vivo</i> images	10.50%	12.64%	89.50%	87.36%	6.74%	10.10%

Table 4.10: Statistical metrics when active contour kidney segmentation is used in *in vivo* mouse model

Parameter	Simulated motion	Motion corrected
Mean edge width	10.4	9.8
SNR	13.6	17.2
CNR	2.5	3.1

Table 4.11: Quantitative parameters for *in vivo* non-gated rib tumor study

processing definition (the ability to resolve two lines as distinct). Actual spatial resolution in this sense is usually measured by calibration line pair phantom [54], [40] because of the difficulty in fabricating a line pair phantom [11], it is common to estimate the resolution by estimating reconstructed line width as a parameter for quantitative evaluation [52]. The resolution estimate is calculated by fitting sigmoid model and measuring the rise length and is defined as edge width (in HR pixels) [17], [60]. In this method, it should be noted that the mean edge width is not the actual resolution measured from the image, but rather a quantifiable estimation that provides some

insight into image resolution. In general, smaller line width represents higher image resolution.

The mean edge width measured from SLP reference image (with no added motion) is calculated as 0.4. Various types of simulated motion were observed to increase the mean edge width, because of the ghosting artifact which in turn reduced the sharpness of edges. However, when introducing the motion correction algorithm, there is a tradeoff due to the interpolation of the lower resolution from the orthogonal view which can compromise edge width when combined with the finer detail in the in-plane images. As a result, the mean width in the motion corrected never reached the 0.4 value from the in-plane images from the motion free data. The effective resolution achieved in the corrected image is lower than the original in-plane image, because of the combination of the in-plane view from an image stack with the interpolated through-plane view of the orthogonal image stack. In other words, the broadening of the mean edge width in the motion corrected image can be attributed to the interpolated through-plane image used in the algorithm. Apart from the increase in mean edge width, introduction of motion artifacts along the readout direction (which is absent in original image) is also observed, as a result of complex conjugate product obtained with orthogonal image which has motion artifact along that direction.

The performance of the algorithm is affected as the bulk misalignment increases. As long as there is no bulk misalignment the algorithm produces qualitatively better images. It is shown that when the bulk misalignment is caused by a rotation of  $4^\circ$ , the correction algorithm still removes a substantial amount of motion artifact and potential misalignment in the resultant image is not evident, but when the bulk motion is doubled to  $8^\circ$ , the misalignment between the structures when combining

the orthogonal images is evident. Increase in AR affects the quality of the motion corrected image.

Increase in AR, implies an increase in interpolation factor for the orthogonal image. As we have already discussed in chapter 2 for super resolution, increase in AR increases the mean edge width, as it broadens the edges. This increase in interpolation factor is the main reason for the reduction in the improvement of edge width and contrast metric, thereby reducing the performance of motion correction algorithm when the algorithm is applied to image stacks with high ARs.

The correction algorithm had a run time ranging from 4 min-6 min in a 2.20 GHz Alienware system. Statistical metrics used for evaluation of tests using automated image segmentation algorithms show that the type I and type II errors are both reduced by the application of motion correction algorithm. This implies that the algorithm decreased the number of instances a pixel belonging to object is classified as nonobject and vice versa. The FVE and RE were also reduced in motion corrected images. The FVE indicates the difference in the volume of a ROI, between manual tracing and the automated segmentation algorithm. It is decreased in the motion corrected image. Rand error which indicates the number of instances the manual segmentation disagrees with automatic segmentation has decreased after the application of motion correction algorithm which can be attributed to the improvement in the image quality.

The improvement in SNR and CNR are higher in the phantom experiments than the *in vivo* experiments. This is because the phantom experiments simulate an ideal case for the testing of the algorithm. The improvement in CNR and SNR are much lower in the *in vivo* images with no gating when compared with the *in vivo* images

from gated acquisition. In non-gated acquisition, all the orthogonal views are affected by severe motion artifacts due to the absence of gated triggering, so using additional orthogonal views doesn't provide any useful information to improve the image quality . The motion correction algorithm is useful when orthogonal images are already acquired, and the original image data have moderate motion artifacts similar to the case of gated acquisitions. In these cases, it is advantageous to use the available orthogonal image(s) to improve the image quality by reducing ghosting artifacts caused by motion. Future work could focus on implementing and testing the algorithm in *in vivo* experiments with sufficient number of data samples to establish the statistical significance of the result.

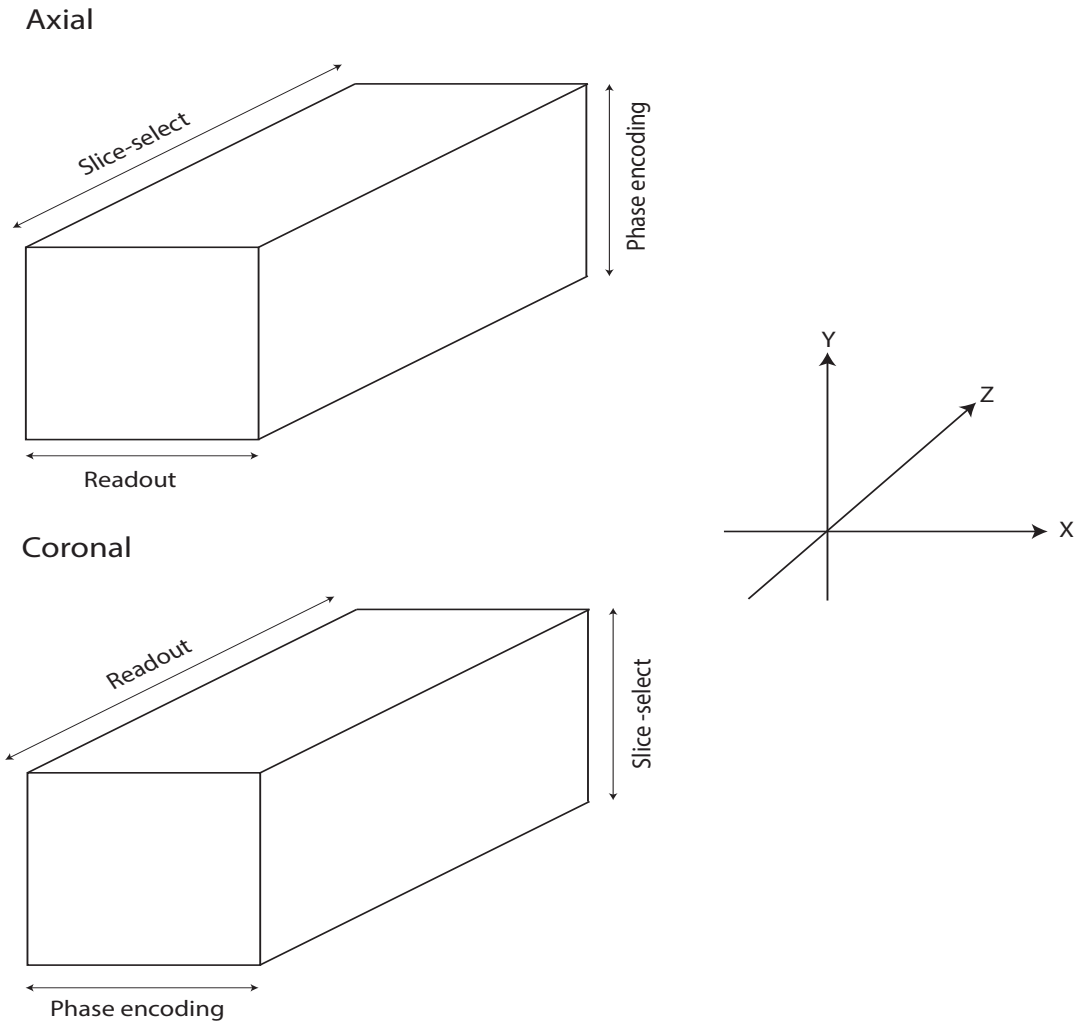


Figure 4.1: Coronal and axial acquisition geometry along with encoding directions

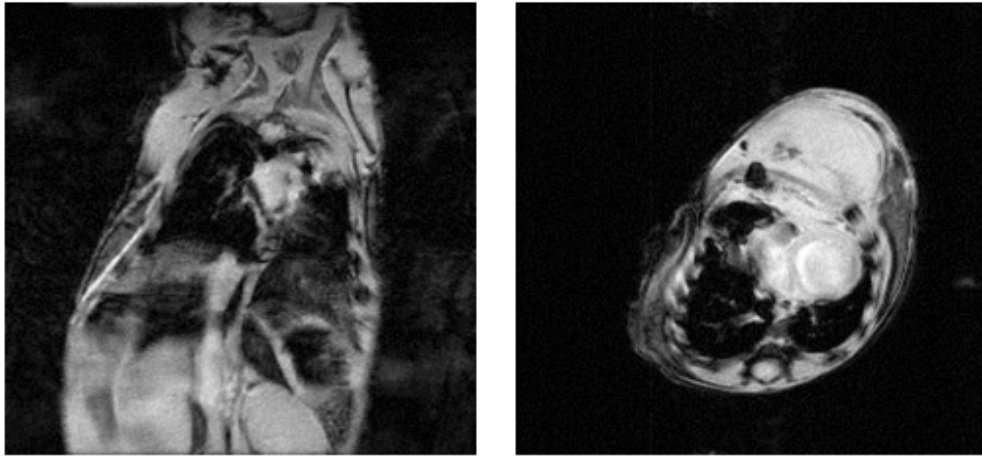
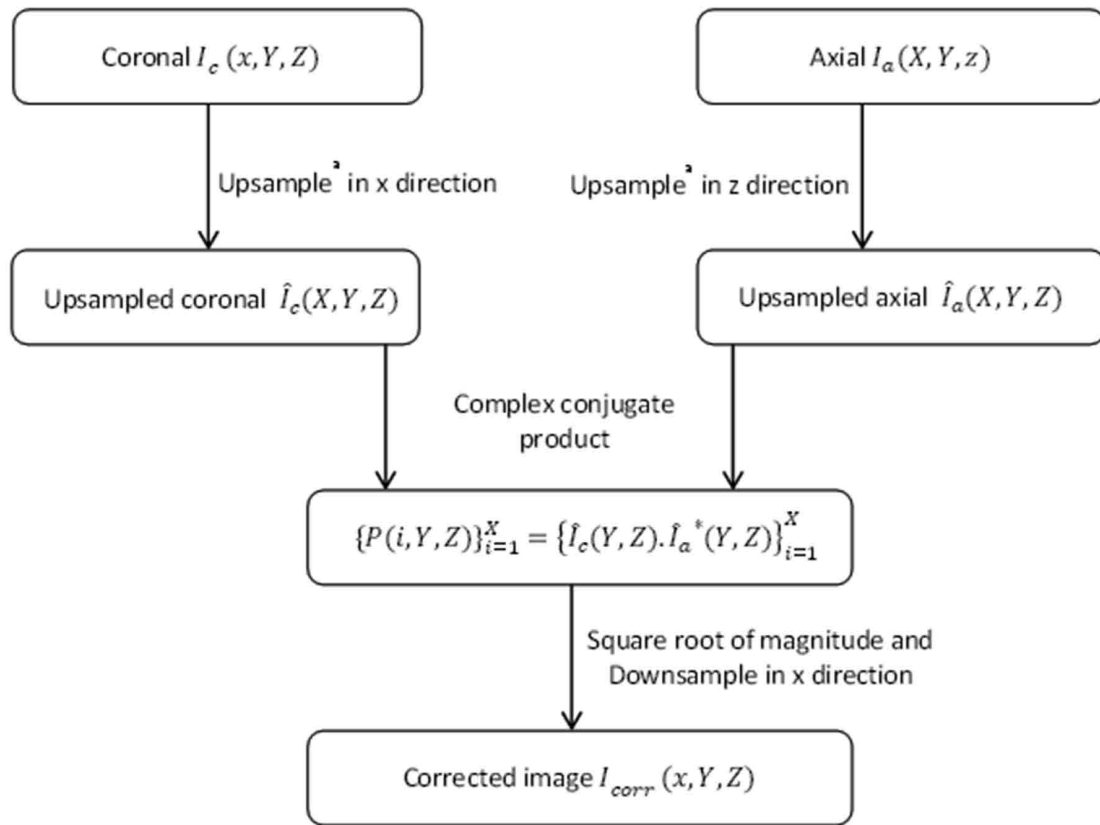


Figure 4.2: Coronal (left) and axial (right) images of thoracic cavity of *in vivo* mouse obtained for rib tumor study



a – linear interpolation

Figure 4.3: Flowchart of the motion correction algorithm

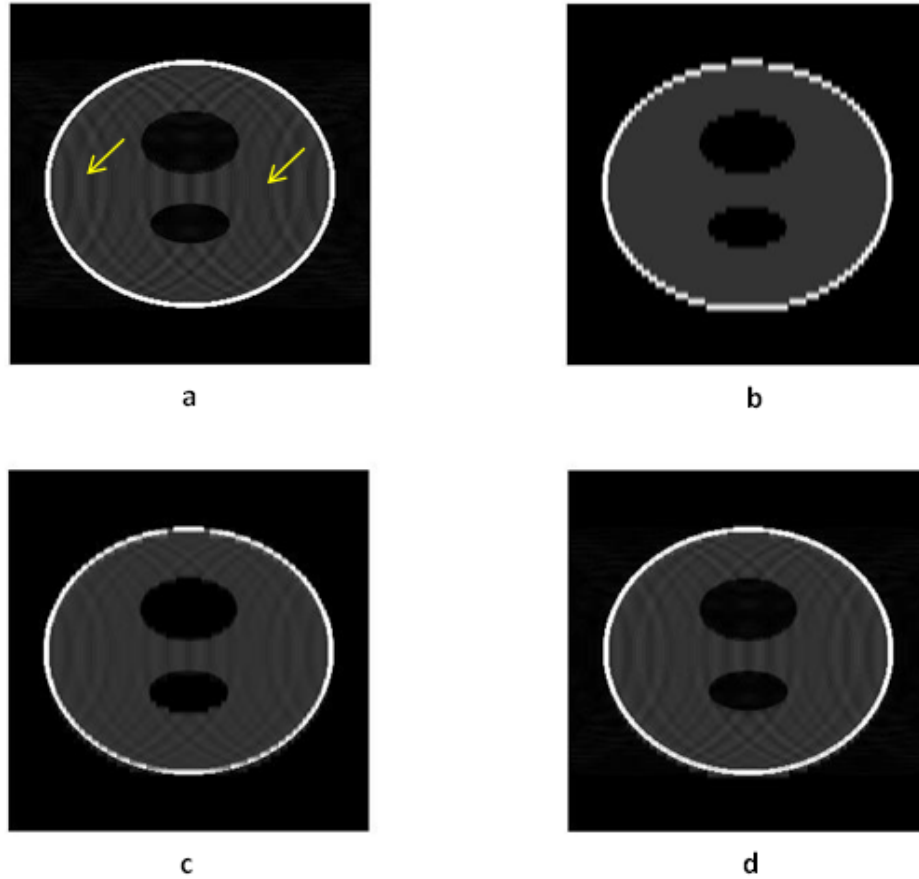


Figure 4.4: Shepp-Logan phantom a) coronal image stack corrupted with random motion, b) axial image stack with no motion rotated and viewed in coronal plane, c) motion corrected image, d) average image. The motion artifacts are highlighted by arrows

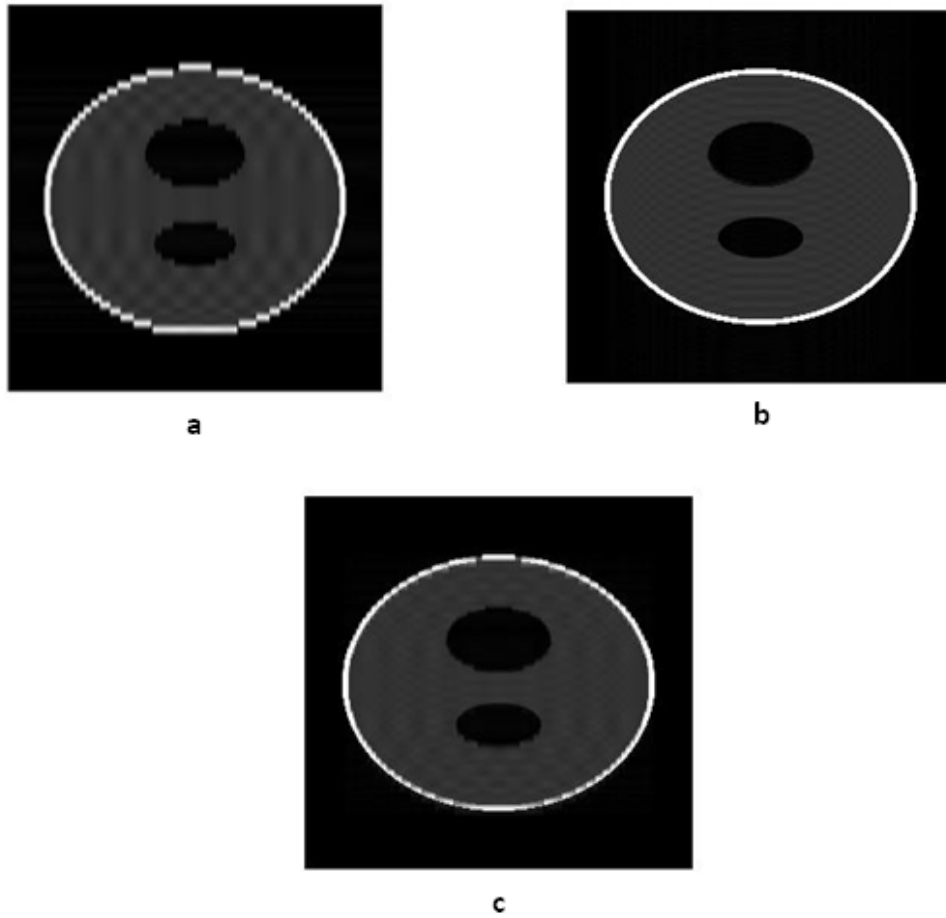


Figure 4.5: Shepp-Logan phantom a) coronal image stack corrupted with more periodic motion than axial image stack, b) axial image stack corrupted with motion, c) motion corrected image

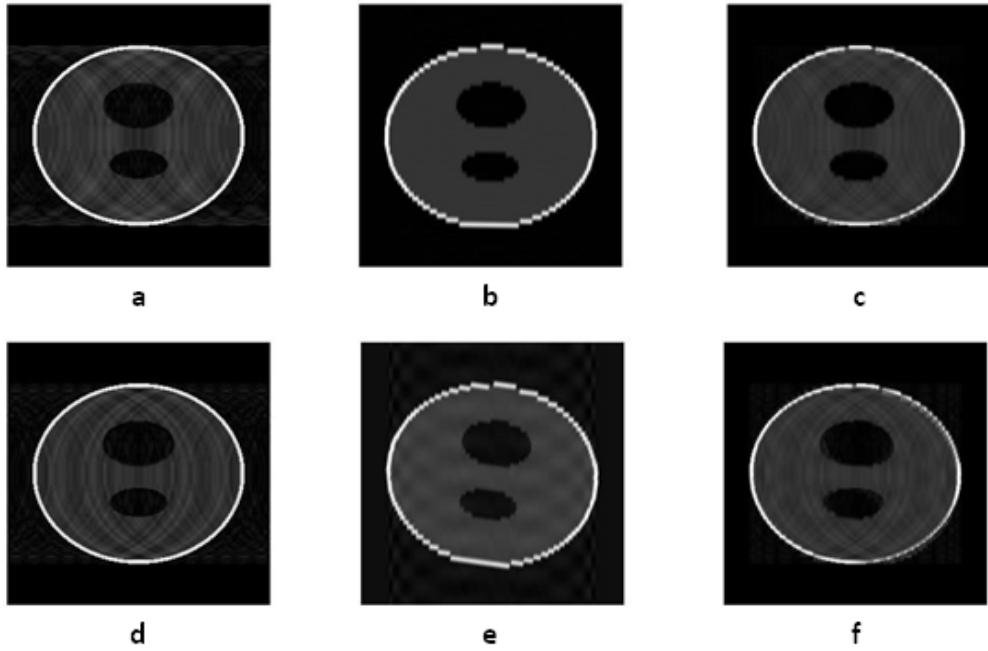


Figure 4.6: Shepp-Logan phantom with bulk motion a) motion corrupted coronal image stack, b) axial image stack with bulk misalignment rotation of  $4^\circ$ , c) motion corrected image when bulk misalignment rotation is  $4^\circ$ , d) motion corrupted coronal image stack, e) axial image stack with bulk misalignment rotation of  $8^\circ$ , f) motion corrected image when bulk misalignment rotation is  $8^\circ$

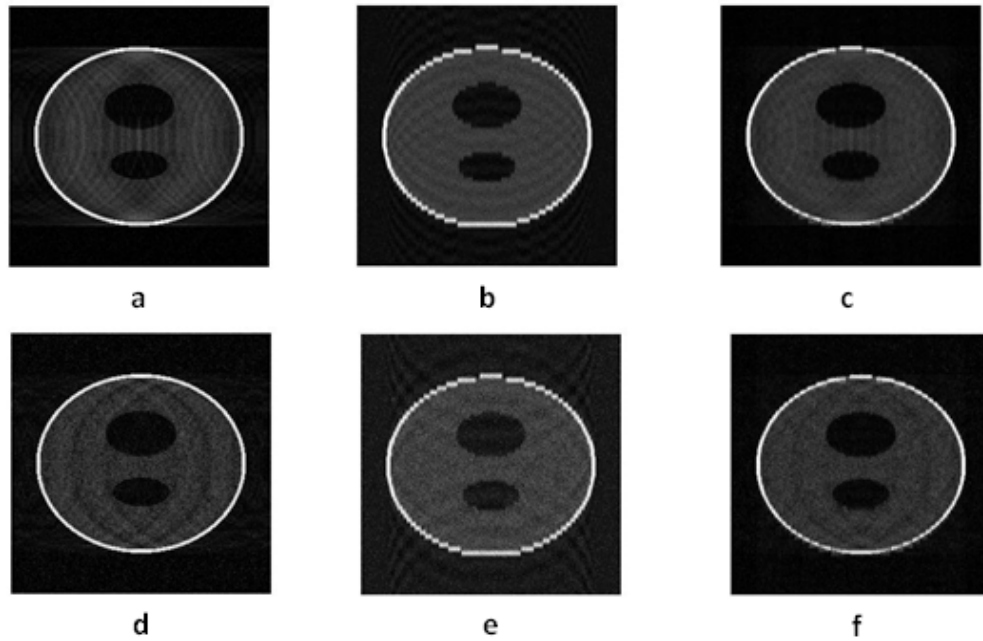


Figure 4.7: Shepp-Logan phantom with added gaussian noise a) coronal image stack with gaussian noise  $\sigma = 0.001$ , b) axial image stack with gaussian noise  $\sigma = 0.001$ , c) motion corrected image in case of gaussian noise with  $\sigma = 0.001$ , d) coronal image stack with gaussian noise  $\sigma = 0.005$ , e) axial image stack with gaussian noise  $\sigma = 0.005$ , f) motion corrected image in case of gaussian noise with  $\sigma = 0.005$

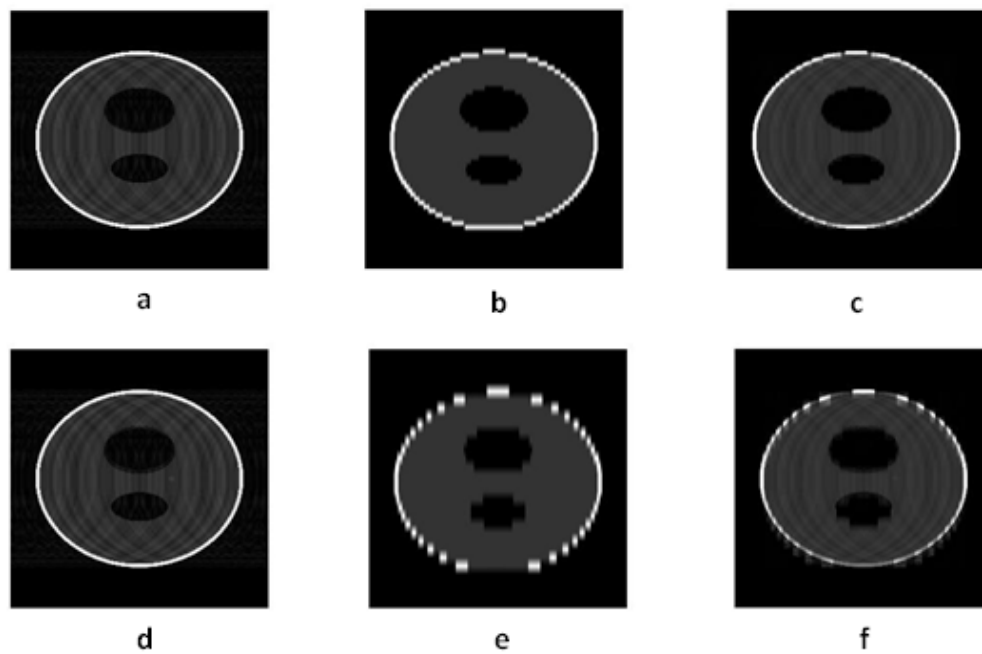


Figure 4.8: Shepp-Logan phantom with different ARs a) motion corrupted coronal stack, b) axial stack with AR 1:1:5, c) motion corrected image when AR is 1:1:5, d) motion corrupted coronal stack, e) axial stack with AR 1:1:10, f) motion corrected image when AR is 1:1:10

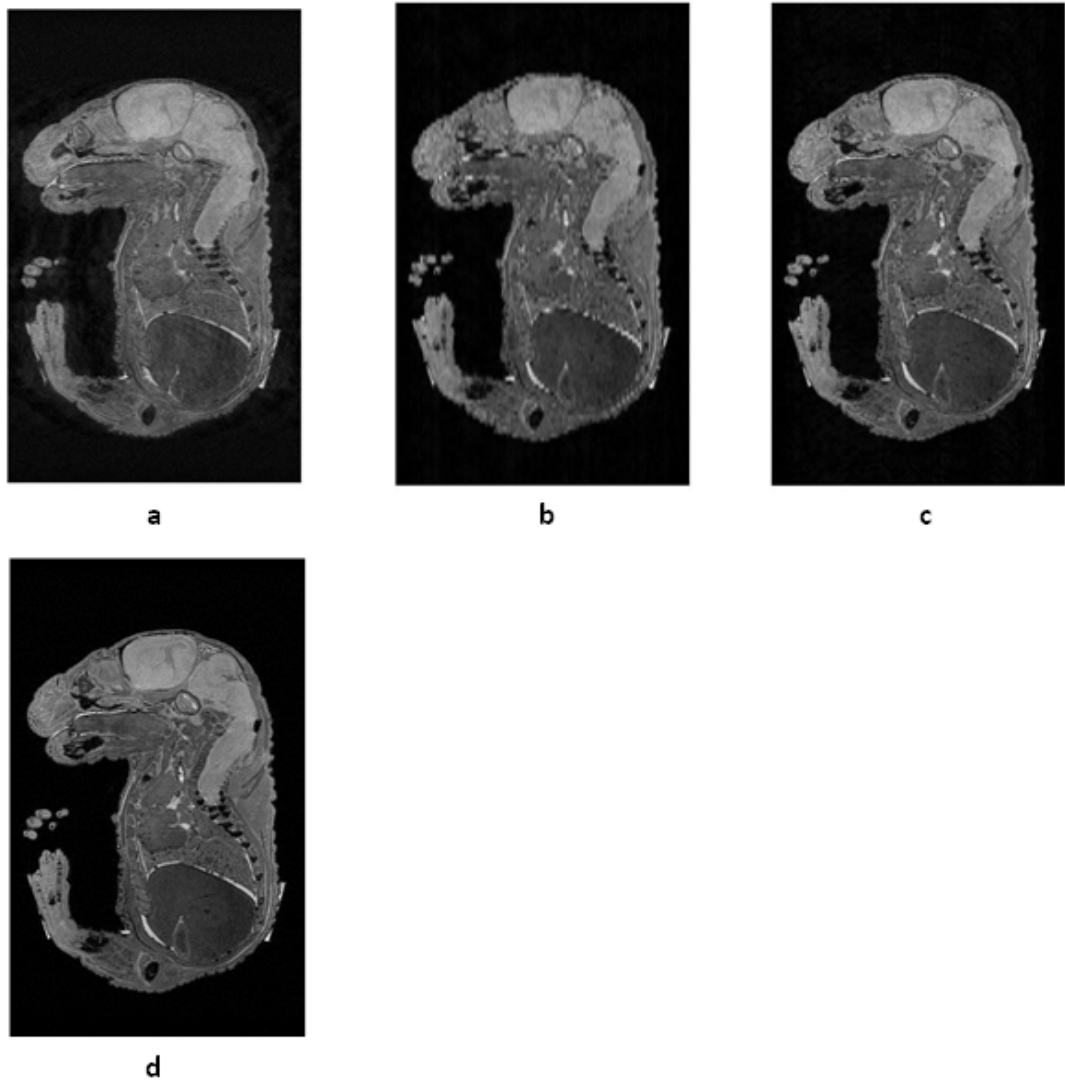


Figure 4.9: Simulated motion in biological phantom experiment a) coronal view corrupted with motion, b) axial view upsampled and rotated with motion, c) motion corrected image, d) *ex vivo* image without motion

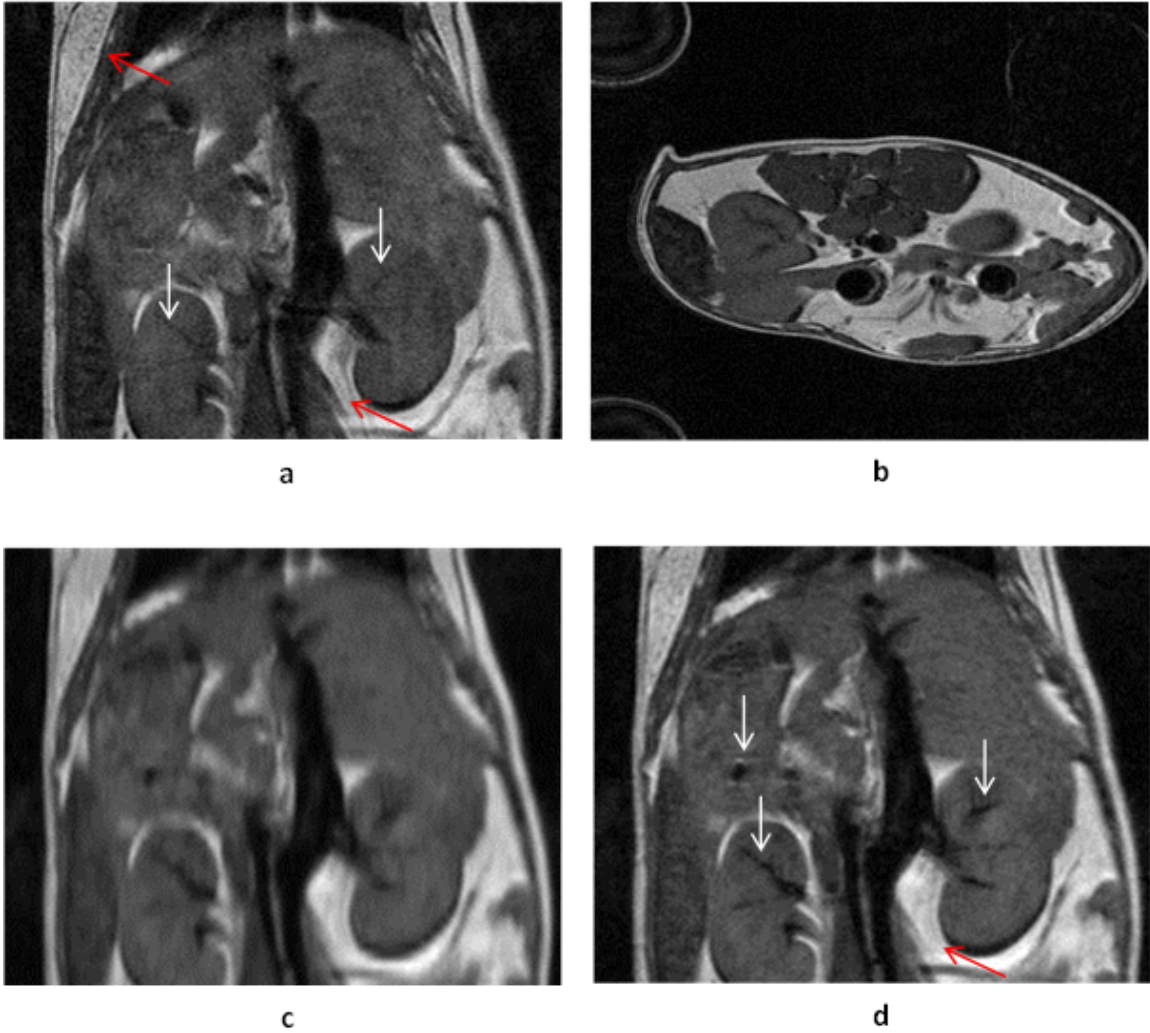
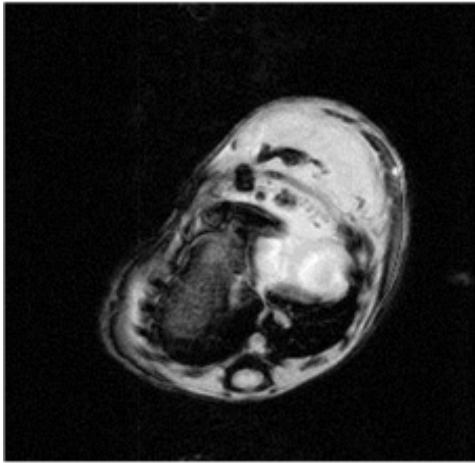
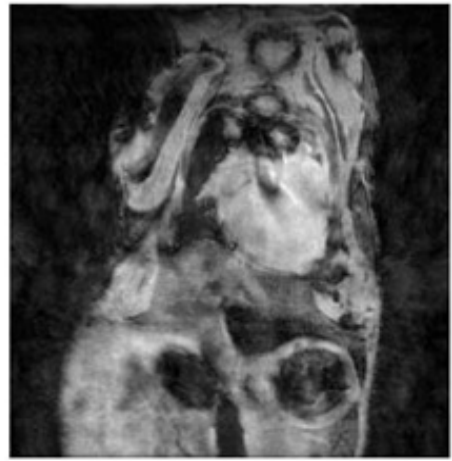


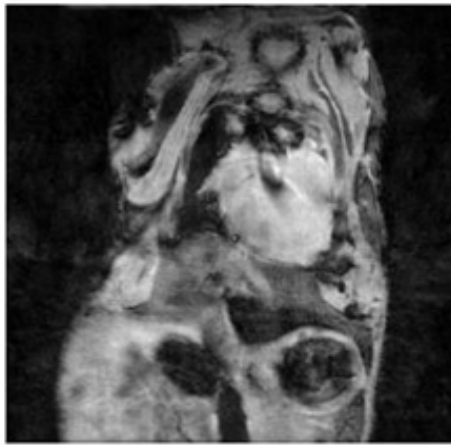
Figure 4.10: *In vivo* gated experiment for obesity study, a) coronal with motion, b) axial with motion, c) axial upsampled and rotated, d) motion corrected image. The ghosting artifact in coronal view is highlighted by red arrow. Anatomical details recovered by the correction algorithm are highlighted by white arrows



a



b



c

Figure 4.11: *In vivo* non-gated experiment for rib tumor study a) axial image stack with less pronounced motion, b) coronal image stack with motion, c) motion corrected image

## Chapter 5: Conclusions and Future Work

### 5.1 Thesis Summary and Conclusions

The use of three different SRR acquisition geometries (i.e., shifted, rotational, orthogonal) for improving through plane resolution in 3D high resolution imaging was discussed in chapter 2. We have shown that the SRR images based on orthogonal acquisition geometry provide a better trade-off between resolution, acquisition time, SNR, and CNR than those based on shifted and rotational acquisition geometries. This was observed for LR images with voxel ARs less than 1:1:6. However, for the orthogonal acquisition geometry, we observed when slice thickness was increased beyond voxel AR of 1:1:6, artifacts occurred in the SRR image. As these artifacts were not consistently present in the same location with increasing voxel AR, we concluded that the artifact is dependent upon the sampling and where a specific slice occurs in the object being sampled. Finally, we demonstrated that SRR is applicable for *in vivo* gated acquisitions. This observation along with the possibility of applying the SRR algorithm with higher voxel AR has the potential to make SRR a practical alternative to acquisition of 3D HR isotropic images in small animal phenotyping applications.

A post processing method that used gradient information from orthogonal images to reduce streaking artifacts observed in orthogonal SR reconstructed image was

discussed in chapter 3. As seen from phantom experiments, in the absence of noise and multiple inflection points, basic sigmoid based interpolation model using the gradient of the orthogonal view had improved the location and sharpness of the edges in the reconstruction of surfaces and small objects. The quantitative and qualitative evaluation of the *in vivo* experiment shows that the sigmoid SRR performs better than linear and cubic interpolation schemes. In biological phantom and *in vivo* experiments the adverse effects of using the gradient from the average image were prominent as images have more anatomical structures as opposed the simulated phantom with well-defined geometrical structures. In addition, we have shown that the quality of a SRR image based on orthogonal acquisition was improved by the addition of a fourth view, acquired obliquely to the through-plane direction of the coronal or sagittal view. The observed increase in image quality would justify the minimal increase in acquisition time required for one additional view.

The development of a post processing method that used two orthogonal views obtained with different slice-select directions to correct for motion artifacts in 2D images was discussed in chapter 4. We have shown that it was advantageous to make use of available orthogonal images to reduce the ghosting artifacts caused by motion. The efficacy of the algorithm was evaluated using phantom images with various types of simulated motion. The performance of the algorithm declined with increase in voxel ARs. Higher voxel ARs, have less effective motion reduction and hence lead to more compromised effective resolution. The algorithm combined image stacks with motion artifacts in different directions, so even as we noticed a reduction of motion in one direction, we have to consider the fact that the method introduced artifacts in another direction where motion was absent in the original image. The algorithm

performed well when there was a slight misalignment between the acquisitions of two orthogonal scans because of subject motion, but when the misalignment was substantial, the effectiveness of the correction algorithm decreased. The performance of the algorithm deteriorated with the increase in noise. However in case of severe motion (like non-gated images), acquiring an additional image for the exclusive use of correction algorithm, might not be worth the trade-off in time.

This dissertation aims to answer the question of whether or not it is possible to use multiple imaging views obtained as part of the normal workflow of imaging studies for improving the quality of the MR image. The main reason for this evaluation is that typically in many small animal imaging studies, multiple imaging views are already obtained as part of the normal workflow but the information taken from one view is not generally combined with that from another view, except in the mind of the expert observer. The development of techniques outlined in chapters 3 and 4 of this dissertation provide some answers this question. The techniques developed in this dissertation make use of multiple low resolution image acquisitions to increase through-plane resolution in 3D image data and to reduce motion artifacts for in-plane 2D images.

## 5.2 Suggested Future Work

In this work, IBP was used for reconstructing the SRR images. More recently regularized least square methods that incorporate prior knowledge as a regularization term have been proposed [53] for SRR implementation. These different optimization algorithms, such as LASR and Tikhonov regularization(TIK), have shown improved

resolution over IBP optimization when the number of LR stacks used for reconstruction is greater than three (i.e., TIK) [52]. However SNR was observed to be greater for IBP when a larger number of LR stacks were used for reconstruction. Plenge's study suggests that different optimization schemes may perform better than others and may be dependent upon the application and the number of LR stacks used for reconstruction [52]. Therefore, future work could focus on implementing these optimization schemes and testing them.

In the gradient guided sigmoid based interpolation model, the location of global maximum within the interpolation window was assigned as single inflection point. In this algorithm the gradient from the average of two orthogonal images was used. In using the average image we might lose the significant gradients or end up with a reduced gradient intensity corresponding to these structures. Using the gradients separately from both the orthogonal images might provide a more robust framework for assigning the inflection point. The future studies should explore a robust framework to detect the inflection point and to fuse the separate gradient information from both orthogonal images to guide the interpolation.

The future studies could be directed towards extending the motion correction algorithm to nearly or quasi-orthogonal images. The combination of orthogonal SRR which improves the through-plane resolution in 3D images with the in-plane motion reduction technique using orthogonal images was outside the scope of this dissertation. Studying the combination of orthogonal SRR and in-plane motion correction using orthogonal images presents an interesting venue for the future research.

## Bibliography

- [1] R. S. Balaban. Physiological and biochemical information from water in cardiac mri. In C. B. Higgins, J. S. Ingwall, and G. M. Pohost, editors, *Current and Future Applications of Magnetic Resonance in Cardiovascular Disease*. Futura Publishing Inc., Armonk NY, 1998.
- [2] R. S. Balaban and V. A. Hampshire. Challenges in small animal noninvasive imaging. *ILAR Journal*, 42(3):248–262, 2001.
- [3] J. D. Blumenthal, A. Zijdenbos, E. Molloy, and J. N. Giedd. Motion artifact in magnetic resonance imaging: implications for automated analysis. *Neuroimage*, 16(1):89–92, May 2002.
- [4] P. J. Bones and J. R. Maclaren. Improved bulk rotation detection and correction in MRI. In *Conf Proc IEEE Eng Med Biol Soc*, pages 2106–9, 2007.
- [5] P. J. Cassidy, J. E. Schneider, S. M. Grieve, C. Lygate, S. Neubauer, and K. Clarke. Assessment of motion gating strategies for mouse magnetic resonance at high magnetic fields. *J Magn Reson Imaging*, 19(2):229–37, February 2004.
- [6] V. Chalana and Y. Kim. Methodology for evaluation of image segmentation algorithms on medical images. volume 2710, pages 178–189, April 1996.
- [7] X. J. Chen and B. J. Nieman. Mouse Phenotyping with MRI. *Methods in molecular biology*, 771:595–631, 2011.
- [8] I. Corouge and C. Barillot. Use of a probabilistic shape model for non-linear registration of 3d scattered data. In *Image Processing, Proceedings. 2001 International Conference on*, volume 1, pages 149–152, 2001.
- [9] C. deGraaf, A. Koster, K. Vincken, and M. Viergever. A methodology for the validation of image segmentation algorithms. page 1724, 1992.
- [10] R. L. Ehman and J. P. Felmlee. Adaptive technique for high-definition mr imaging of moving structures. *Radiology*, 173(1):255–63, October 1989.

- [11] C. Fellner, W. Mller, J. Georgi, U. Taubenreuther, F. A. Fellner, and W. A. Kalender. A high-resolution phantom for mri. *Magn Reson Imaging*, 19(6):899–904, July 2001.
- [12] J. P. Felmlee and R. L. Ehman. Spatial presaturation: a method for suppressing flow artifacts and improving depiction of vascular anatomy in mr imaging. *Radiology*, 164(2):559–64, August 1987.
- [13] A. Gholipour, J. A. Estroff, M. Sahin, S. P. Prabhu, and S. K. Warfield. Maximum a posteriori estimation of isotropic high-resolution volumetric MRI from orthogonal thick-slice scans. *Med Image Comput Comput Assist Interv*, 13(Pt 2):109–16, 2010.
- [14] A. Gholipour, J. A. Estroff, and S. K. Warfield. Robust super-resolution volume reconstruction from slice acquisitions: application to fetal brain MRI. *IEEE Trans Med Imaging*, 29(10):1739–58, October 2010.
- [15] F. Glockner, H. H. Hu, D. W. Stanley, L. Angelos, and K. King. Parallel MR Imaging: A User’s Guide. *Radiographics*, 25(5):1279–1297, September 2005.
- [16] R. C. Gonzalez and R. E. Woods. *Digital Image Processing*. Prentice Hall, 2 edition, January 2002.
- [17] H. Greenspan, G. Oz, N. Kiryati, and S. Peled. MRI inter-slice reconstruction using super-resolution. *Magnetic resonance Imaging*, 20(5):437–446, 2002.
- [18] G. J. Grevera and J. K. Udupa. An objective comparison of 3-d image interpolation methods. *IEEE Trans Med Imaging*, 17(4):642–652, August 1998.
- [19] E. M. Haacke, R. W. Brown, M. R. Thompson, and R. Venkatesan. *Magnetic Resonance Imaging: Physical Principles and Sequence Design*. Wiley-Blackwell, 2 edition, June 2014.
- [20] E. Heijman, W. de Graaf, P. Niessen, A. Nauerth, G. van Eys, L. de Graaf, K. Nicolay, and G. J. Strijkers. Comparison between prospective and retrospective triggering for mouse cardiac mri. *NMR Biomed*, 20(4):439–47, June 2007.
- [21] M. Herbst, J. Maclaren, C. Lovell-Smith, R. Sostheim, K. Egger, A. Harloff, J. Korvink, J. Hennig, and M. Zaitsev. Reproduction of motion artifacts for performance analysis of prospective motion correction in mri. *Magn Reson Med*, 71(1):182–90, January 2014.
- [22] K. H. Herrmann, S. Schmidt, A. Kretz, R. Haenold, I. Krumbein, M. Metzler, C. Gaser, O. W. Witte, and J. R. Reichenbach. Possibilities and limitations for high resolution small animal mri on a clinical whole-body 3t scanner. *MAGMA*, 25(3):233–44, June 2012.

- [23] I. J. Hildebrandt, H. Su, and W. A. Weber. Anesthesia and other considerations for in vivo imaging of small animals. *ILAR Journal*, 49(1):17–26, 2008.
- [24] R. S. Hinks, Q. S. Xiang, and R. M. Henkelman. Ghost phase cancellation with phase-encoding gradient modulation. *J Magn Reson Imaging*, 3(5):777–85, September-October 1993.
- [25] D. Huang and C. Wang. Optimal multi-level thresholding using a two-stage otsu optimization approach. *Pattern Recogn. Lett.*, 30(3):275–284, February 2009.
- [26] M. Hutchinson and U. Raff. Fast mri data acquisition using multiple detectors. *Magn Reson Med.*, 6(1):87–91, January 1988.
- [27] H. T. Huynh, I. Karademir, A. Oto, and K. Suzuki. Computerized liver volumetry on mri by using 3d geodesic active contour segmentation. *AJR Am J Roentgenol.*, 202(1):152–9, January 2014.
- [28] M. Irani and S. Peleg. Motion analysis for image enhancement: resolution, occlusion, and transparency. *Journal of visual communication and image presentation*, 4(4):324–335, 1993.
- [29] A. K. Jain. *Fundamentals of Digital Image Processing*. Prentice Hall, 1 edition, October 1988.
- [30] A. P. Jason, A. B. Matthew, and K. F. Foo Thomas. MRI reconstruction using partial echo and partial NEX data acquisitions. (6166545), December 2000.
- [31] M. Joliot and B. M. Mazoyer. Three-dimensional segmentation and interpolation of magnetic resonance brain images. *IEEE Trans Med Imaging*, 12(2):269–77, 1993.
- [32] M. Kass, A. Witkin, and D. Terzopoulos. Snakes: Active contour models. *International Journal of Computer Vision*, 1(4):321–331, 1988.
- [33] C. G. Koay, J. E. Sarlls, and E. Ozarslan. Three-dimensional analytical magnetic resonance imaging phantom in the fourier domain. *Magn Reson Med*, 58(2):430–6, August 2007.
- [34] H. W. Korin, F. Farzaneh, R. C. Wright, and S. J. Riederer. Compensation for effects of linear motion in mr imaging. *Magnetic Resonance in Medicine*, 12(1):99–113, October 1989.
- [35] D. G. Kruger, G. S. Slavin, R. Muthupillai, R. C. Grimm, and S. J. Riederer. An orthogonal correlation algorithm for ghost reduction in mri. *Magn Reson Med*, 38(4):678–86, October 1997.

- [36] M. Kuklisova-Murgasova, G. Quaghebeur, M. A. Rutherford, J. V. Hajnal, and J. A. Schnabel. Reconstruction of fetal brain MRI with intensity matching and complete outlier removal. *Med Image Anal*, 16(8):1550–64, December 2012.
- [37] L. Landini, V. Positano, and M. Santarelli, editors. *Advanced Image Processing in Magnetic Resonance Imaging (Signal Processing and Communications)*. CRC Press, 1 edition, September 2005.
- [38] P. C. Lauterbur. Image formation by induced local interactions: Examples employing nuclear magnetic resonance. *Nature*, 242:190–191, March 1973.
- [39] T. M. Lehmann, C. Gonner, and K. Spitzer. Survey: interpolation methods in medical image processing. *IEEE Trans Med Imaging*, 18(11):1049–75, November 1999.
- [40] R. A. Lerski and J. D. de Certaines. Performance assessment and quality control in mri by eurospin test objects and protocols. *Magn Reson Imaging*, 11(6):817–33, 1993.
- [41] S. Ljunggren. A Simple Graphical Representation of Fourier-Based Imaging Methods. *J. Magn. Reson.*, 54:338–343, 1983.
- [42] J. R. MacFall, N. J. Pelc, and R. M. Vavrek. Correction of spatially dependent phase shifts for partial Fourier imaging. *Magnetic Resonance Imaging*, 6(2):143 – 155, 1988.
- [43] J. R. Maclaren. *Motion Detection and Correction in Magnetic Resonance Imaging*. PhD thesis, University of Canterbury, Christchurch, New Zealand, January 2008.
- [44] B. Madore and R. M. Henkelman. A new way of averaging with applications to mri. *Med Phys*, 23(1):109–13, January 1996.
- [45] M. J. McAuliffe, F. M. Lalonde, D. McGarry, W. Gandler, K. Csaky, and B. L. Trus. Medical image processing, analysis and visualization in clinical research. In *Computer-Based Medical Systems, 2001. CBMS 2001. Proceedings. 14th IEEE Symposium on*, pages 381–386, 2001.
- [46] S. A. Mirowitz. Mr imaging artifacts. challenges and solutions. *Magn Reson Imaging Clin N Am.*, 7(4):717–32, November 1999.
- [47] A. Mishra, Y. Lu, J. Meng, A. W. Anderson, and Z. Ding. Unified framework for anisotropic interpolation and smoothing of diffusion tensor images. *Neuroimage*, 31(4):1525–35, July 2006.

- [48] R. J. Mural, M. D. Adams, E. W. Myers, H. O. Smith, G. L. Miklos, and R. Wides et al. A comparison of wholegenome shotgun-derived mouse chromosome 16 and the human genome. *Science*, 296(5573):1661–71, May 2002.
- [49] S. Osher and R. Fedkiw. *Level set methods and dynamic implicit surfaces*. Springer-Verlag, New York, 2003.
- [50] N. Otsu. A threshold selection method from gray-level histogram. *IEEE Trans. Systems Man Cybern*, 9(1):62–66, January 1979.
- [51] P. M. Pattany, J. J. Phillips, L. C. Chiu, J. D. Lipcamon, J. L. Duerk, J. M. McNally, and S. N. Mohapatra. Motion artifact suppression technique (mast) for mr imaging. *J Comput Assist Tomogr.*, 11(3):369–77, May-June 1987.
- [52] E. Plenge, D. H. Poot, M. Bernsen, G. Kotek, G. Houston, P. Wielopolski, L. van der Weerd, W. J. Niessen, and E. Meijering. Super-Resolution Methods in MRI: Can They Improve the Trade-Off Between Resolution, Signal-to-Noise Ratio, and Acquisition Time? *Magnetic Resonance in Medicine*, 68(6):1983–1993, December 2012.
- [53] D. H. J. Poot, V. Van Meir, and J. Sijbers. General and efficient Super-resolution method for multi-slice MRI. *Proceedings of the 13th International Conference on Medical Image Computing and Computer-Assisted Intervention: Part I. Berlin, Heidelberg: Springer-Verlag*, page 615622, 2010.
- [54] R. R. Price, L. Axel, T. Morgan, R. Newman, W. Perman, N. Schneiders, M. Selikson, M. Wood, and S. R. Thomas. Quality assurance methods and phantoms for magnetic resonance imaging: report of aapm nuclear magnetic resonance task group no. 1. *Med Phys.*, 17(2):287–95, March-April 1990.
- [55] W. M. Rand. Objective criteria for the evaluation of clustering methods. *Journal of the American Statistical Association*, 66(336):846–850, December 1971.
- [56] S. E. Rose, S. J. Wilson, F. O. Zelaya, S. Crozier, and D. M. Doddrell. High resolution high field rodent cardiac imaging with flow enhancement suppression. *Magn Reson Imaging*, 12(8):1183–90, 1994.
- [57] F. Rousseau, K. Kim, C. Studholme, M. Koob, and J. L. Dietemann. On super-resolution for fetal brain MRI. *Med Image Comput Comput Assist Interv*, 13(Pt 2):355–62, 2010.
- [58] A. Tannenbaum S. Lankton. Localizing region-based active contours. *Image Processing, IEEE Transactions on*, 17(11):2029–2039, November 2008.

- [59] B. Scherrer, A. Gholipour, and S. K. Warfield. Super-resolution reconstruction to increase the spatial resolution of diffusion weighted images from orthogonal anisotropic acquisitions. *Medical Image Analysis*, 16(7):1465–76, October 2012.
- [60] R. Z. Shilling, T. Q. Robbie, T. Bailloeuil, K. Mewes, R. M. Mersereau, and M. E. Brummer. A Super-resolution Framework for 3-D High Resolution and High Contrast Imaging Using 2-D Multi-slice MRI. *IEEE Trans Med Imaging*, 28(5):633–44, 2009.
- [61] F. M. Siri, L. A. Jelicks, L. A. Leinwand, and J. M. Gardin. Gated magnetic resonance imaging of normal and hypertrophied murine hearts. *Am J Physiol*, 272(5 Pt 2):H2394–402, May 1997.
- [62] A. Souza and R. Senn. Model-based super-resolution for MRI. *Engineering in Medicine and Biology Society, 2008. 30th Annual International Conference of the IEEE*, pages 430–434, August 2008.
- [63] H. Takeda and P. Milanfar. An adaptive nonparametric approach to restoration and interpolation for medical imaging. In *Biomedical Imaging: From Nano to Macro, 2009. ISBI '09. IEEE International Symposium on*, pages 666–669, June 2009.
- [64] E. C. Unger, M. S. Cohen, R. A. Gatenby, M. R. Clair, T. R. Brown, S. J. Nelson, and J. S. McGlone. Single breath-holding scans of the abdomen using FISP and FLASH at 1.5 T. *J Comput Assist Tomogr.*, 12(4):575–83, July-August 1988.
- [65] R. Unnikrishnan, C. Pantofaru, and M. Hebert. Toward objective evaluation of image segmentation algorithms. *Pattern Analysis and Machine Intelligence, IEEE Transactions on*, 29(6):929–944, June 2007.
- [66] Y. Kim V. Chalana. A methodology for evaluation of boundary detection algorithms on medical images. *IEEE Trans Med Imaging*, 16(5):642–52, October 1997.
- [67] J. P. Vallee, M. K. Ivancevic, D. Nguyen, D. R. Morel, and M. Jaconi. Current status of cardiac mri in small animals. *MAGMA*, 17(3-6):149–56, December 2004.
- [68] S. K. Warfield, K. H. Zou, and W. M. Wells. Validation of image segmentation and expert quality with an expectation-maximization algorithm. volume 2488, pages 298–306, October 2002.
- [69] E. B. Welch. *Motion Correction Techniques for Magnetic Resonance Imaging*. PhD thesis, Mayo Graduate School, July 2003.

- [70] E. B. Welch, J. P. Felmlee, R. L. Ehman, and A. Manduca. Motion correction using the k-space phase difference of orthogonal acquisitions. *Magn Reson Med*, 48(1):147–56, July 2002.
- [71] G. W. Williams. Comparing the joint agreement of several raters with another rater. *Biometrics*, 32:619627, September 1976.
- [72] J. Woo, E. Z. Murano, M. Stone, and J. L Prince. Reconstruction of high-resolution tongue volumes from MRI. *IEEE Trans Biomed Eng*, 59(12):3511–24, December 2012.
- [73] M. L. Wood and R. M. Henkelman. Mr image artifacts from periodic motion. *Med Phys.*, 12(2):143–51, March-April 1985.
- [74] Q. S. Xiang, M. J. Bronskill, and R. M. Henkelman. Two-point interference method for suppression of ghost artifacts due to motion. *J Magn Reson Imaging*, 3(6):900–6, November-December 1993.
- [75] Q. S. Xiang and R. M. Henkelman. Motion artifact reduction with three-point ghost phase cancellation. *J Magn Reson Imaging*, 1(6):633–42, November-December 1991.
- [76] F. G. Zllner, E. Svarstad, A. Z. Munthe-Kaas, L. R. Schad, A. Lundervold, and J. Rorvik. Assessment of kidney volumes from mri: acquisition and segmentation techniques. *AJR Am J Roentgenol.*, 199(5):1060–9, November 2012.